

From Department of Clinical Neuroscience
Karolinska Institutet, Stockholm, Sweden

HIGH-RESOLUTION DIFFUSION- WEIGHTED BRAIN MRI UNDER MOTION

Mathias Engström



**Karolinska
Institutet**

Stockholm 2014

All previously published papers were reproduced with permission from the publisher.

Published by Karolinska Institutet.

Printed by Universitetsservice US-AB

© Mathias Engström, 2014

ISBN 978-91-7549-676-4

High-Resolution Diffusion-Weighted Brain MRI under Motion

THESIS FOR DOCTORAL DEGREE (Ph.D.)

By

Mathias Engström

Principal Supervisor:

Stefan Skare
Karolinska Institutet
Department of Clinical Neuroscience

Co-supervisors:

Olof Flodmark
Karolinska Institutet
Department of Clinical Neuroscience

Anders Lilja
Karolinska Institutet
Department of Clinical Neuroscience

Opponent:

Chunlei Liu
Duke University
Department of Medical Radiation Physics
Division of Medical Physics

Examination Board:

Jonas Svensson
Lund University
Department of Medical Radiation Physics
Division of Medical Physics

Danielle van Westen
Lund University
Department of Diagnostic Radiology
Division of Neuroradiology

Andreas Sigfridsson
Karolinska Institutet
Department of Molecular Medicine and Surgery

ABSTRACT

Magnetic resonance imaging is one of the fastest developing medical imaging techniques. It provides excellent soft tissue contrast and has been a leading tool for neuroradiology and neuroscience research over the last decades. One of the possible MR imaging contrasts is the ability to visualize diffusion processes. The method, referred to as diffusion-weighted imaging, is one of the most common clinical contrasts but is prone to artifacts and is challenging to acquire at high resolutions.

This thesis aimed to improve the resolution of diffusion weighted imaging, both in a clinical and in a research context. While diffusion-weighted imaging traditionally has been considered a 2D technique the manuscripts and methods presented here explore 3D diffusion acquisitions with isotropic resolution. Acquiring multiple small 3D volumes, or slabs, which are combined into one full volume has been the method of choice in this work.

The first paper presented explores a parallel imaging driven multi-echo EPI readout to enable high resolution with reduced geometric distortions. The work performed on diffusion phase correction lead to an understanding that was used for the subsequent multi-slab papers.

The second and third papers introduce the diffusion-weighted 3D multi-slab echo-planar imaging technique and explore its advantages and performance. As the method requires a slightly increased acquisition time the need for prospective motion correction became apparent.

The forth paper suggests a new motion navigator using the subcutaneous fat surrounding the skull for rigid body head motion estimation, dubbed FatNav. The spatially sparse representation of the fat signal allowed for high parallel imaging acceleration factors, short acquisition times, and reduced geometric distortions of the navigator.

The fifth manuscript presents a combination of the high-resolution 3D multi-slab technique and a modified FatNav module. Unlike our first FatNav implementation, using a single sagittal slab, this modified navigator acquired orthogonal projections of the head using the fat signal alone.

The combined use of both presented methods provides a promising start for a fully motion corrected high-resolution diffusion acquisition in a clinical setting.

LIST OF SCIENTIFIC PAPERS

- I. *Diffusion Weighted Vertical Gradient and Spin Echo*
Engström M, Bammer R, Skare S
Magn Reson Med 68:1755-1763 (2013)
- II. *Diffusion-Weighted 3D Multi-Slab Echo Planar Imaging for High Signal-to-Noise Ratio Efficiency and Isotropic Image Resolution*
Engström M, Skare S
Magn Reson Med 70:1507-14 (2013)
- III. *On the Signal-to-Noise Ratio Efficiency and Slab-Banding Artifacts in Three-Dimensional Multi-Slab Diffusion-Weighted Echo Planar Imaging*
Engström M, Mårtensson M, Avventi E, Skare S
Magn Reson Med 2014 Mar 19. doi: 10.1002/mrm.25182
- IV. *Properties of a 2D Fat Navigator for Prospective Image Domain Correction of Nodding Motion in brain MRI*
Skare S, Hartwig A, Mårtensson M, Avventi E, **Engström M**
Magn Reson Med 2014 Apr 2014. doi: 10.1002/mrm.25234
- V. *Collapsed Fat Navigators for Brain 3D Rigid Body Motion*
Engström M, Mårtensson M, Avventi E, Norbeck O, Skare S,
Manuscript

CONTENTS

1	Introduction	7
1.1	Magnetic resonance Imaging	7
1.1.1	Basic image formation	7
1.1.2	Echo Planar Imaging.....	16
1.1.3	Diffusion-Weighted Imaging.....	21
1.1.4	Multi-Slab Imaging	28
1.2	Motion correction	31
1.2.1	Basics	31
1.2.2	Retrospective motion correction	34
1.2.3	Prospective correction	36
1.2.4	Motion Navigators	37
1.2.5	Motion Fat Navigators.....	38
1.3	Clinical needs And Outlook.....	39
1.3.1	Diffusion-Weighted Imaging.....	39
1.3.2	Cost.....	39
2	Aim of thesis	41
2.1	Specific aims	41
2.1.1	Study I – DW vGRASE	41
2.1.2	Study II – DW 3D-MS EPI	41
2.1.3	Study III – DW 3D-MS EPI.....	41
2.1.4	Study IV – FatNav	41
2.1.5	Study V – Collapsed FatNav.....	42
3	Materials and Methods.....	43
3.1	MRI Systems.....	43
3.2	Diffusion-Weighted Imaging.....	43
3.2.1	DW vGRASE	43
3.2.2	DW 3D-MS EPI – General	46
3.2.3	DW 3D-MS EPI – Sequence.....	53
3.2.4	DW 3D-MS EPI – Efficiency and Artifacts.....	55
3.3	Motion correction	57
3.3.1	2D Sagittal FatNav to address nodding motion	57
3.3.2	Collapsed FatNav	60
4	Results	63
4.1	DW vGRASE	63
4.2	DW 3D-MS EPI – Paper I.....	64
4.3	DW 3D-MS EPI – Paper II	67
4.4	FatNav	68
4.5	Collapsed FatNav	70

Discussion	72
4.6 Diffusion-weighted imaging	72
4.6.1 Low distortion imaging and vGRASE	72
4.6.2 Multi-Slab Imaging	73
4.6.3 2D versus 3D	75
4.6.4 Challenges	76
4.7 Motion correction	77
4.7.1 Fat navigators	77
4.7.2 Collapsed fat navigators	79
5 Acknowledgements	82
6 References	84

LIST OF ABBREVIATIONS

γ	The gyromagnetic constant. ^1H : 42.576 MHz/T
ADC, D	Apparent Diffusion Coefficient
B_0	Main magnetic field
B_1+	RF excitation field
B_1-	RF receive field (coil dependent)
BW	Bandwidth
cFatNav	Collapsed FatNav
CPMG	Carr Purcell Meiboom Gill
CUBE	3D FSE
DSV	Diameter of a Spherical Volume
DTI	Diffusion Tensor Imaging
DW	Diffusion Weighted
ETL	Echo Train Length
EOS	End-Of-Sequence
EPI, ss-EPI	Echo Planar Imaging, single-shot Echo Planar Imaging
ESP	Echo spacing
FA	Fractional Anisotropy
FatNav	Fat Navigator
FE, fe	Frequency encoding
FID	Free Induction Decay
FLAIR	Fluid Attenuated Inversion Recovery
fMRI	Functional MRI
FOV	Field of view
FSE, ss-FSE	Fast Spin-Echo, single-shot Fast Spin Echo
FWHM	Full Width Half Maximum
GA	General Anesthesia
GE, GRE	Gradient Echo
IQ	Image Quality
IR	Inversion Recovery

MRI	Magnetic Resonance Imaging
ms	Multi-shot
MS	Multi-Slab
PE, pe	Phase encoding
Pixel	Picture element
PNS	Peripheral Nerve Stimulation
POCS	Projection Onto Convex Set
rBW, prBW	Receiver Bandwidth, pseudo Receiver Bandwidth
RS	Readout Segmented
SE	Spin-Echo
SNR	Signal-to-Noise Ratio
SPGR	Spoiled GRASS
SpSp	Spectral Spatial
TE	Echo time (ms)
Tmin	Minimal sequence time (1 st excitation to EOS killer)
TR	Repetition time (ms)
vNav	Volume Navigator
WM	White matter

1 INTRODUCTION

1.1 MAGNETIC RESONANCE IMAGING

Magnetic Resonance Imaging (MRI) is the most versatile soft tissue medical imaging technique currently available. It is capable of producing image data with tailored tissue contrasts, high spatial resolution, high temporal resolution, and functional image data series where biological processes such as, e.g. diffusion, perfusion, and susceptibility can be visualized. It is an essential tool for radiologists and plays a major role in clinical neuroscience. Due to the non-invasive, non-ionizing, nature of MRI the research community is steadily improving the quality of the technique, adding to the ways in which data can be acquired.

1.1.1 Basic image formation

1.1.1.1 Nuclear Magnetic Resonance

In 1952 the Nobel Prize was awarded to Felix Bloch and Edward Mills Purcell for their discoveries regarding how to measure nuclear magnetic frequency and magnetism. Bloch and Purcell discovered that if certain atomic nuclei were placed in a strong magnetic field they could both absorb and emit energy at a certain resonance frequency, which they called nuclear magnetic resonance (NMR). This applied only to nuclei that had a magnetic moment such as e.g. ^1H , ^{13}C , ^{19}F , ^{23}Na , and ^{31}P . The unique precession frequency for each nucleus is determined by the Larmor equation as:

$$f = \frac{\gamma}{2\pi} B_0 \quad [1]$$

where γ is the gyromagnetic ratio [$\text{rad}\times\text{s}^{-1}\times\text{T}^{-1}$], specific for each nuclei, B_0 the strength of the externally applied magnetic field [T], and f the resulting resonance frequency [Hz]. Placing e.g. hydrogen atoms in a magnetic field of 1.5T, and exciting them with a radio frequency pulse at the resonance frequency ~64 MHz ($\gamma/2\pi \sim 42.57 \text{ MHz/T}$ for ^1H), can make them both absorb and emit RF at this specific frequency. Each nucleus has its own magnetic moment and will align and precess either parallel or anti-parallel with the B_0 -field, according to the Boltzmann distribution (1), which governs the resulting net magnetization that in turn determines the strength of the measured NMR signal. The Boltzmann distribution is given as follows:

$$\frac{N_{\text{parallel}}}{N_{\text{anti-parallel}}} = e^{\frac{h\gamma B_0}{kT}} \quad [2]$$

where h is Planck's constant (6.525×10^{-34} [Js], k Boltzmann's constant (1.381×10^{-23} [J/K]), and T the temperature in Kelvin [K]. For hydrogen in a B_0 field of 1.5T and an average body temperature of 37.5 C (~ 310.15 K) the Boltzmann distribution tells us that the ratio of parallel and anti-parallel spins is 1.0000098797. It is this tiny excess magnetization that creates the MR signal we can detect. The Boltzmann distribution also tells us that there are two ways in which this signal can be increased. The temperature of the object can be lowered, which is not very practical in a clinical situation, or the B_0 field can be increased.

The initial use of NMR was in chemistry to do classification and determine chemical content and structure of small samples. This could be done by exciting a sample with a spectrum of radio frequencies and listening to the frequency mixed signal ("Free Induction Decay", or FID). After a 1D Fourier transform of the acquired signal, a frequency spectrum is obtained, where certain configuration of the spectral peaks identifies a specific molecule or chemical configuration.

1.1.1.2 Magnetic Resonance Imaging

Doing NMR spectroscopy is however not the only way to utilize the NMR signal. In 2003 Sir Peter Mansfield and Paul C. Lauterbur were awarded with the Nobel Prize for their discoveries in the 70's regarding magnetic resonance imaging (MRI). Due to the bad connotation of the word *nuclear*, in the public eye, the 'N' in NMR has been dropped in the clinical use of NMR for imaging purposes. While a majority of medical imaging techniques rely on ionizing radiation ($f > \sim 10^{17}$ Hz), such as X-ray, computer tomography (CT), and positron emission tomography (PET), MRI utilizes electromagnetic radiation at the frequency range of radio waves (RF) at $\sim 10^6$ - 10^{12} , where exposure to these RF waves induces heat but no tissue ionization.

However, it is not the risk that separates the methods, but rather the difference in image contrast. With CT, the image contrast depends on the electron density in the body, which (like X-ray) makes CT excellent for imaging hard tissues such as bones. For MRI, the image contrast depends primarily on the proton density and two tissue-specific relaxation parameters (T_1 and T_2). In MRI, the soft tissues in the body give rise to the signal, with no signal from bone. MRI can also be performed in a way that images other biological processes, such as diffusion, perfusion, and angiography. Compared to other imaging modalities, the ways in which the image contrast can be manipulated in MRI are more intricate. While in CT one can only

adjust the image contrast moderately by changing the X-ray tube voltage (kV) and current (mAs), in MRI one can vary numerous parameters, such as TE, TR, TI, FA, and pulse sequence (as a narrow selection), the combination of which can produce any type of soft tissue contrast. This, as well as the much shorter scan times in CT, are reasons why CT has been considered fast, simple, and suitable for emergency care while MRI has been considered slow, complicated and more suited for advanced medical diagnosis.

The main reason hydrogen is so well suited for medical imaging is its abundance in the human body. Around 63% of the atoms in humans are hydrogen, where the majority (~60%) is bound in water (2). Other NMR active isotopes suitable for imaging are phosphorous ^{31}P , at 0.14%, and carbon ^{13}C at 0.12%. It should be noted that the occurrence of carbon is ~13% but it is only ^{13}C that has a magnetic moment. Imaging of other isotopes is possible, if adjusting the RF excitation frequency to match the specific gyromagnetic constant of the type of nucleus.

It is the chemical surrounding of hydrogen atoms that determines the rate in which the signal decays. As the MRI signal rely on a net magnetization vector being the sum of all nuclear spins in a voxel, it is important with the coherence of the spins. The larger a molecule is, the greater the magnetic interactions between excited hydrogen nuclei are. For large and less mobile molecules, such as bone and proteins, the magnetic interaction is strong and the signal will decay faster than the actual time required for signal collection. For fat and water and other small molecules, the likelihood for spin interactions is lower, making the MR signal decay slower.

1.1.1.3 The MR scanner

Modern MRI systems consist of four key components, or fields: A B_0 field, a B_1+ (or transmit RF) field, a B_1- (or receive RF) field, and a spatial gradient field - all of which are essential to acquire images. In addition, yet other fields are required to make a fully functional scanner such as shim fields and shielding fields.

The B_0 field is a static magnetic field that creates the required magnetic alignment of spins, i.e. the net magnetization in the body. A large supra-conductive magnet is used to create this strong field. In order to acquire images without considerable geometric distortions and signal loss, the field has to be extremely homogeneous, with standard limitations being ≤ 0.1 ppm spread across a given diameter of a spherical volume around the iso-center of the magnet. The majority of clinical systems active today are 1.5T and 3 T systems, but higher field-strengths are also

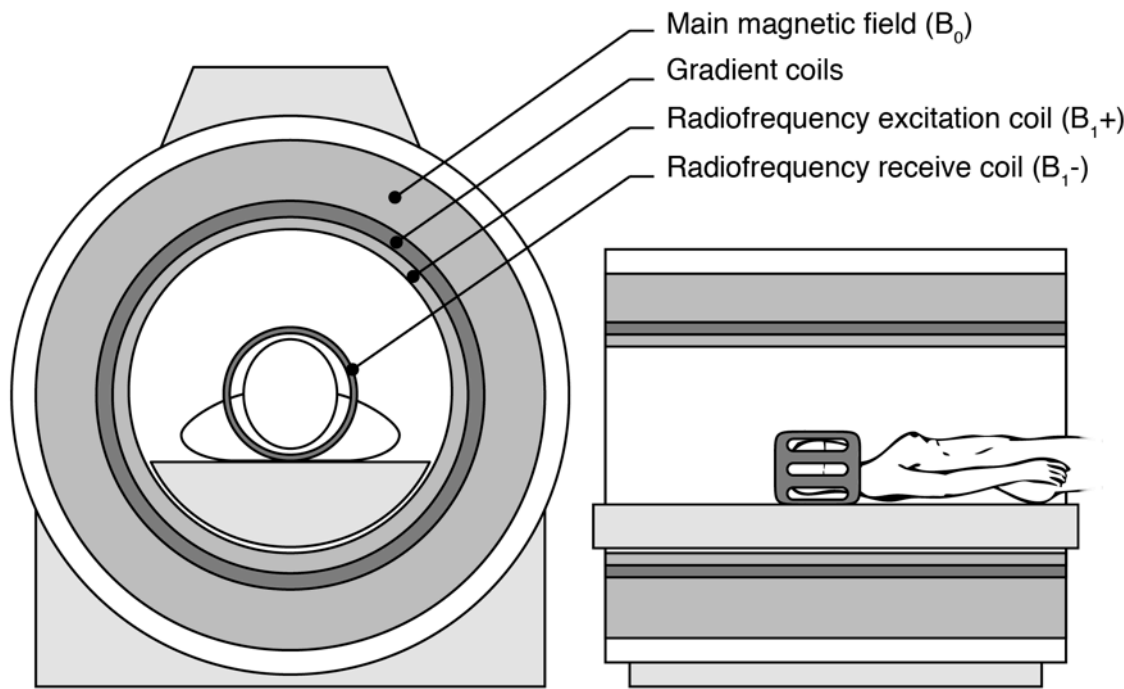


Figure 1. Schematic drawing of a MRI system

being explored. The main reason for moving to higher fields is the increased signal, which scales linearly with the field according to the Boltzmann distribution.

The B_{1+} field, or RF excitation (or transmit) field, is the coil responsible for producing the RF pulse that excites the spins. This field will push the spins out of their alignment with the z -axis (B_0 magnetic flux direction, M_z) into the orthogonal plane of M_{xy} , where they will precess around the M_z axis. The B_{1+} coil is often mounted within the bore of the magnet ('body coil') and is driven by large amplifiers, with a net effect of ~ 30 kW. As an RF field induces heat in the body, this part of the MRI system is closely monitored and controlled for safety reasons. The amount of energy, RF power, that is allowed to deposit into the body is measured as specific absorption rate (SAR) in [W/kg] and is regulated to never heat up the patient by more than 1 degree C (3).

While the B_{1+} field is responsible for the excitation of tissue, the B_{1-} field (the RF receive field) is a spatial field governed by the receiver coil ('antenna') corresponding to the local sensitivity of the MR signal echoed back from the body. In contrast to the powerful B_{1+} field, the signal from the resonating spins is very weak, why it is important that B_{1-} field is optimized to detect these signals as well as possible. This is why the RF coil elements/channels (the numbers and shapes is building up the B_{1-} field) in an RF receive coil are constructed in such a way that they can be located as close to the object as possible. Multi-channel RF coils serves also another purpose, in that their localized signal sensitivities allows for some

spatial encoding of the signal. This is utilized in advanced acquisition techniques such as *parallel imaging* and *multi-band imaging*, which shortens the acquisition time significantly.

The set of spatial (x-y-z) gradient fields is the last core component of an MRI scanner. These gradient fields create linear gradients fields in the main B_0 field within the bore (tunnel) of the scanner. It is these field changes that enable the spatial encoding, i.e. 'tags' the signal in space so we can form an image.

While the B_0 and B_1^- (RF receive) fields are static, the B_1^+ (RF transmit) and gradient fields are constantly changing during the image acquisition. The pulsating B_1^+ field repetitively excites the spins and the gradient fields are constantly changing to create the desired spatial encoding of the MR signal from the spins. It is this constant change in the gradient field that is the source for the acoustic noise that an MRI scanner creates (> 80-90 dBA). Although being molded into epoxy and bolted into place the rapid gradient field changes induces vibrations that propagates as acoustic wave out into the scanner room. Depending on the speed by which the field is changed the acoustic noise will vary in volume and frequency, but is nevertheless very difficult to reduce without sacrificing image quality.

While the B_0 field is measured in units of Tesla [T], the gradient field strength is measured in [mT/m] and the rate of the gradient field change (a.k.a. slew rate) is measured in [T/m/s]. A high-performance clinical MR system can typically deliver ~50 mT/m in gradient strength on each axis (x,y,z) independently of one another, with a slew rate of 200 T/m/s. While the byproduct of the pulsating B_1^+ field is heat, the side effect the of constantly changing the gradient field is peripheral nerve stimulation (PNS), measured in dB/dt, where dB is the field change over the time dt. PNS is a phenomenon that occurs when small currents are being created in the peripheral nerves, due to the rapid switching of the gradient fields, sending messages about muscle contractions. It is generally more uncomfortable than dangerous, and less of a safety concern compared to SAR.

1.1.1.4 Excitation and relaxation

As briefly discussed in the previous sections, an MR image is a product of manipulation of the magnetization that occurs when hydrogen spins are placed within a strong magnetic field. At equilibrium, the magnetization vector, \mathbf{M} , which is the sum of the magnetization from all hydrogen spins contained in a voxel (volume pixel), is parallel to the B_0 field (by convention denoted the z-axis). Its magnitude $\mathbf{M} = M_0$ is precessing around the z-axis at the Larmor frequency. It is useful to view two orthogonal components of the magnetization vector \mathbf{M} . One

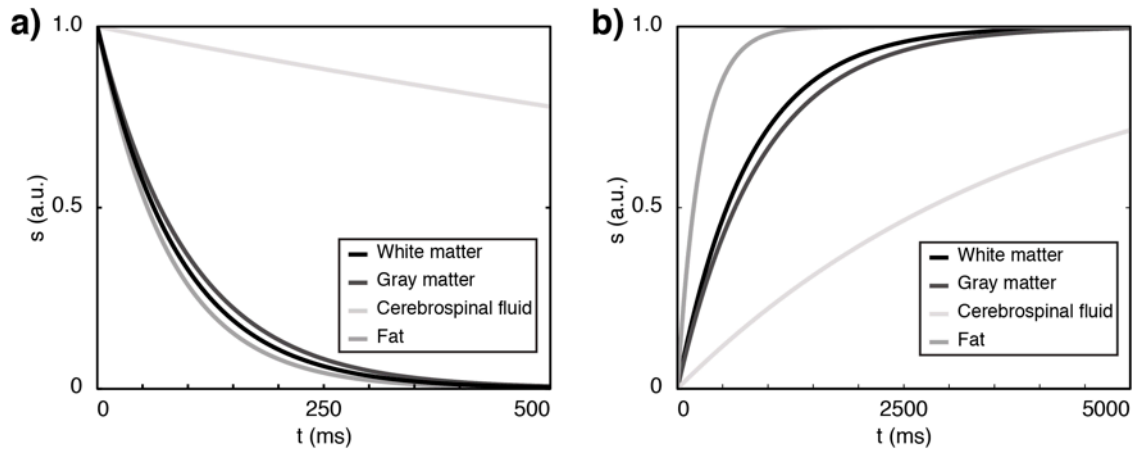


Figure 2. Typical a) T_2 , and b) T_1 relaxation curves for white matter, gray matter, cerebrospinal fluid, and fat.

that is pointing in the direction of the B_0 field, M_z , and one that are orthogonal to M_z , dubbed M_{xy} . When the B_{1+} field is applied it 'excites' the hydrogen protons (spins), making the net magnetization vector to rotated away from z-axis towards the xy-plane, still precessing at the Larmor frequency. The M_{xy} component of \mathbf{M} is proportional to the signal detected by the RF receiver coil, and this signal will be the product of the local MR signal and the local B_{1-} field. The angle at which the magnetization vector \mathbf{M} is rotated (towards the xy-plane) by the RF pulse is referred to as the flip angle (FA). An FA of 90° thus mean that 100% of the initial M_0 now resides in the xy-plane (with $M_z = 0$). Correspondingly, applying a three times shorter (or weaker) RF (B_{1+}) pulse, results in an FA that rotates \mathbf{M} by 30° . In this case, the corresponding M_z component vector is 86% (instead of 0%) and the M_{xy} component vector becomes 50% (instead of 100%).

The excited spins are subject to two types of relaxation processes: T_1 and T_2 relaxation. T_1 is the recovery of M_z magnetization along the z-axis, and T_2 is the signal decay in the M_{xy} plane. These are two independent processes that do not interfere with each other, although T_1 is always larger than T_2 .

T_1 relaxation, or spin-lattice relaxation, corresponds to the exponential rate by which the deposited energy leaves the excited system. This relaxation constant describes how fast \mathbf{M} returns to its equilibrium state, $\mathbf{M} = M_0$ along the z-axis. The T_1 -value of a tissue is defined as

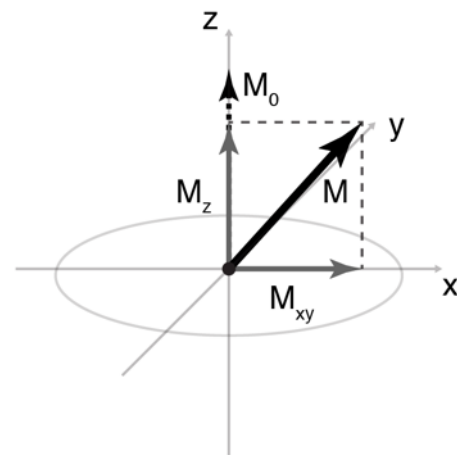


Figure 3. Magnetization vector \mathbf{M} with M_z and M_{xy} components

when 63% ($1-e^{-1}$) of the magnetization is recovered. For gray and white brain matter tissues of the brain, this is around 1 s (900 ms for white matter (WM), 1300 ms for gray matter (GM)), while for cerebrospinal fluid (CSF) it is ~4000 ms at 3 T. If M_z has not fully returned to M_0 when the next RF excitation pulse is applied, the following M_{xy} signal will be reduced due to this incomplete T_1 -relaxation, leading to a T_1 -w signal.

T_2 relaxation, or spin-spin relaxation, does not involve energy transfer but instead coherence. As spins move around they will occasionally get so close to one another that their local magnetic fields will interact, causing a momentary microscopic field changes that causes them to precess at different frequencies due to the Larmor equation. Once they separate again, they will return to the Larmor frequency of the

B_0 field, but their relative phase will be affected causing a net reduction in signal. The T_2 value of tissue is defined as when 37% (e^{-1}) of the initial M_{xy} magnetization is left. The T_2 value for WM and GM are around 90-100 ms.

By altering the timing between excitation, signal sampling and re-excitation different contrasts can be created, due to variation in T_1 and T_2 between tissue types. The time between subsequent excitations will from now on be referred to as repetition time (TR), the time between excitation and signal sampling will be referred to as echo time (TE). With a long TR and a long TE, T_2 -weighted contrast is created. With a short TR and a short TE, T_1 -weighted contrast is created. With a long TR and a short TE, the effects of T_1 and T_2 on the MR signal are minimized, and the resulting image contrast is known as proton density (PD).

1.1.1.5 Pulse Sequence Diagrams

To describe the timing and gradient moments of an MRI acquisition a pulse sequence diagram (PSD) is used. In the simplest case, four time-courses are

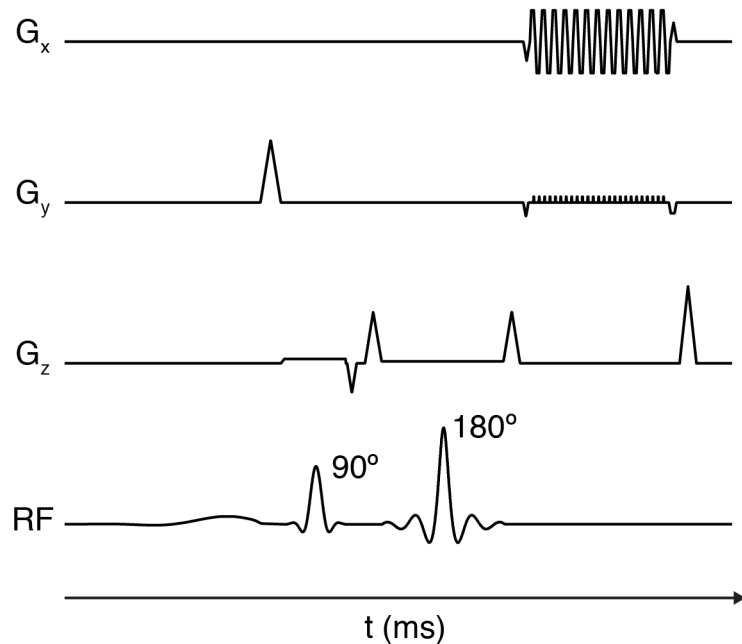


Figure 4. Pulse sequence diagram for the SE-EPI sequence.

depicted, three of which are describing the gradient amplitudes on the x, y and z axes (G_x , G_y , G_z), and one describing the RF pulse amplitude envelopes. The PSD can also be expanded to include receiver timing, receiver phase and RF phase modulation if a more detailed description of a sequence is required.

1.1.1.6 Slice selection

So far signal modulation has only been described in terms of relaxation properties. For spatial localization we also need to select a slice through an object. By applying a linear gradient in z, G_z , a corresponding linear change in Larmor frequency can be created according to the gradient strength.

$$f_z = \frac{\gamma}{2\pi} (B_0 + G_z(t) z) \quad [3]$$

where f_z is the resonance frequency [Hz] at position z , B_0 the main magnetic field (T), and $G_z(t)$ the gradient [T] at position z at time t . If a sinusoidal RF pulse is transmitted only spins located spatial location where the gradient creates the correct Larmor frequency will be excited. Changing the frequency of the RF pulse, whilst keeping the z-gradient, will allow us to move the selected slice in the gradient direction. Only exciting at one resonance frequency will however leave us with an infinitely thin slice, and virtually no signal to detect in our receiver coil. An RF pulse that has both a carrier frequency (choosing spatial location) and an amplitude modulation (creating a specific bandwidth) is therefore used:

$$B_1(t) = \cos(2\pi f_0 t) A(t) \quad [4]$$

where $B_1(t)$ is the RF field at time t [s], f_0 the resonance frequency, and $A(t)$ the amplitude modulation. For small flip angles, the Fourier transform of the amplitude modulation, $A(t)$, is a good approximation of the expected slice profile. Thus, a Sinc amplitude modulation would create a rectangular slice profile response, and a Gaussian modulation a Gaussian response. The full width half maximum (FWHM) of the spectral response determines the slice thickness.

By changing the carrier frequency of the RF pulse, slice position can be controlled. By changing the slice selection gradient, the mapping between the RF bandwidth (by the amplitude modulation) and spectral response (in the tissue) can be controlled, and thus the slice thickness.

1.1.1.7 In-plane spatial encoding

Once a slice has been selected, in-plane spatial encoding has to be performed. This is done via Fourier encoding. With a slice excited, all spins within the slice precess ideally at the same resonance frequency and with the same phase. If we now consider a 2D Fourier transform,

$$\mathcal{F}[s(x, y)] = S(k_x, k_y) = \iint_{-\infty}^{\infty} M_{\perp}(x, y) e^{-2\pi i k_x x} e^{-2\pi i k_y y} dx dy \quad [5]$$

where (k_x, k_y) corresponds to our position in the frequency domain, k-space, and $M_{\perp}(x, y)$ to the signal from the position x, y , within the plane. Having all spins in phase will then be equal to,

$$S(k_x, k_y) = \iint_{-\infty}^{\infty} M_{\perp}(x, y) dx dy \quad [6]$$

i.e. the sum of all available signal, which in turn corresponds to the most low-frequency component of the frequency domain. By convention, k-space is arranged such that the lowest spatial frequency components are at the center, with higher spatial frequency components further away from the origin. Hence, if a slice is excited and the receiver opened, the DC (sum of all available signal) of the image will be measured, positioned at the center of k-space.

To understand how k-space can be traversed, it is useful to consider how a linear gradient field acts upon a slice. If applied within the slice, e.g. in the y direction, it will create a linear distribution of Larmor frequencies in that direction; similar to what is shown in Equation 3. As a function of position y and time t , the accumulated phase becomes

$$\phi(y, t) = \gamma y \int_0^t G_y(t') dt' = 2\pi k_y y \quad [7]$$

where $\phi(y, t)$ is the accumulated phase at position y due to the onset of gradient G_y over time t . The measured signal can now be characterized as

$$S(k_x, k_y) = \iint M_{\perp}(x, y) e^{-i\phi(y, t)} dx dy \quad [8]$$

i.e. by applying a linear gradient in the y direction for a limited amount of time we can traverse k -space in the k_y direction according to Equation 8. This procedure of applying a gradient for a short period of time, creating phase dispersion is referred to as phase encoding, which also results in a static step in k -space of a certain size. By applying a second gradient, perpendicular to the G_y gradient, the corresponding shift in k -space along the k_x and k_y directions become

$$S(k_x, k_y) = \iint M_{\perp}(x, y) e^{-i\phi(x)} e^{-i\phi(y)} dx dy \quad [9]$$

We have now methods for moving freely in both the k_y and the k_x of k -space, controlled by the gradients on the corresponding axes. While creating a static offset in k -space is referred to as phase encoding, the act of sampling while moving in k -space is referred to as frequency encoding. For the majority of sequences the k -space traversal and sampling is done on a rectilinear grid, with an initial phase encoding in the k_y direction followed by a perpendicular sweep in the k_x direction. This process will be repeated until the whole desired grid has been traversed. By controlling the sampling density of k -space, different FOVs can be created, while controlling the extent of the acquired k -space, different image resolutions can be chosen. For 3D sequences, an additional phase encoding direction is applied in the k_z direction, and an inverse 3D Fourier transform is used in the reconstruction.

1.1.2 Echo Planar Imaging

Echo Planar Imaging (EPI) is a fast image acquisition technique that was invented in 1977 by Sir Peter Mansfield (4). While the majority of MRI pulse sequences require multiple RF excitations to form an image, EPI, in its simplest single-shot variant, requires only one RF excitation. This due to that the entire k -space, for one slice, is traversed during the EPI readout, allowing one full volume to be acquired each TR. Numerous advanced imaging methods today depend on EPI imaging, such as diffusion-weighted (5,6), functional (7,8), and perfusion imaging (9). While the high temporal resolution of EPI is used to image physical processes such as blood oxygenation in fMRI and susceptibility changes in perfusion imaging, it is the ability to acquire one image per excitation that is the main benefit for diffusion-weighted imaging.

In most applications it is more meaningful to discuss EPI as type of readout strategy, rather than as a specific sequence, since it is non-specific in terms of image contrast. Depending on RF and other magnetization preparation pulses, EPI can be either a gradient-echo sequence or a spin-echo sequence. For the diffusion imaging part of this thesis, a spin-echo EPI readout with a diffusion preparation is

used. For the motion navigator part of this thesis, gradient-echo EPI readouts are used.

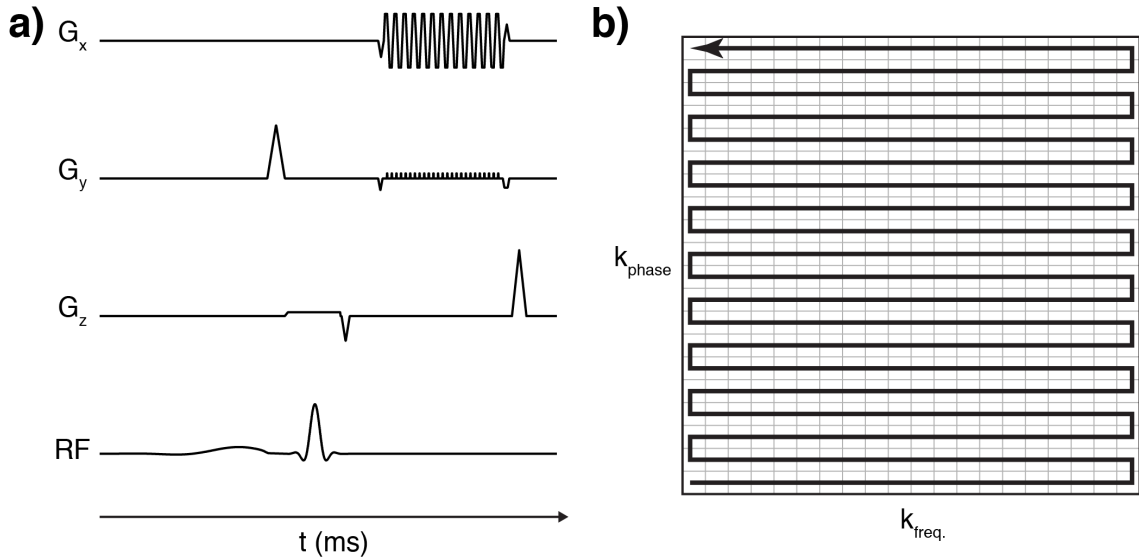


Figure 5. Echo planar imaging pulse sequence diagram a) and k-space trajectory b).

1.1.2.1 Sequence/Acquisition

During an EPI data readout, multiple k-space lines are acquired by using a series of bipolar gradients on the readout (or frequency encoding) axis, and a series of short and small trapezoidal blips on the phase encoding axis. This results in a train of gradient echoes that together covers a fully sampled center portion of k-space. This can be compared to other fast imaging techniques such as ss-FSE that rely on multiple RF refocusing pulses to do the same thing. Avoiding multiple RF pulses is advantageous for several reasons. First, SAR (patient heating) is less of an issue, the echo train does not have to fulfill the CPMG condition (5,10) for the k-space lines to be reliably in phase with each other, and the EPI readout is much shorter than a corresponding RF refocused readout for the same echo train length (ETL).

Spin-Echo EPI and especially Gradient-Echo EPI are however prone to artifacts. Some of these artifacts have to do with system imperfections, others with intrinsic properties of the method itself. Gradient delays (i.e. timing errors of a few μs) cause ‘Nyquist ghosting’ artifacts in the reconstructed images if not dealt with correctly. This is due to misalignments between echoes read with positive and negative gradient lobes. Throughout this thesis, these ghosting artifacts have been removed by using an entropy-based post processing reconstruction technique (11) based on work from Clare (12).

The chemical shift artifact, which is due to a difference of ~ 3.5 ppm in resonance frequency (~ 430 Hz at 3 T) between water and fat, manifest itself normally as a

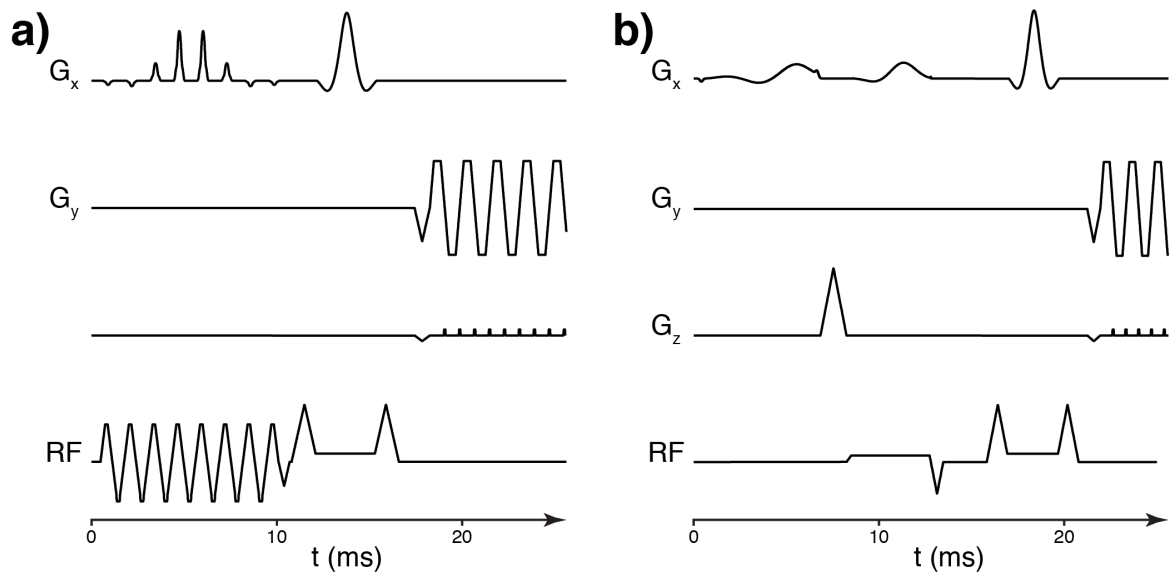


Figure 6. a) Water only excitation (using a Spectral-Spatial RF pulse). b) A leading spectrally selective saturation pulse (ChemSat) followed by a spatially selective excitation

slight misplacement (extent depending on rBW) of the fat signal in the frequency encoding direction for regular non-EPI acquisitions.

For EPI, this chemical shift artifact will appear a bit differently. Data points sampled in the frequency encoding direction are separated by $\sim 4 \mu\text{s}$ (rBW ~ 250 kHz for a standard EPI readout) and only sub-voxel shifts between fat and water will appear. In the phase encoding direction on the other hand, the duration between two consecutive data points is equal to the duration of one readout lobe (~ 1 ms) resulting in a pseudo receiver bandwidth (prBW) of ~ 1 kHz. This results in a displacement of fat of around 25-30% of the FOV, rendering images unusable for diagnostic purposes. It is therefore important to carefully select either fat or water magnetization (but not both) in EPI imaging, either via spectrally selective RF excitation or by fat (or water) suppression techniques.

An RF excitation pulse that is both spectrally and spatially selective (13-16) commonly performs this task, and is what is implemented in many clinical systems (a.k.a. SPECTral-SPatial, or SpSp RF-pulses). Common for many SpSp RF pulses, is that they have good spectral selectivity, but a rather crude spatial selectivity (i.e. slice profile). This is because the RF sub-pulses that determine the spatial selectivity have to be short with few side lobes to allow for their amplitude modulation within the given spectral envelope. With SpSp it is also difficult to acquire thin slices (< 3 mm) due to gradient system limitations. If thinner slices are desired, the combination of two RF pulses may be used to achieve the same goal, where the first RF pulse is spectrally selective (but spatially non-selective), a.k.a. a

ChemSat RF pulse, followed by an RF excitation pulse that may be spatially well-defined, but not spectrally selective.

In order to increase the temporal resolution, e.g. for fMRI and perfusion, or as a way to reduce TE for diffusion-weighted scans it is possible to combine EPI with partial Fourier techniques such as Homodyne (17) or POCS (18), along the phase encoding direction. A typical EPI scan, which is combined with a partial Fourier data reduction, would require approximately 16-24 k-space lines beyond the 50% data that is required from a pure theoretical standpoint (assuming that k-space is a Hermitian matrix), for a successful reconstruction. Throughout this thesis, the POCS reconstruction has been method of choice when partial Fourier acquisitions have been used.

1.1.2.2 Parallel imaging and distortion reduction

In addition to chemical shift artifacts, the low prBW in the phase encoding direction makes EPI sequences also extra sensitive to other sources of off-resonances such as susceptibility variations, B_0 -field inhomogeneities, and eddy currents. This leads to geometric distortions and signal dropouts in the image. Reducing the off-resonance sensitivity is therefore crucial for EPI in order to get images that are as geometrically faithful as possible. This can be done by using e.g. multi-shot (19) EPI readouts, parallel imaging (e.g. GRAPPA (20), and SENSE (21)), or by reducing the echo-spacing (e.g. RS-EPI (22) and SAP-EPI (23)). The amount of local spatial displacement relates to sequence parameters and B_0 field variation as

$$d_{pe}(\mathbf{r}) = \frac{\gamma}{2\pi} \frac{FOV_{phase}}{R} T_{esp} \Delta B_0(\mathbf{r}) \quad [(\text{m})] \quad [10]$$

where $d_{pe}(\mathbf{r})$ denotes the displacement of tissue at spatial location \mathbf{r} (unit: [m]), R is the parallel imaging acceleration factor, T_{esp} the duration between consecutive data-points in the phase encoding direction, and $\Delta B_0(\mathbf{r})$ the off-resonance field at spatial location \mathbf{r} . To reduce these geometric distortions, an initial approach would be to reduce the FOV in the phase encoding direction and match that with the narrowest part of the imaged object. Another option is to use parallel imaging methods such as GRAPPA and SENSE to lower the distortions by a factor of R .

Parallel imaging is based on the fact that if there are multiple receivers (each with a high local sensitivity) around an object, undersampled data that breaks the Nyquist sampling criteria can be restored by modeling the receivers and their known sensitivities as an overdetermined system of equations. This system can then be solved in a least squares sense, either in the image domain (SENSE) or in k-

space (GRAPPA). R in Equation 10 is the parallel imaging acceleration, or sometimes reduction factor, and denotes by what factor the data is undersampled.

With an acceleration factor of 2 a 50% reduction in image distortions can be produced and $R = 3$ would give a reduction to 33%, and so on. Although the distortion levels will be lowered further as R increases, there are diminishing returns. Going from $R = 1$ to 2 will be a 50% reduction, from $R = 2$ to 3 a further 17% reduction, from $R = 3$ to 4 an additional 8% reduction. Using higher acceleration factors is also not viable from an image quality perspective, as the SNR would drop and the parallel imaging related noise (a.k.a. g-factor noise) would be unmanageable.

To reduce the image distortions beyond what is achievable with an R of ~ 2 -3, other approaches are necessary. One approach is to reduce the T_{esp} by shortening the readout duration in the frequency encoding direction. This is accomplished by only scanning a partial, or segmented, part of k-space in the k_x direction. Either in a venetian blind fashion as in RS-EPI (22) or in a PROPELLER (24) fashion as in SAP-EPI (23). This reduces the T_{esp} and consequently also over all image distortions. Only acquiring a small portion of the sought k-space

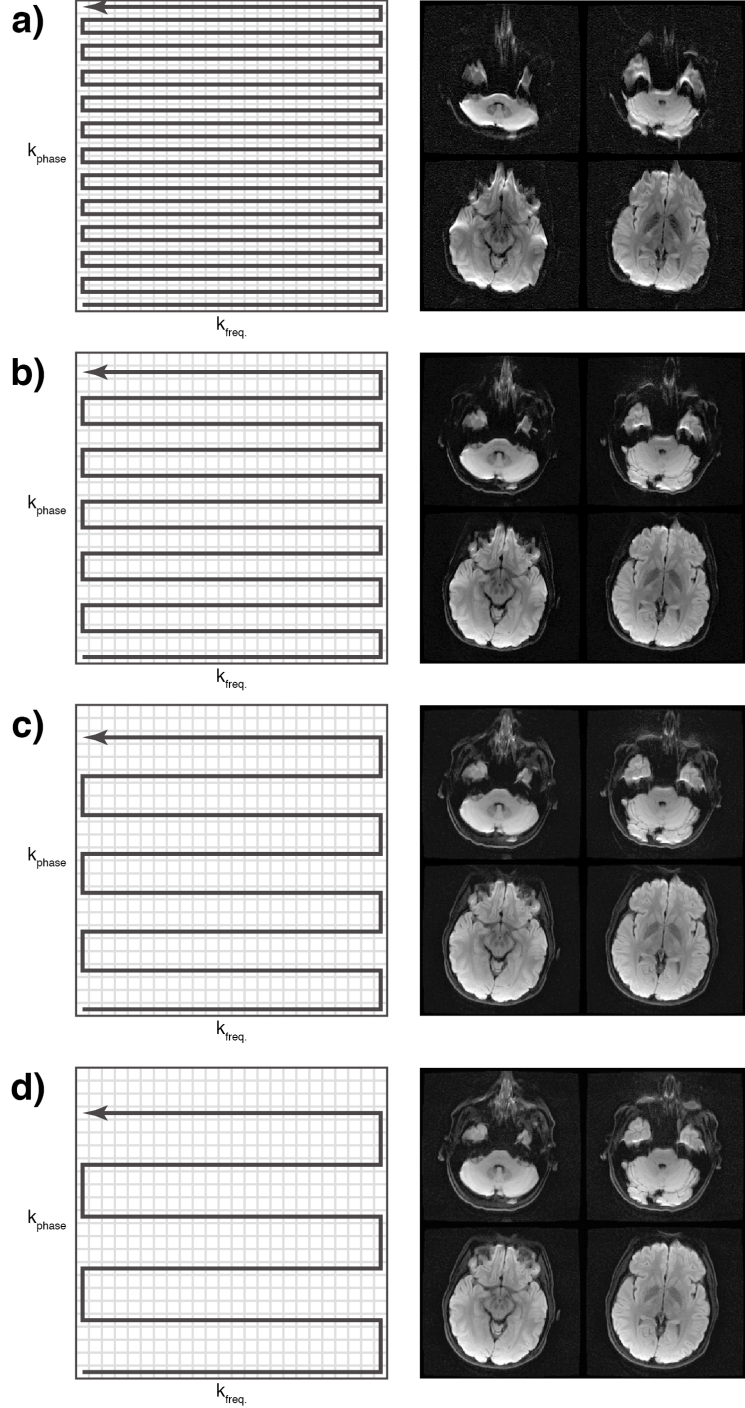


Figure 7. Parallel imaging acceleration factors of a) $R = 1$, b) $R = 2$, c) $R = 3$, and d) $R = 4$, yielding different distortion levels.

requires multiple acquisitions in order to have a complete image, hence the total scan time will be increased. For SAP-EPI (with its rotating EPI blades) the distortions will vary with the direction of the phase encoding direction of each blind (causing blurring in the final images if not accounted for (25)). For RS-EPI, the distortion is unidirectional as in regular EPI, since the phase encoding direction does not change across blinds.

1.1.2.3 Pulse programming and reconstruction

All data processed and presented in this thesis has been reconstructed using in-house algorithms and data processing methods. The major part of the images reconstructed has been performed using MATLAB (MATLAB, The MathWorks, Inc., Natick, Massachusetts, United States) with mexed C and/or C++ routines where necessary for speed reasons. Pulse sequence programming has been carried out in EPIC (Extended Programming In C, GE Healthcare, Milwaukee, Wisconsin, United States), which is a proprietary programming language for pulse sequence development for GE MR systems.

1.1.3 Diffusion-Weighted Imaging

1.1.3.1 Diffusion

Diffusion, as first observed when looking at pollen particles in water by Robert Brown in 1828 (26), is the random motion of particles due to their inherent thermal energy. This motion, also called Brownian motion, was later more theoretically described by Albert Einstein in 1905 (27) where he described it as a mean square displacement $\langle x^2 \rangle = 2Dt$, over a certain time t , scaled by a diffusion coefficient D [m^2/s]. That is, for a solution with a certain value for D the distribution of particles, compared to their initial position, will broaden over time. In the case of Einstein and Brown they assumed a homogenous medium, i.e. the diffusion process is equal in all spatial directions. This is however not always the case when observing diffusion in biological tissues. Diffusion without directional dependence is referred to as isotropic diffusion, while if a directional dependent variation exists in the tissue the diffusion will be referred to as anisotropic.

Since calculated diffusion coefficients can be influenced by e.g. tissue perfusion and partial volume effects, they are often referred to as apparent diffusion coefficients (ADC) (28). A parametric map showing ADC values are calculated by acquiring a minimum of two images, identical except one has been sensitized to diffusion. The amount of sensitization, or diffusion weighting, is denoted by a factor b along some gradient direction $\mathbf{q} = [q_x, q_y, q_z]$. The relative signal between the two images, S_0 and S_1 , becomes

$$S_1 = S_0 e^{-bD} \quad [11]$$

where b is related to the strength and duration of the diffusion gradients (cf. below). Rewriting this equation, the ‘apparent diffusion coefficient’ ADC (or D) is obtained by

$$\text{ADC} = D = \frac{\ln(S_1/S_0)}{-b} \quad [12]$$

For a tissue with non-isotropic diffusion the ADC will depend on the direction \mathbf{q} of diffusion sensitization for image S_1 . In order to have an ADC map that describes the isotropically averaged ADC (or mean ADC), several diffusion-weighted images (DWIs) have to be acquired along different directions in space. The acquired DWIs can either be combined using complex geometrical averaging or fitted into some 3D model of the diffusion process, from which estimates about mean diffusivity later can be derived.

1.1.3.2 Diffusion Tensor

The most common 3D model for diffusion in-vivo is the diffusion tensor model suggested by Basser et al. in 1994 (29,30), where the diffusion process is geometrically modeled as ellipsoids (one per voxel). Mathematically, this ellipsoid corresponds to a positive definite 2nd order tensor, which is a symmetric 3x3 matrix, \mathbf{D} , with six unique elements

$$\mathbf{D} = \begin{bmatrix} D_{xx} & D_{xy} & D_{xz} \\ D_{yx} & D_{yy} & D_{yz} \\ D_{zx} & D_{zy} & D_{zz} \end{bmatrix} \quad [13]$$

As the tensor is positive definite three real positive eigenvalues, λ_{1-3} , exists (with corresponding eigenvectors, \mathbf{e}_{1-3}), corresponding to the radii of the principal axes of the diffusion ellipsoid. We now have an alternative way of describing the average diffusion ($\text{Trace}(\mathbf{D}) = \lambda_1 + \dots + \lambda_n$), with

$$\langle \mathbf{D} \rangle = \frac{\text{Trace}(\mathbf{D})}{3} \quad [14]$$

For the mean ADC map, or $\langle \mathbf{D} \rangle$, which is a measure of the average diffusion at a certain location, typical values for brain tissues are: cerebrospinal fluid (CSF) $2.94 \times 10^{-3} \text{ mm}^2/\text{s}$, gray matter (GM) $0.76 \times 10^{-3} \text{ mm}^2/\text{s}$, white matter orthogonal to

fibers (WM_{\perp}) $0.45 \times 10^{-3} \text{ mm}^2/\text{s}$, and white matter parallel to fibers (WM_{\parallel}) $0.95 \times 10^{-3} \text{ mm}^2/\text{s}$.

As there is a directional dependence associated with white matter fibers, i.e. water diffuses more easily along nerve fiber bundles than orthogonal through them, a measurement of diffusion anisotropy is needed. The most common measurement today is fractional anisotropy index (FA), defined as,

$$FA = \sqrt{\frac{3 \sum_{i=1,2,3} (\lambda_i - \bar{\lambda})^2}{2 \sum_{i=1,2,3} \lambda_i^2}} \quad [15]$$

where λ_{1-3} denotes the three eigenvalues and $\bar{\lambda}$ the mean. FA ranges between 0 and 1, where 0 is isotropy (i.e. the tensor describes a sphere), and 1 full anisotropy (i.e. the tensor only extends into one dimension). More realistically, in anisotropic areas the tensor would be expected to describe either a cigar shape, $\lambda_1 > (\lambda_2, \lambda_3)$, or a saucer, $(\lambda_1, \lambda_2) > \lambda_3$. Given an FA map the eigenvector corresponding to the largest eigenvalue can be used to color-code the data to visualize the principal direction of diffusion. By convention this is done with red indicating left-right, green anterior-posterior, and blue inferior-superior.

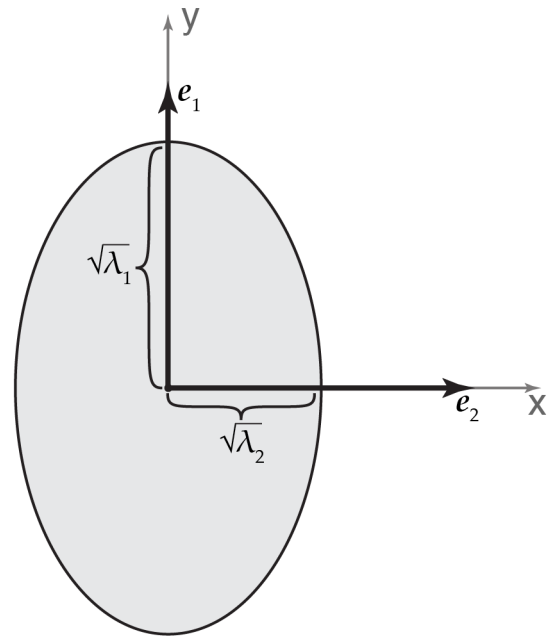


Figure 8. Relationship between the diffusion ellipsoid, eigenvalues and eigenvectors. The square root denotes the RMS displacement of water molecules

1.1.3.3 Diffusion-Weighted Imaging

In order to acquire multiple diffusion directions and many slice locations within a reasonable scan time, a fast imaging sequence is desired for diffusion-weighted MRI. Combining diffusion weighting (i.e. adding diffusion preparation gradients) with single-shot EPI therefore comes naturally, and is currently the preferred sequence, both in a clinical and research context. In 1965, Stejskal and Tanner (6) showed that the MRI signal could be made sensitive to the self diffusion of water if large bipolar gradients were added around the refocusing pulse of a spin-echo sequence. Spins dephased by the gradient before the refocusing pulse would be rephased by the gradient after in the absence of diffusion. For spins in areas with

high diffusion, the dephasing and rephasing would not cancel out and the signal would drop as an effect of the incoherent phase. The amount of applied rephasing and dephasing could be controlled via the b-value

$$b = (\gamma \cdot G \cdot \delta)^2 \cdot \left(\Delta - \frac{\delta}{3} \right) \quad [16]$$

where G is the gradient amplitude (T/m), δ the duration of the applied diffusion encoding gradients and Δ delay between the two gradients.

By increasing the b-value, a pulse sequence can be made more sensitive to diffusion up to a point where the diffusion gradients drives the signal below the noise floor of the image. A typical b-value for an adult patient undergoing a neurological exam is 1000 s/mm², which corresponds to a ~60% loss of signal in the healthy brain parenchyma.

Due to the insertion of the diffusion preparation between the RF excitation and data (EPI) readout, the signal becomes T₂-weighted, with a TE around 65-95 ms and a total sequence duration per slice of ~110-120 ms. With a typical slice thickness of 3-4 mm and a common whole brain coverage of 150 mm, a TR that can fit all slices needs to be larger than about 4500 ms.

An unwanted side-effect of the applied strong diffusion gradients, intended to reduce the magnitude signal only, are *eddy currents* that are formed in the magnet. This results in an added field on top of the spatial encoding x-y-z-field. The eddy currents flowing in the magnet exponentially decay at different time constants, the longest of the order of ~1 s. The long-term (and perhaps dominant) eddy currents

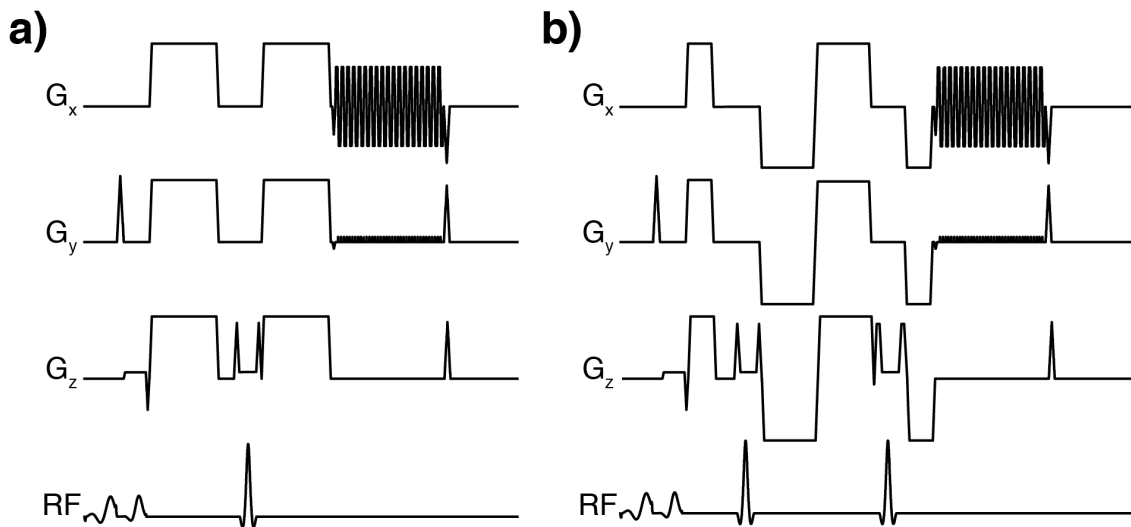


Figure 9. a) Stejskal-Tanner diffusion preparation. b) Twice-refocused diffusion preparation.

can often be approximated as being constant during the 20-40 ms long EPI readout, which makes them appear as constant gradients on x , y or z axes. These extra “gradients” induces translation, shear, and scaling of data, the amount of which is unfortunately dependent on the direction of the applied diffusion gradients (31). This can be dealt with via post processing, real-time field correction, or by applying an alternative diffusion preparation such as the twice-refocused preparation suggested by Reese et al. in 2003 (32). With modern gradient system designs, the eddy current effects in the diffusion data is low/moderate, why only the classical Stejskal-Tanner preparation has been used for the experiments in this thesis. This, in the interest of reduced TE, a better slice profile, and lower SAR compared to the twice-refocused diffusion preparation.

1.1.3.4 Phase correction

With the strong gradients creating the diffusion sensitization of molecules moving on the micro meter scale it follows that all other forms of motion within the FOV strongly affects the complex valued MR signal. Brain motion creates spatially non-linear low-frequency phase variations in the presence of diffusion gradients, and these phase variations varies unpredictably from excitation to excitation. It is therefore not possible to combine diffusion-weighted data from different excitations without taking this phase effect into consideration. These problems are most apparent in the lower part of the brain, where the cardiac-induced brain

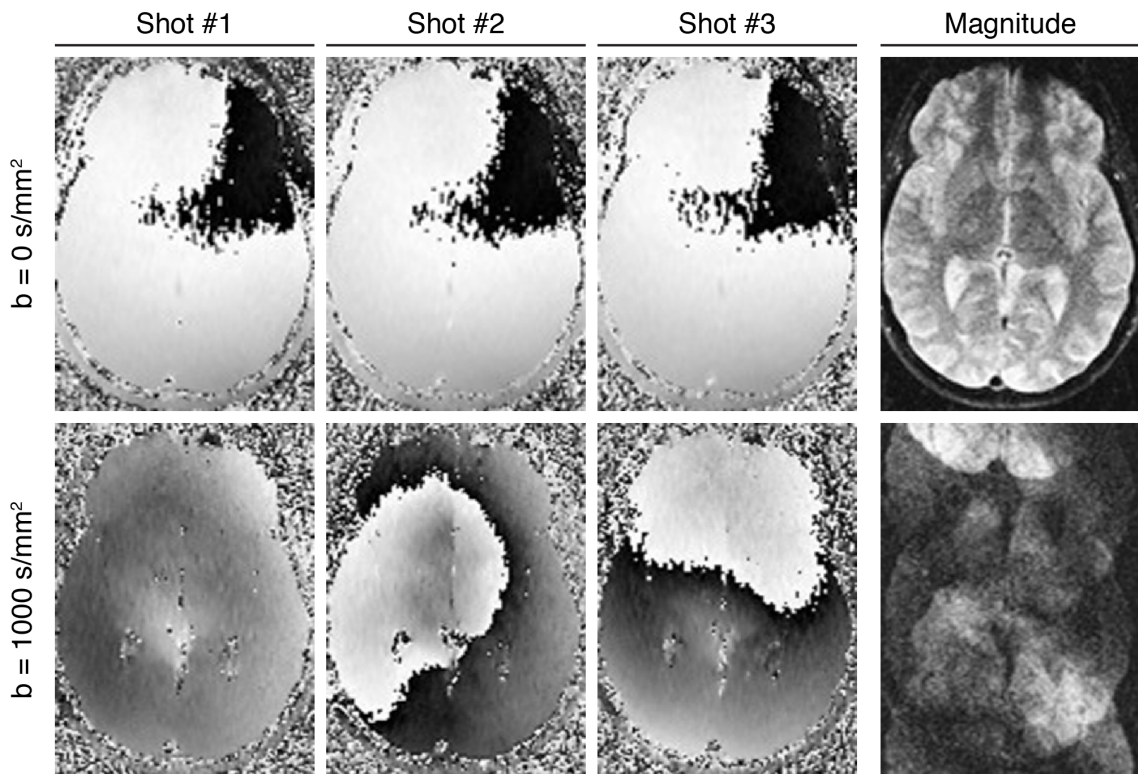


Figure 10. Three consecutive excitations without diffusion-preparation (upper row), and with diffusion-preparation (lower row). Complex combined images (right panel)

motion is the strongest. This motion-induced unwanted non-linear phase in the image domain corresponds to shifts and blurring in the frequency domain (k-space). For single-shot EPI, this phase is of little issue, since it is the same for the entire k-space and simply removed in the image domain by taking the magnitude of the complex DWI. For a multi-shot diffusion-weighted acquisition (which we might want to do to reduce the geometric distortions), the k-space segments acquired become on the other hand displaced in some random amount and direction (and also randomly blurred). This makes it very difficult to combine the multi-shot data into a consistent full k-space, why strong image ghosts will occur. An older remedy to reduce problems with phase variations has been to use pulse gating with diffusion acquisitions, thereby avoid imaging during the part of the cardiac cycle when the brain motions are large (33,34). Although effective in removing signal dropouts, pulse gated diffusion-weighted MRI scans has declined due to the increased scan time it brings and is no guarantee against the ghost inducing diffusion phase.

The simplest, and clinically most robust, way to avoid the phase issue is to acquire DW ss-EPI with a realistic acceleration factor of $R = 2$ or 3 using SENSE (35) or GRAPPA to reduce distortions. However, for higher image resolution or for lower distortion levels, multi-shot acquisitions may still be necessary.

Frameworks for data reconstruction of multi-shot interleaved diffusion data have been suggested, e.g. Atkinson et al. (36,37), Liu et al. (38,39), and Aksoy et al. (40). However, the reconstruction problem is indeed difficult, even if the correct phase field would be known, since areas of undersampling might still remain in k-space. There are iterative techniques that using non-Cartesian parallel imaging is able to essentially fill in the missing k-space data in the reconstruction.

Even for DW ss-EPI, the image phase of each DWI can be of value to keep. When combining reconstructed DWI data, e.g. images for many diffusion directions into one mean diffusion-weighted image (a.k.a. iso-DWI), the simplest approach is to take the magnitude of each diffusion-weighted image, and then perform an average (preferably the geometric average) to yield an iso-DWI. The drawback of this is that the magnitude operation makes the noise distribution Rician, instead of Gaussian with zero mean, which leads to an iso-DWI with pronounced noise floor that gives a hazy appearance. Alternatively, one can keep the DWI data complex and perform a complex averaging of the acquired DWIs. This makes the noise of the iso-DWI to converge towards zero, provided the undesired diffusion phase is first removed by some phase correction method.

The phase correction approach used throughout this thesis work to remove the diffusion phase in the data is based on the removal of low frequency phase components through phase self-navigation introduced by Pipe for DW-PROPELLER reconstructions (41). A phase self-navigator is created by Fourier transforming a copy of the image data into the frequency domain, where a triangular filter is used to select only low frequent components. The navigator is then transformed back into the image domain where the data is conjugated and the magnitude normalized. Doing a point wise multiplication between the original complex image data and the navigator yields a removal of the low frequent phase contribution (leaving only the high frequent component of the phase that stems from noise). The width of the filter will determine the amount of phase removal. A too wide filter will be close to doing magnitude combination, while a too narrow filter could result in residual phase cancelations. In this thesis a filter width of 25% of the full k-space FOV has been used if not otherwise described.

It is also this spatiotemporally varying phase that increases the number of oversampling lines required for partial Fourier acquisitions. With too few extra lines, the diffusion phase may move the k-space peak outside the acquired k-space, making successful reconstructions impossible.

1.1.3.5 Navigators

In order to make use of the self-navigation technique described in the previous section some parts of the acquired data has to cover the central parts of k-space, i.e. the low-spatial frequency components of the data have to be included. This is the case for multi-shot and parallel imaging accelerated single-shot EPI. Unfortunately this is not the case for the DW-RS-EPI sequence, or the two pulse sequences presented in this thesis, DW-vGRASE (42) and 3D-MS DW-EPI (43). As none of these pulse sequences cover the center of k-space after every excitation, additional phase navigation data needs to be acquired. A simple approach to meet this demand is to acquire an additional EPI echo that captures the central parts, as suggested by Ordidge et al. (44) and Anderson et al. (45). An additional echo prolongs however the sequence time and thereby also the total scan time (alternatively, a reduced the number of slices is possible for a given TR). If an EPI phase navigator is acquired as a second echo with an RF refocusing pulse in between, the signal phase has to be carefully treated, following the work of Pipe in 2007 (46).

1.1.3.6 Signal loss, geometric distortions and noise

When applying diffusion sensitizing gradients the only signal change possible is decrease. With that comes that anything that goes wrong during a DWI acquisition

will result in a signal loss. That is, if data is lost during the acquisition there is no way to recover it neither with reconstruction or post processing methods and it have to reacquired or discarded.

As previously discussed the distortions can be reduced by using multi-shot, parallel imaging, and/or segmented readout approaches (cf. Eq. 10). For Cartesian EPI, distortion correction methods have gained some attention recently as software has becomes more accessible. To make this work for Cartesian EPI, two images with opposite distortion direction needs to be acquired, which prolongs the scan time (47,48). Unless two oppositely distorted images are acquired for each diffusion direction it is not possible to undo the signal pile-up that will occur for large distortions. This, even if a correct field map (ΔB_0) would be perfectly known. Signal pile-ups mostly arise near regions with air-tissue boundaries, such as around the inner ear and the sinuses.

Using propeller trajectories with an FSE train like DW-PROPELLER (49), the distortions can be removed entirely, but this sequence is not particularly SNR efficient compared to EPI and has not gained a wide acceptance although it is commercially available. Faster diffusion-weighted propeller variants have since then been proposed by the same authors, where the FSE readout has been replaced with a GRASE-like readout (50,51). Another diffusion-weighted propeller-type sequence option is an accelerated DW-SAP-EPI with distortion correction embedded in the reconstruction (25). Here the sequence itself is less sensitive to off-resonances compared to Cartesian EPI, and the residual distortions that remain can be largely removed in the reconstruction. This can be done without any additional data or ΔB_0 measurements by minimizing the geometrical shape differences between the blades, leveraging on the works of Andersson et al. (47) and Skare et al. (52).

With the heavy dephasing from the diffusion gradients, SNR becomes an issue for DWI. There is a trade-off between enough weighting for a clear representation of the diffusion processes and come too close to the noise floor, i.e. being able to separate tissue from the background. To keep the geometric distortions minimal, the highest possible rBW must be used. This goes against the goal of high SNR as SNR is proportional to $1/\sqrt{rBW}$. Even so, EPI is still more SNR efficient than a corresponding FSE PROPELLER readout.

1.1.4 Multi-Slab Imaging

With 2D pulse sequences, a slice is first excited and in-plane Fourier encoded using one phase encoding and one frequency encoding direction. The resolution in the

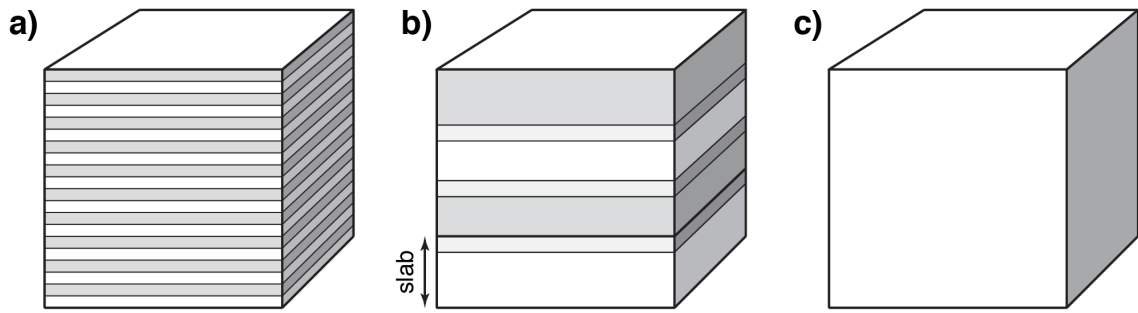


Figure 11. a) 2D, b) Multi-Slab, and c) 3D excitation

slice direction is usually lower than in the in-plane directions to save scan time. Multiple adjacent slices constitute one image volume, and the slice acquisition order is interleaved to minimize crosstalk effects. For 3D imaging, the RF pulse excites a volume instead of a slice, and the slice direction is instead spatially encoded with an extra phase encoding gradient. Since the quality (sharpness) of the excitation RF pulse is decoupled from the resolution in the ‘slice’ direction, 3D sequences are usually acquired with an isotropic spatial resolution, with also an increased SNR efficiency compared to a corresponding 2D scan. Acquiring a single volume DW 3D EPI with a Stejskal-Tanner diffusion preparation is very difficult and has never been attempted to our knowledge. This is both due to the unrealistic scan time and the nearly impossible task to undo the non-linear diffusion phase for each TR and slice encoded plane over such a large volume. Perhaps the most promising single-volume diffusion-weighted 3D sequence is based on SSFP, using a small accumulative diffusion gradient and a short TR. Here, the phase problems cause not ghosting but signal dropouts and are dependent on the diffusion direction. Recent work by O’Halloran et al. (53,54) has however shown a drastic improvement in the ability to reduce these dropouts.

There are also multi-slab sequences, where multiple (partially overlapping) thinner 3D volumes (or slabs) are combined into one full volume in the reconstruction. There are some well known examples of multi-slab imaging such as the sequential ordered MOTSA sequence used for time-of-flight MR angiography by Parker et al. (55) or the interleaved ordered 3D RARE sequence for T_2 -weighted imaging by Oshio et al. (56). Recently the multi-slab acquisition scheme has been explored for high-resolution diffusion imaging, using EPI based sequences (43,57,58), and spiral based sequences (59).

A move to a 3D multi-slab acquisition makes sense for two reasons. Firstly, the slice definition is not limited by the fidelity of the involved RF pulses, and the Fourier encoded slices within each slab produce perfectly rectangular slices

without cross-talk effects. Secondly, the SNR efficiency can be significantly increased with 3D multi-slab acquisitions compared to 2D.

1.1.4.1 Slab profiles

For 2D imaging it is easy to overlook that the resolution in slice selection direction is defined by the combined FWHM of the excitation and refocusing pulse(s) and that data is weighted according to the combined envelope of these RF pulses. To create a slice with a certain width, the excitation and refocusing pulses must be made wider than the prescribed slice thickness. The extent of the widening depends on the fidelity of chosen RF pulses. For a commercially available SpSp excitation pulse as an example, the default slice widening is 125% (60) in order to meet the prescribed slice thickness. This creates unnecessary cross-talk and could also cause a slice narrowing effects if a scan is performed in a low TR regime below about 3000 ms. Sharper RF pulses may be used, but require more SAR and leads to a slight increase in sequence time.

For multi-slab imaging the story is different. It is still true that a certain broadening of the RF pulse profiles is required to keep the slab thickness correct, but the reconstructed slices within each slab are still perfectly rectangular, albeit with some slice-to-slice signal intensity modulation due to the RF pulse profile. Moreover, it is necessary to overlap the slabs by some amount, so that the SNR does not fall too low in the slab boundaries. Unlike 2D imaging, where the slice profile is never directly seen, for 3D multi-slab the effective slab profile needs to be taken into account in the reconstruction for a seamless boundary between the slabs.

1.1.4.2 RF pulse design

For smaller flip angles ($< \sim 90^\circ$) the Fourier transform of the RF pulse envelope sufficiently approximates the slice profile. For larger flip angles, this approximation breaks down due to the nonlinearities of the Bloch equations. An efficient way to design RF pulses for any flip angle is to use the Shinnar-Le Roux algorithm (SLR) (61-65). An SLR algorithm solves an inverse problem of Bloch simulation by approximating the RF pulse by a series of hard pulses. An RF pulse can then be designed given a series of RF design parameters such as the flip angle, RF bandwidth (Hz), amount of ripple in the pass-band (i.e. inside the slice) and stop-bands (i.e. outside the slice) of the RF pulse, and transition width (Hz) etc. To achieve a sharp slice profile, the transition width should be as small as possible, and to obtain a short duration of the RF pulse, the RF bandwidth needs to be high, with system limitations. A high RF bandwidth does however increase the slice

selection gradient amplitude associated with the RF pulse, and so also the RF peak amplitude, the latter leading to an increased SAR.

Due to the gradient amplitude limitations of the system, there is therefore a minimum slice thickness limit for high bandwidth RF pulses. It is therefore easier to create sharp wide slabs than sharp thin slices. In the work presented in this thesis, SLR-optimized excitation and refocusing pulses have replaced the vendor provided RF pulses to achieve as sharp transitions as a necessary.

1.2 MOTION CORRECTION

Compared to other imaging modalities the acquisition time for a full MRI exam is slow. This is partly because multiple MR imaging contrasts are required that each require its own acquisition, partly because of physical limitations; biological relaxation processes that cannot be accelerated. Making MRI faster is a large active field of research and an important problem to solve in the interest of patient comfort. Patients are today usually only instructed to lie still, and the resulting quality of the examination is largely based on their cooperation.

There are however patient groups that, despite their best effort, cannot manage to stay still during the time that is required for one single acquisition. This could be claustrophobic patients, young kids, patients that suffers from stroke, mentally ill patients, or patients that simply are in too much pain or agony.

For these patients some form of motion detection and correction needs to be implemented with the MR acquisition. There are two main categories of motion correction, retrospective correction (where the data is corrected during the image reconstruction phase), and prospective correction (where the acquisition is updated in real-time to follow the motion of the patient). For brain imaging, the motion can be considered as predominately rigid and involves only translations and rotations. Motion outside the brain cannot generally be rigidly corrected as the tissues are also deformed to some extent.

1.2.1 Basics

The first thing that has to be done for any motion correction technique is to compare data between two time points and tell if there has been any change in positioning of the object. There are numerous ways this can be done depending on the nature of the acquired data. There are e.g. k-space approaches, image domain approaches, field-change approaches etc. which all require their own set of tools. This thesis will only use image domain approaches without external hardware.

1.2.1.1 Transformation

To understand how motion in the real world translates to, and is represented in, the ‘voxel world’ of a computer, some image processing basics is required. One common way of representing this connection is by using two arrays, one that contains the image data (i.e. the numerical value for each voxel), and one that contains x , y , and z real world coordinates for the corresponding voxels. By this approach a certain numerical value can be said to represent a specific position in 3D space. Either changing the image data, or the coordinates can perform a transformation.

If the image data is to be transformed, resampling is required. Depending on the application the interpolation method may differ, with the simplest being nearest neighbor interpolation. This is computationally fast but results in significant image quality degradation.

Often, linear and cubic interpolation kernels are used, where a target voxel is calculated by fitting either a linear or cubic function to the data in the neighboring voxels. Another common form of data resampling is spline interpolation, often cubic B-splines or a higher-order form of spline for even better interpolation results. As interpolation always results in slight image blurring, it is important to choose the right type of interpolation method for the right application. If repeated interpolations are to be performed, a high quality interpolation technique should be used, to minimize propagating image degradation, despite longer interpolation times. If data is to be transformed once to give an estimate of a gross error estimate, a faster interpolation such as linear interpolation may be the best option.

1.2.1.2 Cost function

By visual inspection of two images, it is often easy to tell whether motion has occurred between them. To quantify the amount of motion in 3D with high accuracy and without human interaction is however more difficult. A metric of how similar two images is therefore required, where the metric is a scalar number that increases the more different the two images are. This metric, or cost, is the output of some cost function f

$$\text{cost} = f(\mathbf{p}; R, I) \quad [17]$$

where R is a stationary reference image, and I is an image being transformed given a parameter vector \mathbf{p} . For the 3D case, \mathbf{p} will be a vector containing three rotations and three translations that we need to guess in an iterative manner until the cost is minimized. Although the cost function depends on R and I it is considered as

being a function of \mathbf{p} . An example of a cost function is the sum-of-squares (SoS) difference

$$\text{cost} = \sum_{i=1}^N (R(i) - I(i, \mathbf{p}))^2 \quad [18]$$

where N is the number of voxels in the transformed image I (assuming I and R have equal size) according to \mathbf{p} . Another possible cost function is to use normalized correlation. Sum-of-squares difference and correlation metrics work well with image data that have similar image contrast. When two images have different appearance, other metrics for motion should be used, such as e.g. mutual information (MI) (66).

$$\sum \left(\text{img1} - \text{img2} \right)^2 = \sum \left(\text{img3} \right)^2$$

Figure 12. Sum-of-squares cost function

With \mathbf{p} being a 6-dimensional vector, the task is to find the minimum of the cost function in its six-dimensional space. Ideally, we would like cost function to be smooth and quadratic with one global minimum. Due to noise, image artifacts and interpolation effects, also local minima will generally exist unfortunately. By using techniques such as e.g. a slight randomization of the resampling coordinates, the roughness of the cost function related to the interpolation kernel can be mitigated. To make the cost function closer to a quadratic and smooth (and thereby fast converging) function, the images to be registered are also usually smoothed prior to the motion estimation process. Strong smoothing ensures a fast convergence, but excessive smoothing also reduces the final accuracy. Therefore, two-pass approaches may be used, where the image data is first heavily smoothed to yield approximate motion parameters, $\mathbf{p}_{\text{coarse}}$, which can be used as starting guess for a second motion estimation pass using the same images with less smoothing applied.

1.2.1.3 Search algorithms

To avoid the computationally heavy, and inefficient, work of having to calculate the whole six-dimensional topology of the cost function, a search algorithm must be used to find the global minimum. The task for the search algorithm is to

iteratively execute the cost function, $f(\mathbf{p})$, for different candidates of \mathbf{p} and based on the variations of the cost and as quickly as possible find the way towards the optimal \mathbf{p} that corresponds to the global minimum. Ideally, a search algorithm should both require few steps and perform fast calculations each iteration, but it is very difficult to get both, and the search algorithms available tend to end up in one of two categories.

The first category contains those that require a lot of iterations, but where the computational burden of each iteration is small. An example in this is the Nelder-Mead downhill simplex method (67), also known as the *amoeba* method, which also the Matlab function `fminsearch` uses.

The other category of search algorithms is derivative-based methods, such as e.g. the Gauss-Newton method. For each iteration, the partial derivatives w.r.t. each parameter (in \mathbf{p}) of the cost function are calculated. This makes the function evaluation at each point \mathbf{p}_i more computationally heavy. However, for derivative-based search algorithm such as Gauss-Newton, the global minimum can be found in just a few iterations (instead of hundreds for Nelder-Mead) as both the direction and some form of distance information is given to the location of the global minimum from the current point \mathbf{p}_i . This distance information comes from the (approximate) Hessian of the function.

1.2.2 Retrospective motion correction

The term retrospective motion correction means that motion correction is performed after all MR data has been collected. This has historically been, and still is, the dominating type of motion correction for volume-to-volume image registrations in e.g. fMRI and DWI. The benefit is that the correction is performed as a generic post-processing step using software independent of the pulse sequence or MR vendor software environment. Retrospective corrections have proven to be very robust for EPI with image volume acquisition times of only a few seconds.

For retrospective motion correction to work well, data need to be acquired in such a way that small chunks of data can be reconstructed and used for motion estimation. An example of this is the PROPELLER technique where data is acquired in ‘blades’, narrow segments covering the center of k-spaces, which are rotated across TRs. The time it takes to acquire one blade is only a fraction of the entire scan time, and each blade will depict the entire image FOV with one high-resolution direction and one low-resolution direction. By comparing the blades the relative motion in between can be found and adjusted for prior to combining them to one full resolution image.

One disadvantage with retrospective techniques, and a major source of criticism, is the inability to correct for spin history effects. That is, if a slice has been excited and the patient/subject then moves its head, subsequent slice excitations may intersect the previously excited slice location. This will result in a drastically decreased effective TR leading to tissue saturation, especially for tissues with long T_1 .

1.2.2.1 2D DW-EPI

In a diffusion-weighted scan, one or more T_2 -w ($b = 0$ s/mm²) images and a larger set of diffusion-weighted ($b = 1000$ s/mm²) images are acquired. Using a sum-of-squares cost function, the similarly looking T_2 -w images may be aligned to one of them as reference. As reference, one may either simply choose the first among the acquired T_2 -w images, or as done in this work, choose the reference image based on image entropy. The idea behind this is that the image volume with the lowest entropy most of the time corresponds to the one with the least artifacts such as image ghosting from e.g. intra-volume motion.

In theory, the DWI data fit less well to a sum-of-squares (similarity) model for motion correction, since the diffusion anisotropy in the brain white matter (WM) makes the WM signal intensity to vary across diffusion directions. In our experience however, the DWI data is ‘similar enough’ to make the similarity based motion correction to work in practice, at least at $b = 1000$ s/mm² that is commonly used in the clinical routine and also in this work. For the alignment reference volume, a best suited DWI volume can be chosen by either again using the entropy metric or by simply selecting the DW volume with the highest mean intensity, given that motion in diffusion leads to signal dropouts.

Once all diffusion-weighted volumes have been registered to each other, the iso-DWI (i.e. geometric average over all diffusion directions) can be calculated. To calculate mean ADC or FA maps, the T_2 -w and DWI data also need to be aligned to each other. As the DWI and T_2 -w data have different contrast, it is not likely that the cost function gives its lowest value when the two images volumes are perfectly registered to each other. To register all data to the same space, the mutual information (MI) metric is better for this purpose, where the motion between the mean of the registered T_2 -w image volumes and the iso-DWI is determined, with the latter as reference.

For most clinical DWI scans, the TR of a DW-EPI scan is short enough that intra-volume motion can be assumed to be small enough to make the abovementioned volume-to-volume retrospective realignment reasonable. For patient groups associated with larger motion patterns such as small children and e.g. stroke

patients, retrospective correction is only expected to partially work, which increases the need for prospective techniques.

1.2.2.2 Diffusion-Weighted Multi-Slab Imaging

For diffusion-weighted multi-slab imaging, with a TR of about 3-6 seconds and about $N_{kz} = 10$ phase encoding steps in each slab, the temporal footprint for a diffusion-weighted volume becomes about 30-60 seconds, allowing for significant time for intra-volume motion. With overlapping slabs the DW 3D-MS EPI sequence is also more sensitive to motion, in comparison to 2D, from a spin-history and slab-combination point of view.

Recently, we proposed to address head motion for DW 3D-MS EPI in three steps (68). A first step is to do intra-slab correction, followed by inter-slab correction, and finally full volume-to-volume realignment as described in the preceding paragraph. The intra-slab correction estimates in-plane (2D) motion that occurs between k_z -phase encodes by performing 2D SoS image registration of the navigator echoes (always in $k_z = 0$). Once all k_z encodes have been corrected, slab-to-slab (inter-slab) realignment has to be performed, also this in 2D only. This step is necessary since the first intra-slab correction method does not guarantee spatial consistency between slabs. With inter-slab correction the overlapping area between adjacent slabs are compared and the relative positions adjusted. Once this has been performed, one whole volume is considered motion corrected (albeit only in 2D). Lastly, 3D SoS image registration is performed as above. For axial imaging, this will mean that nodding motion is left uncorrected, but this is not something that can be easily addressed retrospectively within one volume. Prospective motion is therefore of great interest to the DW 3D-MS EPI sequence.

1.2.3 Prospective correction

All types of motion correction that adjusts for patient movements during the data acquisition are referred to as prospective correction. The first prospective correction approaches allowed the acquisition to follow basic physiological processes such as the cardiac cycle, or the respiratory cycle (by triggering the acquisition to a certain part of the cycle and blocking other parts). This is often used for cardiac and liver imaging where the physiological motion is more prominent than for neurological imaging. The benefit of cardiac gating to avoid brain motion for neurological DWI scans has been reported in several studies, e.g. Skare et al. (34). Still, it is not widely used today as much as it should perhaps, due to the prolonged scan time of gated diffusion-weighted imaging.

Prospective motion correction techniques to overcome head motion include the use of navigators interleaved with the host pulse sequence that acquire snapshots of the position of the head during the entire scan. These snapshots are processed in real-time and the motion estimates are sent back to the MR scanner and running pulse sequence to update the slice locations. An example of this is the PROMO navigator technique (69) that uses a set of orthogonal spiral readouts to detect motion deviations.

An alternative to navigators for real-time motion correction is to use external devices such as an optical camera mounted in the bore of the scanner that detects a marker on the patient/object (70-72). These methods do not interfere with the timing and duration of the main MRI sequence, hence does not affect the scan efficiency. It does however require some patient cooperation in order to keep the marker fixed with respect to the head position. Directly placing the markers on the skin may cause misregistration, as the skin is not guaranteed to exactly follow the motion of the brain. Other types of prospective correction techniques include gradient field detection systems such as the active marker approach by Ooi et al. (73). The work in this thesis will however only involve image-space navigators, interleaved with DW 3D-MS EPI as the host sequence.

1.2.4 Motion Navigators

With image navigators there is an inherent trade-off between how much time that should be spent on acquiring motion navigator data and image data. Depending on the host sequence, there are also limitations on where the navigator could possibly be placed. For e.g. a FSE sequence, the long readout (up to 300 ms) prevents navigator data to be acquired at a faster rate than ~3-4 Hz. For shorter host pulse sequences, the duration of the navigator becomes relatively large, which may imply a significant scan time increase. To allow for a frequent use of the navigator while not drastically reducing the scan efficiency, the navigator module must be very short. Undersampling the navigator's k-space trajectory using parallel imaging is one viable option. The most extreme case today is probably FID navigators (74), where only a few points (~30 us) are sampled and used to detect, but not correct for, motion.

As discussed earlier, for 2D EPI based sequences used for perfusion imaging, DWI and fMRI, all acquired at a relatively high temporal rate, 3D retrospective rigid body motion correction is possible between volumes. But the volumes themselves can also be used as self-navigation for prospective motion correction, such as the 3D PACE method (75), where the most recent volume is used to update the slice locations so that they follow the patients head with one TR lag.

The image space PROMO navigator for prospective motion correction has been combined with pulse sequences having large blocks of dead-time, during which longer navigator blocks can be played out without scan time penalty. Each navigator block in PROMO is about 50 ms, and today PROMO has been combined with 3D sequences such as IR-SPGR (BRAVO, MP-RAGE), T2-CUBE (SPACE) and T2-FLAIR CUBE (SPACE).

Another recently proposed navigator is the volume navigator (vNav) was suggested by Hess et al. for spectroscopy in 2011 (76), by Tisdall et al. 2012 for neuroanatomical imaging (77), and by Alhamud et al. for diffusion-weighted imaging (77) in 2012. While PROMO uses three orthogonal spirals, vNav use a full $32 \times 32 \times 32$ EPI volume with a even longer navigator duration of 275 ms.

PROMO and vNav require large amounts of information to accurately perform image registration and send the motion information back to the host sequence. For PROMO and vNav, the update block is ~240 ms and ~400 ms, respectively. In order to make these techniques more widely applicable for sequences without embedded dead-time, these blocks have to be shortened considerably. One way to accomplish this for vNav is to use multi-band RF pulses (78), i.e. RF pulses that excite multiple slices simultaneously. The vNav module can then be reduced to ~25 ms as demonstrated by Bhat et al. in 2014 (79).

1.2.5 Motion Fat Navigators

While both PROMO and vNav show promising results they are both using signal from water magnetization for the navigator data. With PROMO's three orthogonal planes saturation artifacts in the images generated by the host sequence may occur. Also, the amount of parallel imaging acceleration possible is limited in this water-signal based navigator data.

In many cases, the signal from fat (compared to water) is of less importance from a radiological perspective. Moreover, the T1-relaxation of fat is very short, making its M_z magnetization to recover quickly if perturbed. Selectively exciting the fat in the head, primarily the subcutaneous fat surrounding the head, has therefore become an attractive option for the purpose of motion tracking (80-82). The character and distribution of the subcutaneous fat also makes it extremely sparse in space. This has shown to allow for very high parallel imaging acceleration factors using both EPI readouts (83) and 3D GRE readouts (84).

For EPI host sequences, the use of fat navigators is well suited, as the fat magnetization must be saturated anyway to avoid strong chemical shift artifacts in the main imaging data. Adding a navigator readout block between the leading fat

saturation (ChemSat) RF pulse and the subsequent excitation RF pulse increases the total sequence time by only a small amount. Accelerated EPI readouts have been suggested for this, either with a 3D EPI readout (83) or with three orthogonal 2D EPI readouts (85).

With three orthogonal 2D EPI readouts, the fat signal will be represented as three orthogonal projections of the patient's fat head, in the axial, sagittal, and coronal views, respectively. By acquiring data in this way, and combining it with high acceleration, the total readout time can be below 10 ms, allowing a motion update frequency of ~10 Hz. Full 3D motion realignment is not possible straight away, since only motion in the three basal planes can be detected.

1.3 CLINICAL NEEDS AND OUTLOOK

1.3.1 Diffusion-Weighted Imaging

In 2012, Holdsworth et al. (86) presented a large scale study where the motion of 1600 pediatric patients during a DW-ssEPI sequence was examined. The motion corrupted DWI data were corrected retrospectively and the maximum motion that occurred during each scan was stored in a database. 816 (~51%) had minimal motion of 0-1 mm, but of these were 656 (~41%) acquired under general anesthesia (GA). Of the remaining 784 patients did 448 (28%) move 1-3 mm, 208 (13%) move 3-5 mm, 96 (6%) 5-10 mm and 32 (2%) more than 10 mm. With an average in-plane image resolution of ~1.8 mm, these numbers are large by comparison, and the need for prospective as well as retrospective correction techniques is apparent. Although GA is effective in avoiding motion it comes with several side effects and drawbacks, including healthcare costs, scheduling issues, patient safety, and patient comfort. Avoiding GA would be a great advantage for both patients and families.

1.3.2 Cost

The numbers above do not translate directly to adult patients but are also not too far off. In 2014, Andre et al. (87) presented a study where 175 MRI examinations were examined during one week of clinical neuroaxis (head, neck, spine) exams, with ~50% being emergency and in-patients, and ~50% outpatients. Out of these were ~31% classified as motion degraded, and in ~17% of the cases repeated scans were required. According to the authors, these numbers are even likely to be underestimated. An exact cost for a MRI examination is hard to estimate, but their figure of \$813/h seems reasonable (c.f. 6000 SEK/h at Karolinska Universitetssjukhuset, 2013-2014). An increase of only 5 min per examination due to motion, adds up to about ~\$1,900/scanner/week or ~\$100,000/scanner/year. The

ability to correct for patient motion is therefore not only a question of image quality and radiological confidence, but has also indirectly a significant impact on the hospital's budget.

2 AIM OF THESIS

Diffusion-weighted MRI provides detailed information about the diffusion processes occurring in our body, and has become an increasingly important MR contrast in the clinical routine, far beyond stroke imaging alone. In the neuroscience MR research community, it plays about as an important role as fMRI. Due to the semi-random diffusion phase from one TR to the next, 2D single-shot EPI has been the main sequence of choice. With that choice follows that many image volumes can be acquired in a short period of time, but also limitations in image resolution, geometric distortions and difficulties with thin and sharp slice profiles.

The aim of this thesis was to increase the isotropic spatial resolution of diffusion MRI via new acquisition strategies with maintained or reduced geometric distortion levels. The aim was also to guarantee that the effective resolution is preserved under patient head motion via methods of motion correction.

2.1 SPECIFIC AIMS

2.1.1 Study I – DW vGRASE

To develop a pulse sequence that can acquire low distortion diffusion-weighted data without multiple acquisitions or additional phase navigation.

2.1.2 Study II – DW 3D-MS EPI

To acquire multi-shot diffusion-weighted data at high isotropic spatial resolution without diffusion phase artifacts and reduced motion sensitivity by developing a new diffusion-weighted 3D multi-slab EPI sequence and a tailored image reconstruction chain.

2.1.3 Study III – DW 3D-MS EPI

To evaluate the performance of DW 3D-MS EPI in terms of SNR and scan efficiency, but also to benchmark the suggested method against currently available techniques (such as DW ssEPI).

2.1.4 Study IV – FatNav

To investigate the use, characteristics and limitations of an in-house developed image domain motion navigator depicting the subcutaneous fat around the skull.

2.1.5 Study V – Collapsed FatNav

To combine the use of DW 3D-MS EPI with fat navigation by exploiting the chemical saturation pre-pulse already existing in the DW EPI pulse sequence.

3 MATERIALS AND METHODS

3.1 MRI SYSTEMS

All data presented in this thesis have been acquired on two clinical MRI systems at the Department of Neuroradiology at Karolinska University Hospital. The first being a 1.5T system (DVMR45, GE Healthcare, Milwaukee, WI), the second a 3T system (DVMR750, GE Healthcare, Milwaukee, WI), using 8-channel receive only head-coil (Invivo, Hi-Res Head Coil, Invivo, Gainesville, FL). Phantom measurements were performed using the ACR MRI phantom (ACR MRI phantom, American College of Radiology, Reston, VA), if not specified otherwise.

3.2 DIFFUSION-WEIGHTED IMAGING

3.2.1 DW vGRASE

3.2.1.1 Sequence design

The GRASE pulse sequence (88) is a fast T₂-w sequence that is similar to an FSE or TSE readout, but with short EPI readouts between the refocusing pulses to acquire many more k-space lines per excitation. With this, a single-shot readout of k-space is possible with lower distortions compared to EPI. The vGRASE pulse sequence was proposed as an alternative to GRASE by Oshio (89) to separate the T₂-modulation of the EPI trains due to the long FSE train and the phase modulation from off-resonances along the frequency and phase encoding axes.

In this work, we have developed a diffusion-weighted version of the vGRASE sequence. This was done by modifying a DW-ssEPI stock sequence to allow for

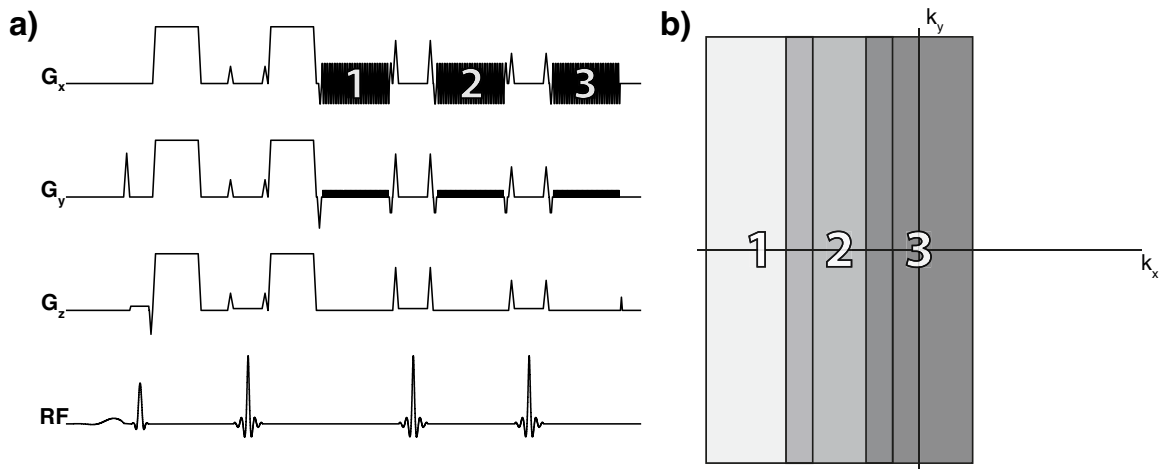


Figure 13. Pulse sequence diagram for DW vGRASE a), and b) corresponding readout ('blind') k-space coverage.

three RF-refocused EPI readouts following a single RF excitation pulse. In the interest of short TE, a standard Stejskal-Tanner diffusion preparation (6) was chosen over the eddy-current robust twice-refocused scheme (32). The k-space readout trajectory was similar to that of a five blind vGRASE sequence (89), with each k-space blind corresponding to one readout. To shorten the sequence readout time, T_{\min} , a partial-Fourier k-space sampling in the frequency encoding direction was used. This reduced the five blinds to three, leaving $\sim 40\%$ of k-space to be synthesized in the reconstruction using POCS. The blind acquisition order was chosen to optimize the T_2 -w image contrast and the SNR of the high spatial frequencies of k-space. Therefore, the outermost blind in k-space was acquired first, the adjacent blind next, and the central k-space blind last. With the third blind covering the k-space center, the effective TE of the sequence (TE_{Eff}) became ~ 120 ms.

With a diffusion preparation and multiple RF refocused readouts the CPMG criterion (5,10) is no longer met, making spin-echo and stimulated echo pathways over the echo train to not add up constructively. To avoid stimulated echo interferences in the data, two measures were taken. First, the standard refocusing pulses were replaced with an 8 ms SLR optimized refocusing pulses (TBW = 5) (90). Second, the crusher gradients around the refocusing pulses were altered pair-wise to allow for only zero ordered (i.e. spin-echo) echo pathways.

Table 1: Scan parameters_{SDW vGRASE}

FOV	240×240 mm ²
Resolution	1.25×1.25×4.0 mm ³
Matrix _{Final}	192×192 (fe×pe)
Matrix _{Blind}	192×48 (fe×pe)
Slice _{Thickness}	4 mm
Slice _{Spacing}	0 mm
R _(GRAPPA)	3
NEX	3
N _{Slices}	21
N _{Readouts}	3
TR	4000 ms
TE _{Readout 1}	60 ms
TE _{Readout 2}	90 ms
TE _{Readout 3}	120 ms
b _{Human}	1000 s/mm ²
b _{Human}	300 s/mm ²
N _{T2w}	2
N _{DW}	15

3.2.1.2 Data acquisition

Human data were acquired from two healthy volunteers and phantom data from the ACR phantom. The sequence parameters for both MR systems can be found in Table 1.

3.2.1.3 Image reconstruction

In the presence of an uncontrolled diffusion induced phase over the object prior to the RF readout train on top the spatial phase encoding and transmit and receive RF phases, the phase accumulation over the train needs careful attention. This was described by Pipe et al. in 2007 (46) in the context of DW-PROPELLER. Hence, before the blinds can be combined, the phase that stems from the diffusion gradients and brain motion needs to be found. To do this, one must also use the phase of the T_2 -w ($b = 0$ s/mm²) vGRASE data without diffusion gradients applied.

The central blind of the T₂-weighted vGRASE data, and the central blind of the diffusion weighted scan, were first low-pass filtered using a triangular window (25% width of the full matrix size) (24), and a phase difference map, $\Delta\phi$, was calculated between the two central blinds. The phase difference map was removed from the first and third blinds and the conjugate of this map, $\overline{\Delta\phi}$, was removed from the second blind of the diffusion-weighted data. The procedure, illustrated in Fig. 14, was repeated for each slice and diffusion direction.

With the three blinds acquired at different echo times (60-120 ms), and with the

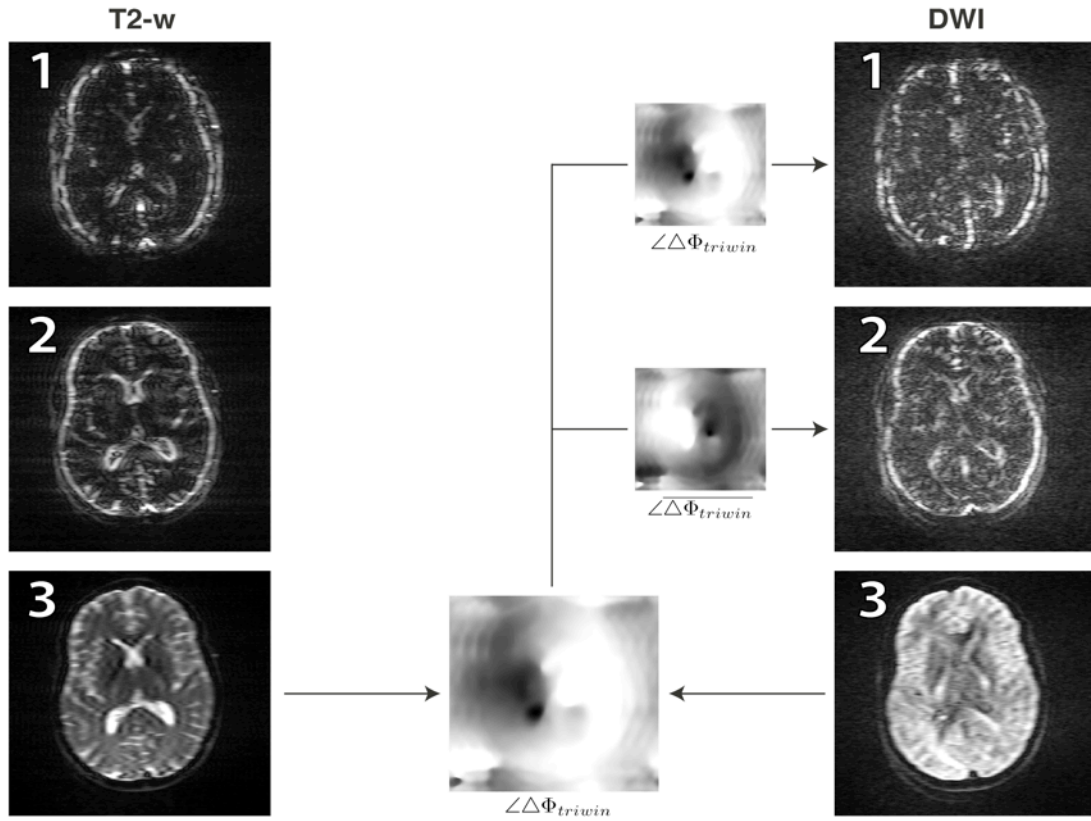


Figure 14. Phase correction procedure. A phase difference map is calculated between the third blind of the b₀ scan and the third blind of the DW scan, and then applied to the 1st and 3rd blind, while the conjugate is applied to the 2nd blind.

blind straddling the k-space center acquired last, the data becomes high-pass filtered due to T₂-decay between the three readouts. This acts as a form of sharpening filter in the image domain. To dampen this high-pass filtration, relative intensity scaling factors were determined for each blind by comparing the signal intensities in the overlapping regions between the blinds.

3.2.2 DW 3D-MS EPI – General

3.2.2.1 Diffusion weighting and Multi-Slab

Adding a diffusion preparation to a multi-slab acquisition, several pulse sequence modifications are required. Traditionally, the diffusion weighted EPI sequence is using an SpSp RF excitation pulse. Good spectral separation and acceptable pulse duration (~14 ms on a 1.5T system) has made it a workhorse, adequate for clinical routine. The slice profile is however not sharp enough for multi-slab imaging. The choice therefore becomes to either design an excitation SpSp with a better slice profile, or using a combination of a non-spatially selective chemical saturation pulse followed by a sharp SLR pulse with a good slice/slab profile. In this work the latter was found preferable. Since the acquired slabs are ~8-10 times the slice thickness of a 2D scan the RF bandwidth may be higher without reaching gradient system performance limitations. As all spatially selective RF pulses included in a sequence contribute to the final slice profile, one must provide optimal slice selectivity for both the excitation and refocusing RF pulses.

The vendor provided RF pulses were therefore replaced with spatially sharper, in-house generated, SLR optimized RF pulses for both refocusing and excitation. The 5.0 ms long default excitation RF pulse was replaced with a 6.2 ms SLR pulse having a time-bandwidth product, TBW, of 8. Similarly, the 3.2 ms standard RF refocusing pulse was replaced with an 8.4 ms SLR pulse, also with a TBW of 8. A further increase in TBW would have implied yet sharper slices, but at the expense of longer RF pulse durations and a further increase in TE.

3.2.2.2 Sequence design

With experience from DW-vGRASE, the DW 3D-MS EPI sequence was developed with two EPI readouts (instead of three for vGRASE) with a refocusing pulse in between. Unlike vGRASE, each EPI readout covered all of k-space in k_x and k_y . Before and after the first EPI readout, dephasing and rephasing phase encoding gradients were added in the z direction for 3D Fourier encoding of the slab. The second EPI readout was used for diffusion phase navigation without additional Fourier phase-encoding gradients. Fourier encoding a volume (slab) with a z-FOV as thin as 15-30 mm requires large gradient areas of the z phase encoding gradient. This z-dephasing gradient is placed right after diffusion preparation and also after the first RF refocusing pulse with its crusher gradients. The crusher gradients around the RF refocusing pulses are necessary to spoil the signal from the unwanted excitation from the RF refocusing pulse arising due to the non-rectangular slice profile and deviations from the ideal 180 degrees flip angle. For large negative k_z encoding steps, this dephasing gradient can be on the same scale

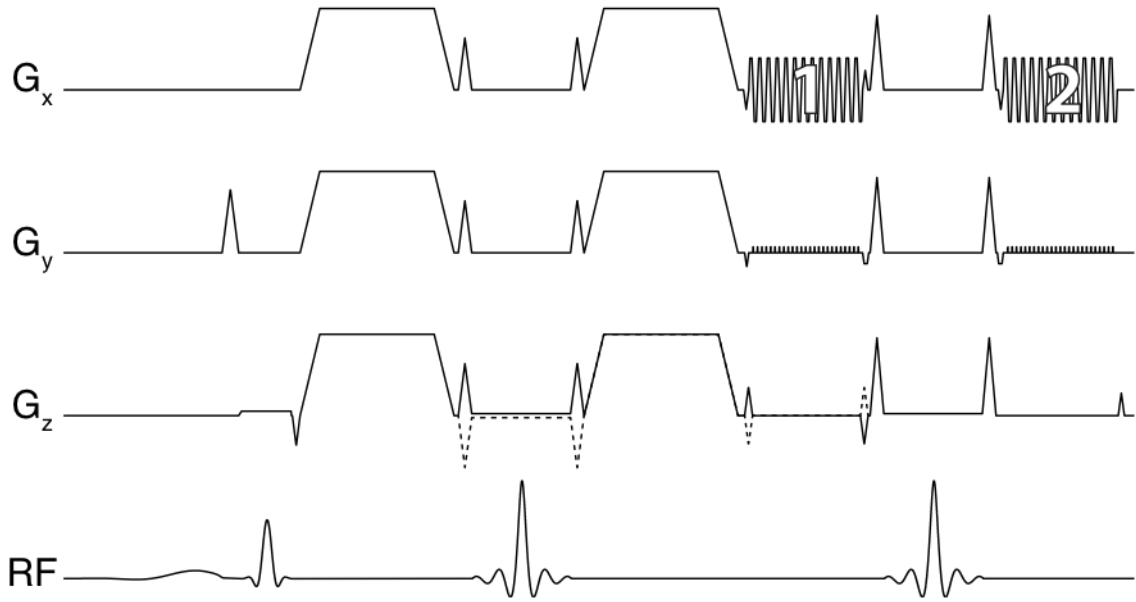


Figure 15. Pulse sequence diagram for DW 3D-MS EPI

as the positive crusher gradient following the refocusing pulse. This makes the two gradient moments partially cancel out, making the FID of the refocusing pulse contribute to the signal in the EPI readout, leading to image artifacts. To counteract this effect, the sequence was modified so that the polarity (but not the size) of both crusher gradients followed the polarity of the k_z dephasing gradient.

3.2.2.3 Slab combination

With knowledge on how to create slabs that are well defined remains the issue of creating one full volume out of multiple sub-volumes. This has been a general problem for all multi-slab acquisitions for a long time. First, there is the issue of potential slab aliasing in the z -direction due to long tails of the excited slab. Therefore, the slab typically needs to be oversampled with some extra k_z steps to encode sufficient space outside the full-width-half-maximum (FWHM) of the slab. The sharpness of the slice profile determines the amount of oversampling necessary. Even for a very sharp slice profile, an extra k_z sampling step on each side is a theoretical minimum. In practice, a few more k_z steps are necessary to avoid aliasing and to give room for imperfections in the slab profile and also handle minor movements. In this thesis adjacent slabs overlapped by ~40% of the full slab z -FOV, if not specified otherwise.

To combine slabs to a single volume, the simplest approach may be to average the slab data in the spatially overlapping regions. This tends to be suboptimal as it is very difficult to acquire slabs with a certain slab profile and overlap that produces a flat signal intensity over the volume in the z -direction after straightforward

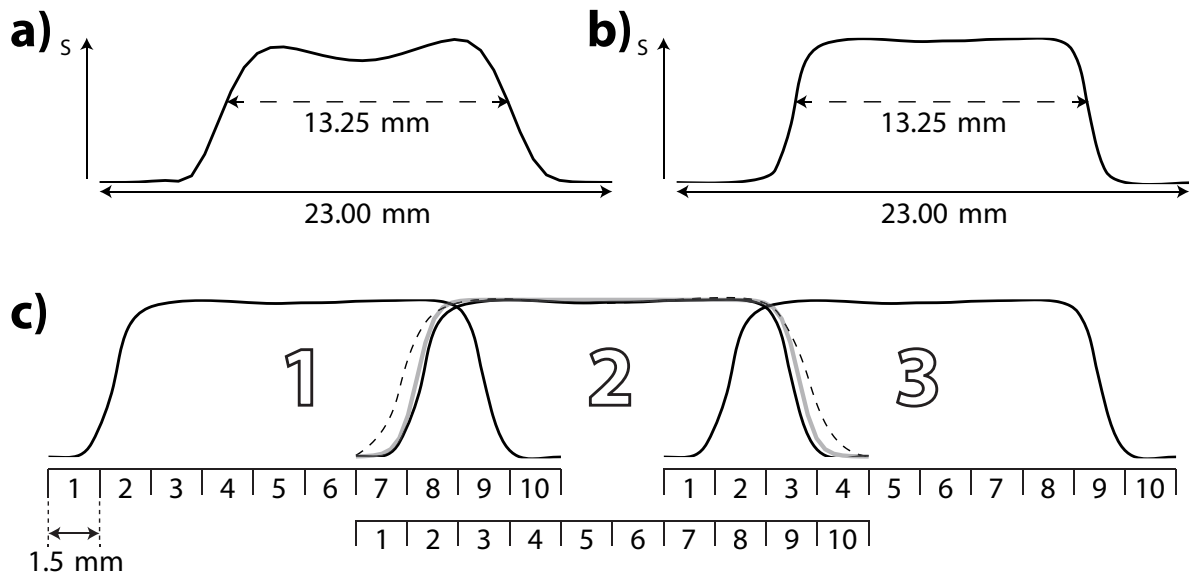


Figure 16. Slab profile comparison of a) default vendor pulses, and b) our SLR optimized pulses. c) Slab-to-slab combination scheme.

averaging. The slab profile is rarely perfectly symmetrical and even if it were, two partially overlapping slab profiles have to have a perfectly linear transition zone to make the sum of the slab weighting constant. The preferred method is therefore to compensate for the slab profile via sum-of-squares weighted combination, as demonstrated by Skare et al. in 2013 (91), where the slice profile was calculated beforehand, and was shown to be a fairly successful approach in the absence of T_1 -saturation effects.

Whilst cross-talk between adjacent 2D slices (only) leads to a saturation of the overall signal, the cross-talk effects are more apparent in multi-slab imaging. With the necessary overlapping of slabs, a spatially uneven T_1 -saturation over the slab is another problem, as the outermost parts of each slab are excited every $TR/2$ while the central part is excited every TR . Depending on which TR that has been prescribed, the different amount of T_1 -weighting in these regions may effect the signal. One has also to consider whether this uneven T_1 -saturation will affect any subsequent diffusion post-processing. Since the differences in T_1 is quite small between WM and GM (compared to CSF), an average T_1 -weighting of the brain parenchyma may be used to partially undo the T_1 -dependent slab profile in the reconstruction.

3.2.2.4 Phase navigation

Multi-slab EPI imaging requires data acquisition to extend over multiple excitations or TRs per volume, where each excitation corresponds to a certain k_z -encoding step. Therefore, with diffusion gradients present giving rise a new random phase before each EPI readout, phase navigation is necessary to control

and correct for this diffusion phase across the TRs. Similar to the procedure for DW RS-EPI (22) and DW-vGRASE (42) another EPI readout after the imaging echo is used to capture this semi-random spatially varying phase.

What makes a phase navigator in diffusion-weighted multi-slab imaging a bit different from the 2D counterparts is the thickness of the slab. The slowly varying phase that is corrected for in 2D acquisitions stems from 3D brain motion. Since the phase navigator echo is not k_z encoded, its phase information is still only 2D despite the now much larger extent in the z -direction. For thick slabs, the approximation of the diffusion phase (which is 3D in nature) to be constant across the slab may no longer hold well. For this reason, the slabs in the presence of diffusion gradients are preferably not to be made too thick to avoid signal cancellations.

3.2.2.5 Phase correction

Poncelet et al. showed in 1992 (92) that the diffusion phase is slowly varying over the head and that successful image reconstruction can be achieved by only removing the low spatial frequency component of the object's phase. The assumption we make with a 2D navigator is that this phase variation is negligible over a 15-30 mm slab, and that it is sufficient to perform only an in-plane phase correction of each k_z -encoded readout.

A phase difference map, $\Delta\phi_j(x,y)$, for the j^{th} k_z encoding step of the T_2 -w data was calculated by taking the difference between the phase information of the j^{th} navigator echo in the slab and a reference navigator. As reference navigator, any one of the navigators belonging to the slab could be used. To only include phase changes of low spatial frequency (corresponding to brain motion) in the phase difference map, a triangular 2D low-pass filter was applied, $T(k_x, k_y)$, with a width of 25% of the full k -space extent. The low-pass filtered navigator phase was calculated as

$$\phi_{\text{nav},j}(x, y) = \angle \left\{ \mathcal{F}_{2D}^{-1} \left(k_{\text{nav},j}(k_x, k_y, j) \odot T(k_x, k_y) \right) \right\}; \quad j = 1 \dots N_{k_z} \quad [19]$$

where ' \odot ' denotes element-wise multiplication. The phase difference map given as

$$\Delta\phi_j(x, y) = \phi_{\text{nav},j}(x, y) - \phi_{\text{nav,ref}}(x, y) \quad [20]$$

Correcting the Fourier encoded first EPI readout (both $b = 0$ s/mm² and $b = 1000$ s/mm²), is done by exponential multiplication

$$I_{\text{corr}}(x, y, j) = I(x, y, j)e^{i\Delta\varphi_j(x, y)}; \quad j = 1 \dots N_{k_z} \quad [21]$$

With this phase component removed from the hybrid-space slab data $I_{\text{corr}}(x, y, k_z)$, a Fourier transform in the slab direction yields the final slab volume $I_{\text{corr}}(x, y, z)$. As this process is conducted independently for each slab, there is still no guaranteed inter-slab phase consistency. By applying the phase correction on each slice within the slab once more, the slabs can now be combined. An alternative approach to this second phase correction step would be to just use the magnitude of the slab data for slab combination, but this leads to a more pronounced Rician noise distribution and an elevated noise floor (93).

3.2.2.6 Motion correction and slab combination

To combine the 3D encoded slabs into a full volume, at least the outermost slice on each side of the slab has to be discarded due to aliasing signal coming from the tails of the slab. Instead of discarding an integer number of encoded slices in the slab, a fairly sharp 1D Fermi filter was applied to the data in the slab encoding direction prior to slab combination. For the slab combination, the slabs were weighted by the 1D Fermi filter and the measured slab profile.

To correct for the possible in-plane (2D) motion occurring during the acquisition of one diffusion-weighted volume two different types of motion correction were applied, intra-slab motion correction and inter-slab motion correction. For the intra-slab motion correction, motion within a slab between each k_z -encoding step is corrected for using the magnitude of the navigator data. For each slab, one navigator (second readout) was chosen as reference based on image entropy. The other navigators in the slab were then realigned to the reference and the detected motion parameters applied to the first readout of each k_z encode. Motion correction directly between the first readouts is not possible due to the slab phase encoding.

Once all slabs have been internally corrected, the slabs may still not be consistent with each other. To perform an in-plane alignment of the slab volumes, data in the shared anatomical regions in the overlapping zones between the slabs was used for the registration. First, the two most central slabs were aligned to each other, after which the algorithm proceeded outwards towards the next slab, and so forth until all slabs were aligned to each other in the x-y plane.

3.2.2.7 SNR

There are many ways to calculate and estimate the SNR for a given sequence, including experiments such as e.g. the NEMA standard protocol (NEMA MS 1-

2008, National Electrical Manufacturers Association, Arlington, VA) or through various types of theoretical modeling. Comparing the SNR for two (or more) sequences is yet something that has to be done with care, as there are most often many factors involved. A straightforward SNR comparison may neglect acquisition time, the number of slices per TR or may be performed with an unrealistic number of slices, which are important aspects from a clinical imaging perspective. For that reason it is often preferred to use an SNR-efficiency metric instead, which can be expressed as $\text{SNR}/\sqrt{T_{\text{scan}}}$. One way of determining the theoretical SNR was described by Edelstein et al. in 1986 (94):

$$\text{SNR} \propto \Delta x \Delta y \Delta z \sqrt{T_{\text{readout time}}} \quad [22]$$

where Δx , Δy , and Δz are spatial dimensions of a voxel and $T_{\text{readout time}}$ is the time the receiver is open for data sampling. For a SE sequence this would be the time it takes to sample on line in k-space, while it for an ssEPI sequence this would be the time it takes to acquire the entire k-space. This simple relation does however not include information about e.g. receive coils or relaxation times. For a 2D acquisition, Equation 22 has to be modified to include the number of phase encoding steps, N_y , and number of excitations, NEX,

$$\text{SNR}_{2\text{D}} \propto \Delta x \Delta y \Delta z \sqrt{N_y \text{NEX} T_{\text{readout time}}} \quad [23]$$

For a 3D acquisition, with two phase encoding directions (as in the case of a slab in a multi-slab sequence), N_y for the number of phase encoding steps in the y-direction and N_z for the number of phase encoding steps in the z-direction, a slight adaption gives

$$\text{SNR}_{3\text{D}} \propto \Delta x \Delta y \Delta z \sqrt{N_y N_z \text{NEX} T_{\text{readout time}}} \quad [24]$$

Assuming the same readout times for the 2D and a 3D sequence, the approximate SNR gain for 3D would be $\sqrt{N_{kz}}$, by dividing Equation 23 by Equation 24. To make this more general, individual properties of the 2D and 3D acquisition have to be considered. TE, TR, excitation flip angle (θ_{Ex}), and refocusing flip angle (θ_{Ref}) should therefore be included to make a more fair comparison. This thesis will exclusively discuss SNR efficiency in a diffusion-imaging context using spin-echo (SE) based EPI sequences for 2D and 3D. To include above said parameters, and

assuming SE characteristics, the signal can be described as, following the work of Perman et al. (95),

$$S = M_0 \sin \theta_{\text{Ex}} \sin^2 \left(\frac{\theta_{\text{Ref}}}{2} \right) \frac{1 + (\cos \theta_{\text{Ref}} - 1) e^{\frac{-(\text{TR} - \frac{\text{TE}}{2})}{T_1}} - \cos \theta_{\text{Ref}} e^{\frac{-\text{TR}}{T_1}} e^{\frac{-\text{TE}}{T_2}}}{1 - \cos \theta_{\text{Ex}} \cos \theta_{\text{Ref}} e^{\frac{-\text{TR}}{T_1}}} \quad [25]$$

By adding small phase encoding blips on the slice encoding direction board a 2D SE-EPI sequence can be modified into a 3D-MS SE-EPI sequence, as will be discussed more in detail later on in this thesis. This results in that $T_{\text{Readout time}}$ will be equal for the two sequences, as adding phase encoding in z does not change the readout duration, nor does it affect the TE or TR. If slice uniformity is ignored, the excitation flip angle can be set to 90° and refocusing flip angle to 180° . Combining Equation 23-25 then yields

$$\frac{\text{SNR}_{3\text{D}}}{\text{SNR}_{2\text{D}}} = \frac{\left(1 - 2e^{\frac{-(\text{TR}_{3\text{D}} - \frac{\text{TE}_{3\text{D}}}{2})}{T_1}} + e^{\frac{-\text{TR}_{3\text{D}}}{T_1}} \right) \sqrt{N_z}}{\left(1 - 2e^{\frac{-(\text{TR}_{2\text{D}} - \frac{\text{TE}_{2\text{D}}}{2})}{T_1}} + e^{\frac{-\text{TR}_{2\text{D}}}{T_1}} \right) \sqrt{\text{NEX}_{2\text{D}}}} \quad [26]$$

which shows the theoretical SNR relationship between 2D SE-EPI and 3D-MS SE-EPI. To understand how and when a 3D-MS approach outperforms a 2D approach in terms of SNR-efficiency, scan coverage in the slice direction (z) has to be included. In this thesis, the term ‘full brain coverage’ introduced and is here defined as 150 mm.

For a 3T MRI system accounting for modern hardware limits, a 2D SE-EPI and a 3D-MS SE-EPI scan can be simulated. The 2D SE-EPI was simulated with one EPI echo while the 3D-MS SE-EPI sequence was simulated with two EPI echoes, as this is necessary for diffusion phase correction. With a FOV of 220×220 mm and desired spatial resolution of $1.5 \times 1.5 \times 1.5$ mm³ the $\text{TE}_{\text{Full Fourier}}$ becomes about 80 ms using an acceleration factor of $R = 3$. This in turn yields a sequence time, T_{Seq} , (from the beginning of the ChemSat RF pulse to the end of sequence’s last spoiler gradient) of ~130 ms for 2D SE-EPI and 190 ms for 3D-MS SE-EPI. For 3D-MS SE-EPI, a standard slab thickness is 15 mm with an overlap of 40% between adjacent slabs. Acquiring one volume, with full brain coverage, would require 100 slices from the 2D SE-EPI and 17 slabs for the 3D-MS SE-EPI sequence. Hence, the shortest possible TR for the 2D sequence would be 13.0 s and 3.2 s for the 3D-MS sequence.

However, the 3D-MS sequence will require 10 repetitions to acquire all phase encoding steps in the slab direction, resulting in a total volume time of 32 s.

As ~30 s is the minimal possible time to acquire one diffusion-weighted volume with a 3D-MS technique, the fairest comparison of the two sequences is to use scan time normalization. That is to ask what would the SNR be for a 2D sequence if it were scanned for the same amount of time as the 3D-MS (NEX for 2D will be allowed as a floating number for the sake of argument). With a TR of 13.0 s and ~2.46 NEX the total acquisition time can be adjusted to 32 s. The relative SNR gain can now be calculated and will result in ~2.2 for white matter, ~1.92 for gray matter and ~1.0 for CSF, in favor for the 3D-MS sequence.

Although the exact numbers are only valid for this specific setup they serve as an example to show how it comes that the 3D-MS approach has an SNR advantage. The numbers can be generalized, as shown in Ref. (60) and the SNR advantage will still remain. It is not, as may initially be expected, the switch to a 3D acquisition that makes the most difference. It is rather that a large z-FOV can be acquired using 3DMS without the costly increase of TR, which 2D acquisitions require.

3.2.2.8 TR/T_1 saturation

At the center of the slab, the time allowed for T_1 -relaxation is the prescribed TR, whilst only TR/2 in the overlapping regions of the slab. The result of this difference in T_1 -weighting will manifest as a slab-banding artifact in reconstructed volumes if TR is not long enough. A TR longer than about $4 \times T_1$ is therefore necessary to mitigate these saturation artifacts. When imaging samples with one single T_1 , a signal compensating weighting can be applied in the reconstruction, but as soon as multiple T_1 exists, partial volume effects will make any sort of compensation weighting difficult. The slab-banding artifact has therefore been one of the main obstacles to overcome for multi-slab MRI especially in the short TR regime. For longer TR, the scan time increases, but can be compensated by slab undersampling techniques (96).

3.2.3 DW 3D-MS EPI – Sequence

3.2.3.1 Data acquisition and Experiments

Human and phantom scans were acquired using the standard protocol found in Table 2. The TR was set to 4600 ms to allow enough T_1 -relaxation to occur in white and gray matter, noting that a TR of 4600 ms yields an effective TR of 2300 in

Table 2: Scan parameters_{DW 3D-MS EPI}

FOV	220×220 mm ²
Resolution	1.5×1.5×1.5 mm ³
Matrix _{Slab}	144×144×10 (fexpe _x pe _{Slab})
Slab _{Thickness}	15.0 mm
Slab _{Spacing}	-6.0 mm
R _(GRAPPA)	3
NEX	3
N _{Slabs}	24
N _{Readouts}	2
TR	4600 ms
TE _{Image}	78 ms
TE _{Navigator}	128 ms
b	1000 s/mm ²
N _{T2w}	2
N _{DW}	15

the overlapping region between adjacent slabs with an interleaved acquisition order. For each TR a new slice phase encoding step was acquired. Parallel imaging was used in-plane to reduce geometric distortions, TE, and scan time. GRAPPA calibration data were obtained by shifting the starting k_y position by one Δk_y for the R first acquisitions of the T₂-weighted ($b = 0$ s/mm²) reference data. GRAPPA weight sets were calculated on a per-slab and k_z encoding step basis and applied to the subsequent diffusion-weighted data volumes and k_z -encodes. For one experiment, the slab thickness was varied from 15 to 30 mm to evaluate the validity of a 2D approximation of the diffusion phase for a range of slab thicknesses (Table 3). For another experiment, the resolution was increased to 1.3×1.3×1.3 mm³ as a proof of concept (Table 4) resulting in a 40 min scan time. A 2D DW-ssEPI was used as gold standard and a scan time normalized reference scan was created with identical scan time and resolution as the standard DW 3D-MS EPI protocol, except for a longer TR of 13,000 ms to account for the larger amount of slices (Table 5). For the SNR comparison, 27 and 81 T₂-w volumes were acquired using the DW 3D-MS EPI and the DW-ssEPI, respectively. SNR maps were calculated after smoothing the image data with a 4.5×4.5×4.5 mm³ Gaussian kernel.

Table 3: Scan parameters_{DW 3D-MS EPI}

Matrix _{Slab} ($f \times p \times p \times e_{\text{Slab}}$)	144×144×10	144×144×12	144×144×14	144×144×20
SlabThickness	15.0 mm	18.0 mm	21.0 mm	30.0 mm
SlabSpacing	-6.0 mm	-6.0 mm	-6.0 mm	-6.0 mm
N _{Slabs}	24	18	14	10

Table 4: Scan parameters_{DW 3D-MS EPI}

FOV	220×220 mm ²
Resolution	1.3×1.3×1.3 mm ³
Matrix _{Slab}	168×168×10 ($f \times p \times p \times e_{\text{Slab}}$)
SlabThickness	13.0 mm
SlabSpacing	-5.2 mm
R _(GRAPPA)	3
NEX	3
N _{Slabs}	17
N _{Readouts}	2
TR	4800 ms
TE _{image}	94 ms
TE _{Navigator}	155 ms
b	1000 s/mm ²
N _{T2w}	9
N _{DW}	45

Table 5: Scan parameters_{DW 3D-MS EPI}

	DW 3D-MS EPI	DW ssEPI
FOV	220×220 mm ²	220×220 mm ²
Resolution	1.5×1.5×1.5 mm ³	1.5×1.5×1.5 mm ³
Matrix _{Slab}	144×144×10 ($f \times p \times p \times e_{\text{Slab}}$)	144×144 ($f \times p \times e$)
SlabThickness	15.0 mm	1.5 mm
SlabSpacing	-6.0 mm	0 mm
R _(GRAPPA)	3	3
NEX	3	9
N _{Slabs}	24	144
N _{Readouts}	2	1
TR	4500 ms	13000 ms
TE _{image}	78 ms	78 ms
TE _{Navigator}	128 ms	N/A
b	1000 s/mm ²	1000 s/mm ²
N _{T2w}	27	81
N _{DW}	10	10

3.2.4 DW 3D-MS EPI – Efficiency and Artifacts

This work is an extension of the method presented in the previous section, now with a focus on SNR efficiency and slab profile effects.

3.2.4.1 Slice profile effects

To examine slab profiles for different RF pulses and TRs, a cylindrical water phantom (with a T_1 of ~ 1200 ms) was used to simulate a mixture of GM and WM. The combined use of the vendor's SpSp RF pulse (14.4 ms, TBW = 2) and refocusing RF pulse (SLR: 3.2 ms, TBW = 4) was compared against using 12 ms excitation and refocusing RF pulses with a TBW of 14 (90). The slab profiles were measured by moving the slice selection gradient for the respective RF pulses from the z to the x (freq. enc.) axis. For the depiction of the combined slice profile, both slice selection gradients were placed on the frequency-encoding axis, rendering the effective slab profile directly in the reconstructed images.

Table 6: Scan parameters_{DW 3D-MS EPI}

	2D Ex.SpSp + Ref.Vendor	2D Ex.SLR + Ref.SLR	3D-MS Ex.SLR + Ref.SLR
FOV	140×140 mm ²	140×140 mm ²	140×140 mm ²
Resolution	2.9×2.9×0.25 mm ³	2.9×2.9×0.25 mm ³	2.9×2.9×0.25 mm ³
Matrix _{Slab} (fexpe _x pe _y pe _z)	48×48×80	48×48×80	48×48×80
N _{Slabs}	6	6	6
Slab _z FOV	20.0 mm	20.0 mm	20.0 mm
Slab _{Thickness}	10.0 mm	10.0 mm	10.0 mm
Slab _{Spacing}	0 mm	0 mm	-2 mm
TR	1000-5000 ms	1000-5000 ms	1000-5000 ms
TE	65 ms	65 ms	65 ms

3.2.4.2 T1 saturation effects

To investigate how the slab profile is affected by the choice of TR, the previous approach does not work as it can only image a single slab at a time. Instead a modified version of the 3D-MS EPI was used with an increased number of encoding steps in the z-FOV, and the FWHM of the nominal combined slab profile was set to 50% of the z-FOV. Thereby, also the tails of the slab profile could be well resolved. In one experiment, mimicking 2D zero gap imaging, the slabs were spaced out by the FWHM of the combined slab profile. In a second experiment the slabs were spaced out by 80% of the FWHM, corresponding to a realistic overlap for 3D-MS EPI. The first experiment was acquired with default and sharper RF pulses, while the second experiment simulating the multi-slab scenario used only the sharper RF pulses. Relevant sequence parameters can be found in Table 6.

3.2.4.3 SNR simulations

Based on the signal equations presented in Eqs. 22-26, theoretical SNR calculations could be performed for both 2D DW-ssEPI and DW 3D-MS EPI scans with a fixed voxel size of $1.5 \times 1.5 \times 1.5 \text{ mm}^3$. The sequence timing was based on the standard protocol in Table 1. The TR was set to the minimum time possible to fit the slices for the requested scan coverage (z-FOV). With the 3D-MS EPI being more time consuming (per volume), scan-time normalization was performed by adding averages (NEX) to the 2D sequence. Although unrealistic in reality, floating point NEX was allowed to correctly match all possible scan combinations. With the scan timing and acquisition time identical the signal was approximate as that of a spin-echo following the work Perman et.al in 1984 (95). Calculations were done for T_1 values representing WM, GM and CSF using tabulated values in the literature (97,98).

3.2.4.4 Compensating the TR/T_1 -Related slab-profile artifacts

To reduce the banding artifacts that arise at low TRs two different approaches were proposed for the image reconstruction. In the first approach, an attempt was made to undo the signal profile across the slab before slab-combination by finding the combined effective slab profile due to both the inherent RF pulse profile and the additional TR/T_1 -related modulation in the overlapping regions. The second approach attempted to remove the slab banding in the final slab-combined 3D volume via band-pass filtration.

Considering that the two dominating tissue types in the brain, gray and white matter, have approximately the same T_1 (at least when compared to CSF), the assumption is that there is a common single 1D effective slab profile for all slabs for a given TR. This 1D slab profile was estimated by first masking out the brain in all slabs for all diffusion encoding directions. An average was then taken over all slabs, volumes, and over both in-plane axes to create a 1D slab profile along z. The profile was used to weigh each slab prior to slab combination. As this weighting filter is applied to both the T2-w and the DWI data it does not affect the diffusion calculations of ADC or FA.

The second approach acknowledges that the uneven T_1 -weighting manifests itself as a periodic signal fluctuation in the z-direction in the final reconstructed 3D volumes. To quantify the amount of banding, all 3D diffusion volumes were first averaged to a single volume and then averaged over both in-plane axes. The resulting 1D signal (now over the entire z-FOV) was Fourier transformed and band-passed filtered matching the spatial frequencies corresponding to the slab separation and width. An inverse Fourier transform was applied and the resulting

banding-signal was used to remove the periodic fluctuation for in the 3D data (T₂-weighted and diffusion-weighted). Similar to the pre-slab approach does this filter also act as a point operator and will not affect the parametric diffusion maps.

3.3 MOTION CORRECTION

3.3.1 2D Sagittal FatNav to address nodding motion

In this initial study we explored the concept of using the subcutaneous fat surrounding the skull for motion navigation, more precisely nodding motion. It did not include a diffusion-weighted host pulse sequence and shall be seen as a proof of concept of the FatNav method to outline the characteristics and limitations of fat navigators for brain applications. Unlike previous brain navigators that utilize the water content, the signal from fat is depicted as spatially sparse and opens up good opportunities for high parallel imaging acceleration. With the study only focusing on nodding motion a single sagittal slab was acquired through the anatomical mid-line of the brain. The navigator module was implemented as a stand-alone pulse sequence using an SpSp excitation and an EPI readout.

3.3.1.1 Excitation of a mid-sagittal fat slice for motion navigation

The excitation slice for the FatNav sequence module was positioned at the center of the head with a FOV size of $300 \times 300 \text{ mm}^2$, a slice thickness of 30 mm, and an in-plane matrix size of 48×48 yielding a voxel size of $6.25 \times 6.25 \times 30 \text{ mm}^3$. The frequency offset between fat and water was manually adjusted (a $\sim 380 \text{ Hz}$ offset was used instead of the theoretical value of $\sim 440 \text{ Hz}$). Although the SpSp RF excitation pulse centered on the fat peak should only excite the fat signal, some additional ‘leaking’ is unavoidable. In order not to cause saturation artifacts, in both water (not to be excited) and fat, a low flip angle of 10° was used.

For reduced distortion artifacts, that in turn will influence motion parameters, parallel imaging (GRAPPA) was used. High parallel imaging factors were attempted, due to the sparsity of the signal, ranging from $R = 1$ -8 using the 8-ch RF coil. An additional benefit of using a high acceleration factor, assuming that the SNR and reconstruction hold together, is that the navigator readout duration is minimized, meaning less scan time overhead when combined with a host pulse sequence.

3.3.1.2 GRAPPA weights estimation on FatNav data

In order to optimally reconstruct the undersampled FatNav data (as it will rely on high acceleration factors), optimal calibration data for GRAPPA weight estimation is crucial. The effects of both the signal content (water or fat) and the level of

distortions in the calibration data were investigated. Regarding the signal content, the question was whether a more SNR rich water based calibration scan should be used over a content matched fat based calibration data. To test this two scans were acquired on a healthy volunteer using water-selective and fat-selective RF pulses, respectively. To rule out distortion effects and Nyquist ghosting, the EPI data were acquired as a GRE sequence with one line per TR (i.e. $N_y = N_{shots}$). Two weight-sets were calculated from each calibration data, one at $R = 4$ and one at $R = 8$. To test the validity of the weight sets, cross-reconstructions were also performed, i.e. where the fat data was reconstructed using weights calculated from water data, and vice versa. For all experiments, separate data set were used for calibration and the accelerated data to avoid self-calibration benefits, which may unfairly reduce noise.

Next, the need for distortion matched calibration data was investigated, where the question was if the calibration data should have the same distortion level as the reconstructed data or if the calibration data should be free from distortions. This experiment was performed by reconstructing $R = 1-8$ data with distortion-free and distortion-matched calibrations. During the acquisition of the calibration data sets, the subject was instructed to lie still. Before the subsequent accelerated scans, the subject was instructed to tilt the head backwards somewhat to better mimic a real life situation.

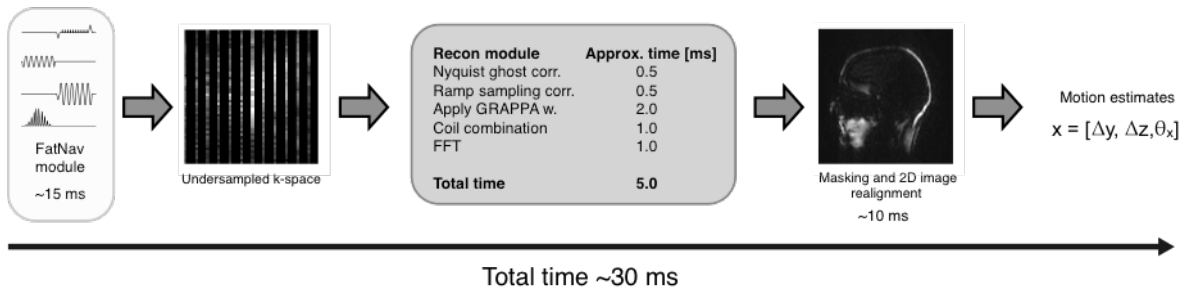


Figure 17. FatNav recon procedure

3.3.1.3 Head pose and the robustness of the GRAPPA weights

To more comprehensively investigate the effect of head motion and parallel imaging for FatNav, a third experiment was carried out. This time the subject was instructed to move its head in a nodding motion from 'chin down' to 'chin up' in five evenly spaced steps. The approximate maximum tilt was between ± 7 degrees. For each position two FatNav data sets were acquired, one for calibration and one for reconstruction. Cross-reconstructions were then performed between all data sets, i.e. -7° GRAPPA weights were used to reconstruct -7° to $+7^\circ$ data sets, -3.5° GRAPPA weights were used to reconstruct -7° to $+7^\circ$ data sets, and so on. A

maximal tilt of $\sim 15^\circ$ (from initial position) is expected to be a reasonable approximation of a large head movement found among clinical patients.

3.3.1.4 Distortions in the FatNav data and the motion accuracy

With the EPI distortions being inversely proportional to the acceleration factor R , it is important to investigate the accuracy of the FatNav motion-estimates for different values of R . For this experiment, three healthy volunteers were scanned. Each volunteer was scanned with a set of five sequences repeated for 30 different head poses (nodding motion) directly after each other. The first of the five sequences in each set was a distortion free high-resolution SPGR sequence (water signal). The second was a FatNav sequence with $R = 2$ and the phase encoding direction anterior to posterior, and the third scan was identical except for a reversed phase encoding polarity making the distortions occur in the opposite direction. The remaining two scans in each set were similar to scans #2 and #3, but using $R = 8$ instead of $R = 2$. As changing the phase encoding direction also changes the distortion direction, the hypothesis was that a symmetric bias could be observed for $R = 2$ around the gold standard SPGR scan, and less so for $R = 8$.

Motion correction of the FatNav data was performed using a simple SoS metric in two passes, first with a $15 \times 15 \text{ mm}^2$ Gaussian smoothing to robustly capture gross motion followed by a $3 \times 3 \text{ mm}^2$ smoothing kernel for fine adjustments. With the FatNav data acquired in the sagittal plane, the non-rigid motion of the neck and jaw does bias the motion parameters. Therefore a mask was applied that excluded the most inferior 30% of the FOV. No masking was performed in the anterior-posterior direction.

3.3.1.5 Matrix size

The larger the matrix, the longer the FatNav module will become. To keep the navigator time short and image distortion low it is important to know how much the resolution can be reduced before motion estimates are affected due to lack of resolution. To evaluate this, repeated scan sets were performed, where each scan set comprised four FatNav scans (all with $R = 8$) with matrix sizes of 96×96 , 48×48 , 32×32 , and 96×96 (again). The last 96×96 was added to guarantee data consistency, i.e. no significant movements between the first and last scan in each scan set. Again, distortion free high-resolution SPGR data was used as gold standard. One healthy volunteer was scanned with all five sequences for 20 repetitions. Between each repetition, instructions were given to change head position in a nodding fashion.

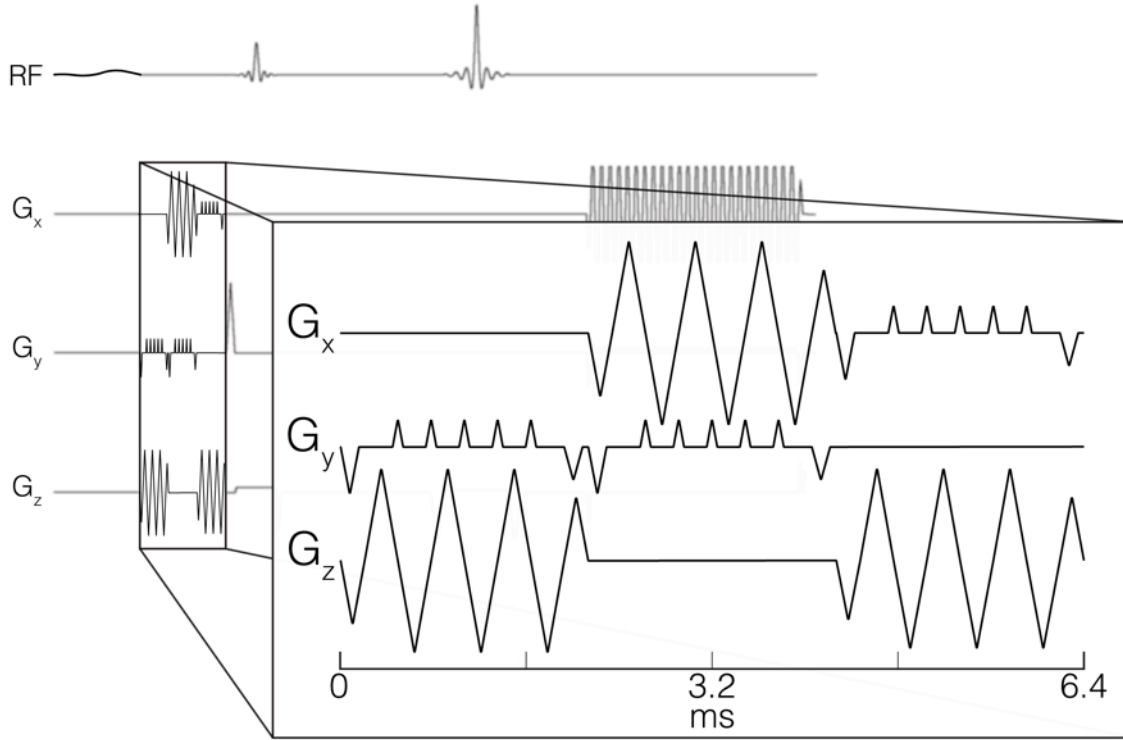


Figure 18. Collapsed FatNav readout block

3.3.2 Collapsed FatNav

While the FatNav method presented in the previous section only addresses motion in the sagittal plane, the collapsed FatNav (cFatNav) technique was designed to ultimately deal with full 3D rigid body motion. In this case, the single EPI readout previously used was replaced by three orthogonal EPI readouts, one in the sagittal plane, one in the axial plane, and one in the coronal plane. Also the FatNav RF pulse was modified from the slice selective SpSp RF pulse to a non slice-selective, but spectrally selective, chemical saturation RF pulse. The non-spatially selective RF pulse and the three 2D readouts results in projection (collapsed) images of the fat magnetization, hence the name.

In contrast to the 2D sagittal FatNav acquisition, which was implemented as a stand-alone pulse sequence, the collapsed FatNav (cFatNav) sequence module was implemented as a plugin to the 3DMS DW-EPI sequence. Programming wise, the cFatNav module was embedded in the chemical saturation pre-pulse source code module, the latter that is compatible with most pulse sequences provided by the vendor (GE).

3.3.2.1 Sequence

The default specifications for the cFatNav sequence block can be found in Table 7. GRAPPA calibration for the cFatNav data was obtained in the beginning of the scan by changing the k_{pe} -dephasing gradient for the R first acquisitions. This

calibration data was also used to determine the gradient delays for Nyquist ghost correction. For the subsequently acquired cFatNav data, the reconstruction time was ~25 ms per projection, including ghost correction, GRAPPA unaliasing and image realignment.

Table 7: Scan parameters_{ScFatNav}

FOV	320×320 mm ²
Resolution	6.6×6.6×∞ mm ³
Matrix _{Slab}	48×48 (fexpe)
R _(GRAPPA)	8
N _{Readouts}	3
TE _{Sagittal}	1.1 ms
TE _{Axial}	3.2 ms
TE _{Coronal}	5.3 ms
T _{Seq}	6.4 ms

3.3.2.2 Parallel imaging and resolution

To investigate the practical resolution of the cFatNav data, four scans were acquired on a healthy volunteer at 3T, using two parallel imaging acceleration factors ($R = 4$ and $R = 8$) and two different resolutions $6.7 \times 6.7 \text{ mm}^2$ and $10 \times 10 \text{ mm}^2$. The volunteer was instructed to lie as still as possible during all scans. Image reconstruction was done retrospectively using the same configuration as for the real-time reconstruction.

3.3.2.3 Saturation effects

Squeezing in a cFatNav readout block between the ChemSat RF pulse and the excitation pulse of the host sequence could possibly lead to unwanted fat signal in the host sequence due to unwanted M_z recovery of fat (due to its short T_1 relaxation time). This potential effect was investigated by acquiring four scans on a healthy volunteer (on a 1.5T system) where the delay between the saturation pulse and the excitation pulse was varied. As gold standard in terms of fat saturation performance, a fifth scan was acquired using an SpSp RF excitation (known for minimal fat signal residues). The host sequence was set up as a 2D spin-echo EPI with sequence timing similar to that of a clinical DW ssEPI sequence. The delays investigated were 0 ms, 6.4 ms, 15 ms, and 25 ms respectively, where 6.4 ms correspond to time needed for the suggested cFatNav configuration.

3.3.2.4 Stability

To investigate the stability of the cFatNav data, two stress tests were acquired. The first was designed to visualize system drifts and the second test evaluated the effects of long-term eddy currents from the diffusion encoding gradients on the cFatNav data. A total of 2400 cFatNav navigators were acquired with 66 ms separation in time. For the eddy current tests, a Stejskal-Tanner diffusion preparation was added with $b = 1000 \text{ s/mm}^2$. 60 noncollinear diffusion encoding directions were acquired in addition to 10 $b = 0 \text{ s/mm}^2$ acquisitions. 6532 cFatNav navigators were acquired with 130 ms separation. Data reconstruction was performed off-line in MATLAB.

3.3.2.5 In-vivo: Motion parameters and DW 3D-MS EPI

For accuracy tests of the motion estimates derived from the cFatNav navigator, a Spin-Echo EPI host sequence equipped with the cFatNav module was run twice, with nodding and left-right head motion, respectively. Diffusion gradients were not applied to rule out eddy-current effects in the cFatNav data. A spin-echo EPI sequence was prescribed to cover a $320 \times 320 \times 320$ mm³ volume for 12 consecutive volumes. Real-time motion correction updates were ignored and all data were reconstructed retrospectively.

In another experiment, cFatNav was used with the DW 3D-MS EPI sequence at 1.5T. This sequence was run four times on a volunteer, with and without step-wise nodding motion and with and without the cFatNav motion information applied in real-time to the host pulse sequence. For all scans, in-plane motion correction of the DW 3D-MS EPI data was performed according to previous work, for increased robustness to motion.

4 RESULTS

4.1 DW VGRASE

Reconstructed DW vGRASE data can be seen in Figure 19. The uncorrected iso-DWI (geometric complex average), Fig. 19b, shows severe blurring due to phase inconsistencies between the blinks. With the proposed phase correction applied, Fig. 19c,d, the data consistency is significantly improved. The high-pass filtering effect, due to T2 decay between each blind, can be seen if comparing Fig. 19c with Fig. 19d (where the latter has a T2 correcting scaling filter applied).

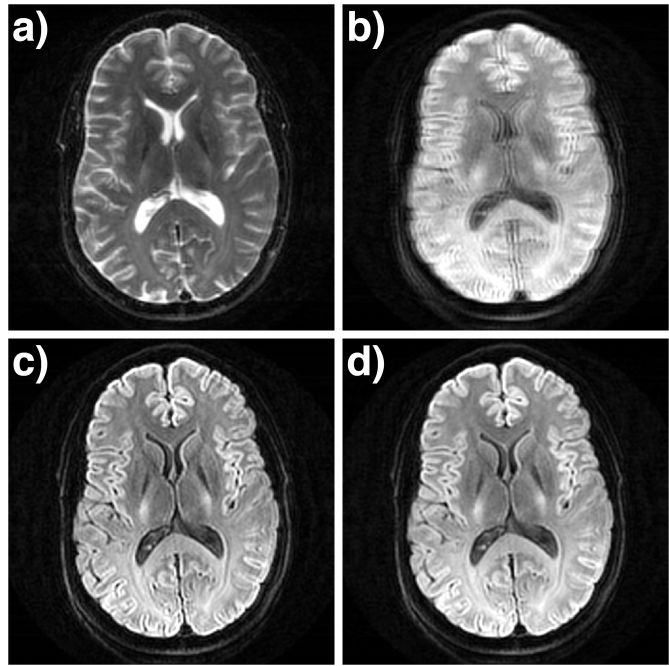


Figure 19. Reconstructed DW vGRASE data where a) is the b0 data, b) isoDWI without phase correction, c) isoDWI with phase correction, and d) isoDWI with phase correction and blind scaling.

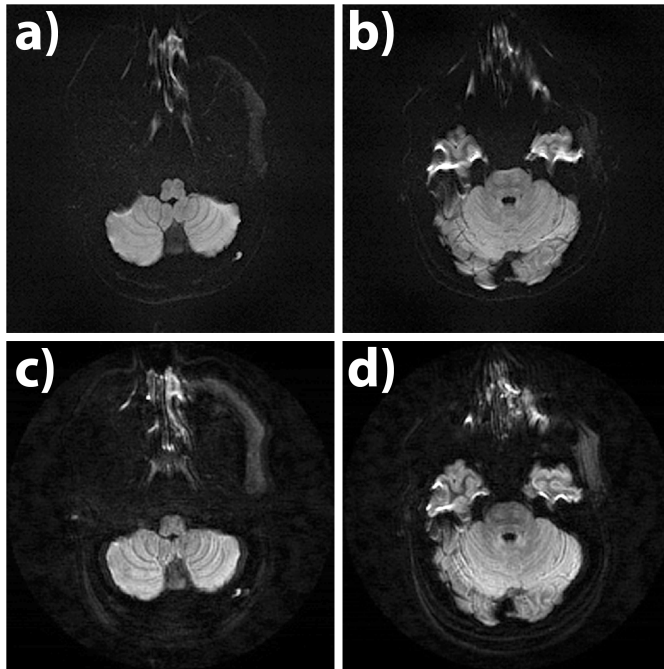


Figure 20. Comparison between DW ssEPI a,b) and DW vGRASE c,d) at two slice locations, showing reduced distortion levels at both locations.

In Figure 20 a comparison between DW ssEPI, Fig. 20a,b, and DW vGRASE, Fig. 20c,d, is shown. The reduced distortion level of the proposed method can be appreciated at both slice locations, however with a slightly increased noise for the DW vGRASE method (due to the increased TE). Both scans were acquired with 15 diffusion-encoding directions and in-plane parallel imaging acceleration (GRAPPA, R = 3).

4.2 DW 3D-MS EPI – PAPER I

Figure 21 shows DW 3D-MS EPI data, at $1.5 \times 1.5 \times 1.5$ mm³ resolution, without the proposed intra-slab phase correction in a) and with the correction in b). In both cases the b0 data (top row) is seemingly unaffected (as expected). Without the proposed correction strong phase cancellation artifacts appear, most apparent in the reformatted (sagittal and coronal) views.

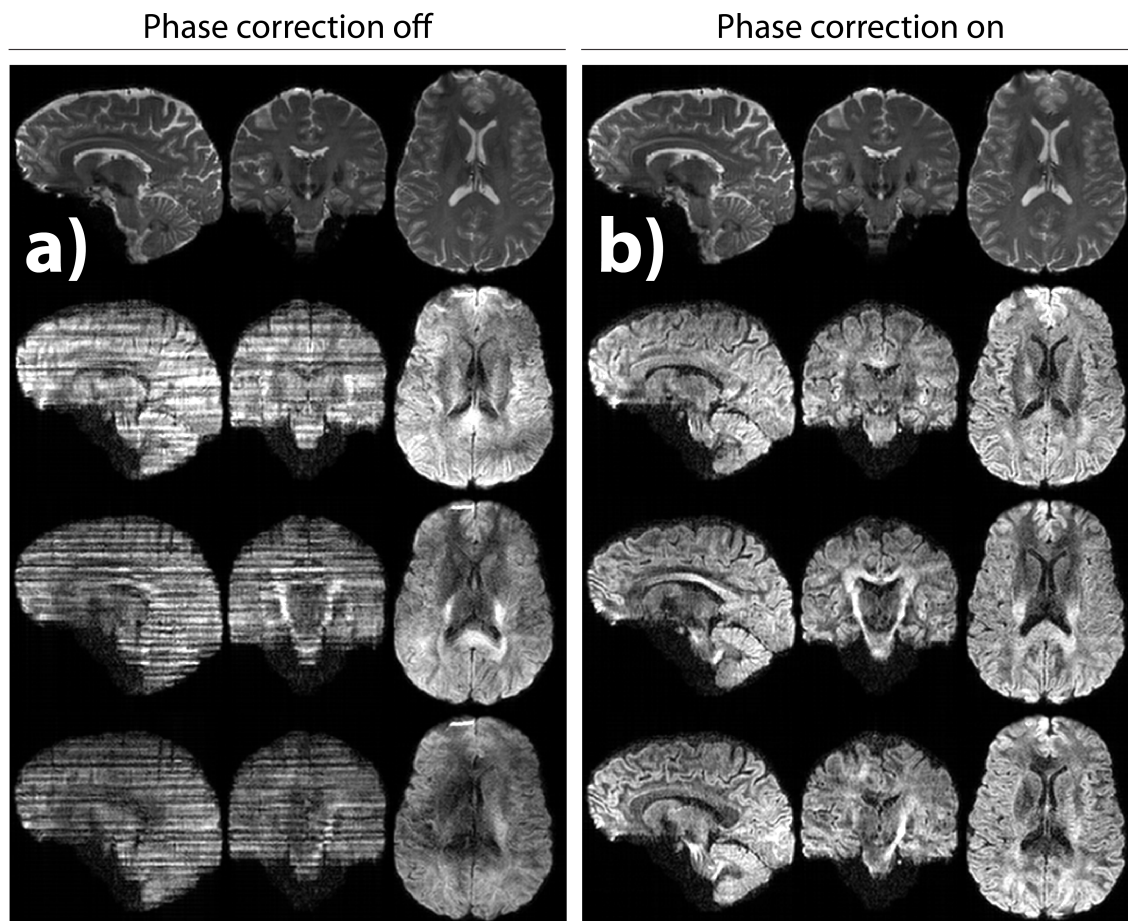


Figure 21. DW 3D-MS EPI data without the intra-slab phase correction in a) and with the correction in b).

The effect of increasing the slab thickness can be seen in Figure 22, where a) is with a 15 mm slab, b) with a 18 mm slab, c) with a 21 mm slab, and d) with a 30 mm slab. All data were acquired at $1.5 \times 1.5 \times 1.5$ mm³ resolution using the same slab-to-slab overlap. As the proposed intra-slab phase correction technique only addresses 2D in-plane phase variations the quality of the correction was expected to fall off with increasing slab thickness. This effect can be primarily seen in the brain stem of Fig. 22c,d. However, for all slab thicknesses, a fairly homogeneous signal is seen throughout the entire volumes.

SNR comparisons between scan time normalized 2D DW ssEPI data and DW 3D-MS EPI data is shown in Figure 23. Both scans were acquired at $1.5 \times 1.5 \times 1.5$ mm³

resolution using full brain coverage. The increased SNR of the DW 3D-MS EPI sequence is primarily due to the increased TR required for the 2D DW ssEPI to match the full brain coverage demand.

Figure 24 shows DW 3D-MS EPI data (single direction and isoDWI) in the presence of motion and the performance of the retrospective in-plane motion correction technique. In Fig. 24a,b the subject was instructed to lie as still as possible, in Fig. 24c,d, to nod the head, and Fig. 24e-h to shake the head from left to right. By comparing Fig. 24b with Fig. 24d and Fig. 24f clear improvement is seen for the left-right motion, but none for the nodding motion.

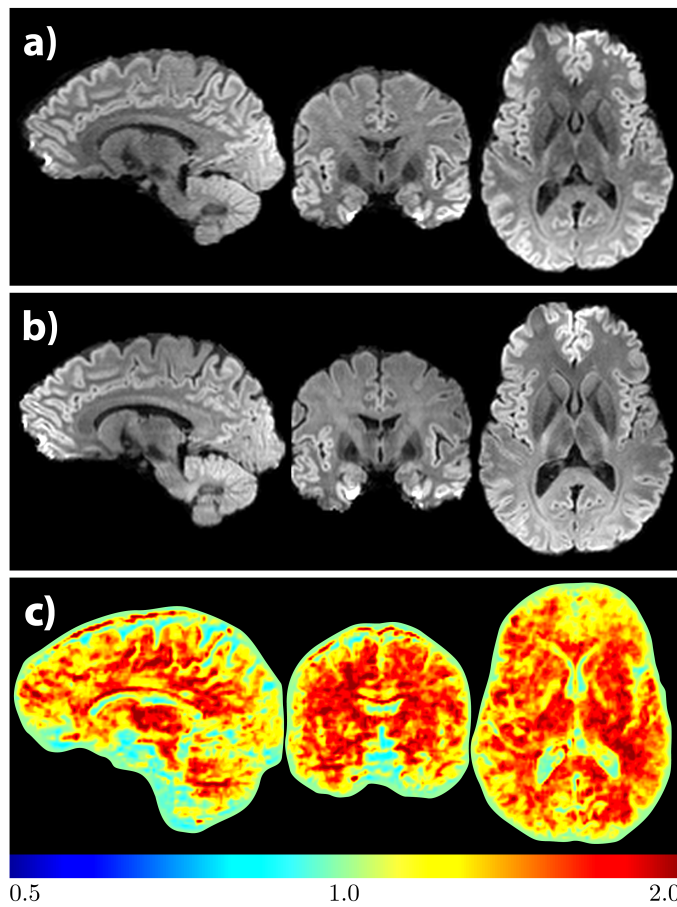


Figure 23. Comparisons of scan time normalized data with a) being 2D DW ssEPI, b) DW 3D-MS EPI, and c) SNR ratio (after smoothing).

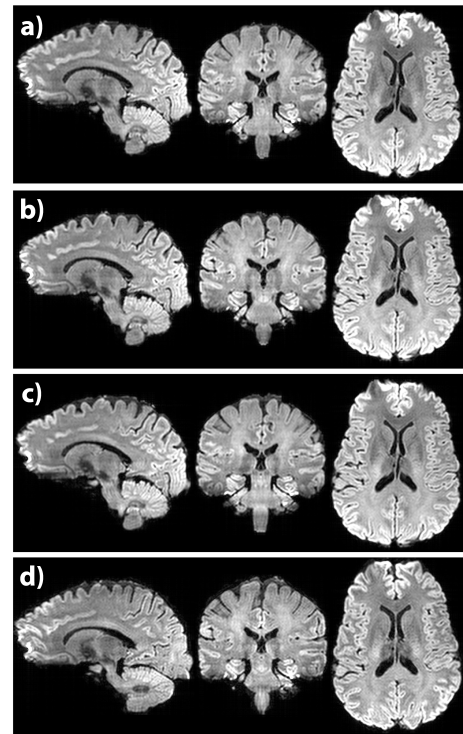


Figure 22. DW 3D-MS EPI isoDWIs with a) 15 mm, b) 18 mm, c) 21 mm, and d) 30 mm slice thickness

Figure 25 shows the isoDWI and color encoded FA map for a DW 3D-MS acquisition at $1.3 \times 1.3 \times 1.3$ mm³ resolution. As a consequence of the small voxel size the scan time was increased to ~40 min, and data should serve as a proof of concept.

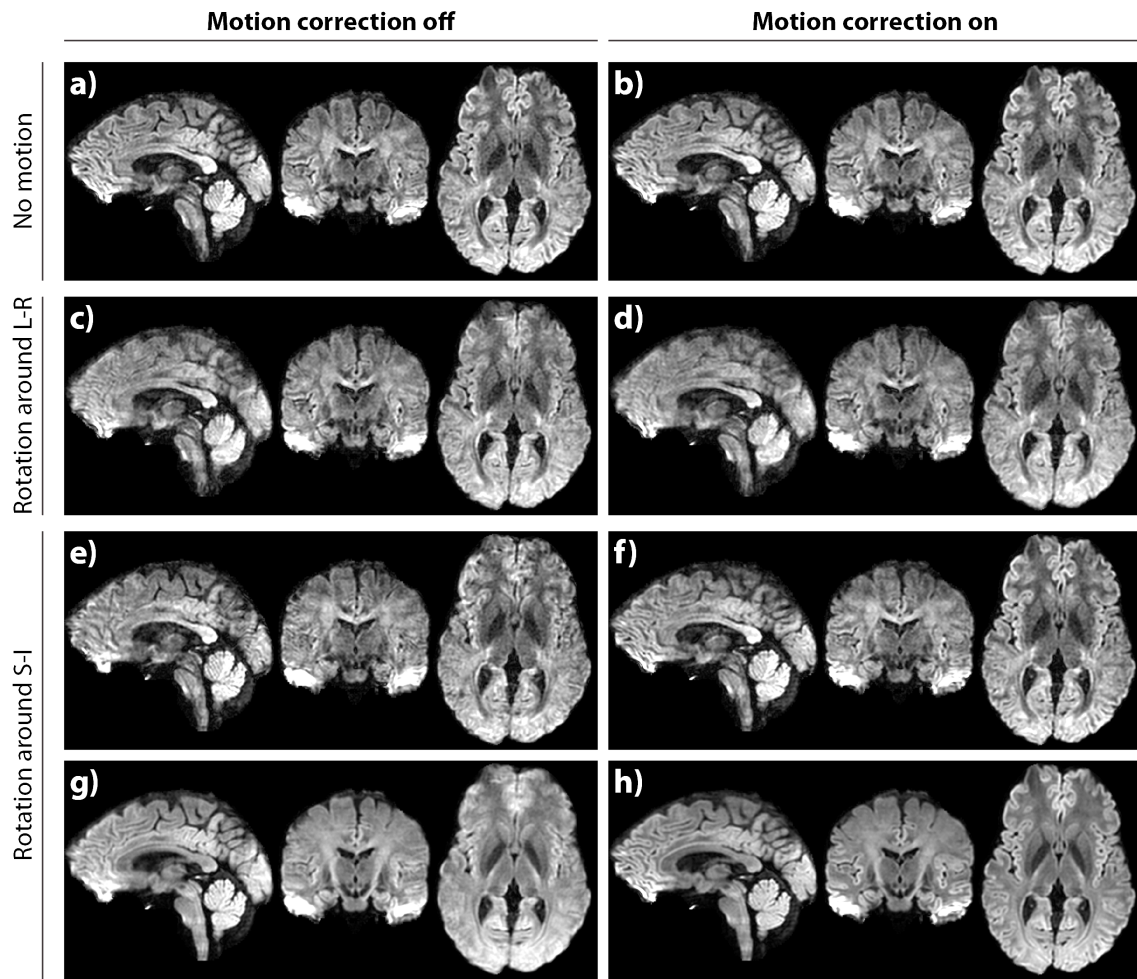
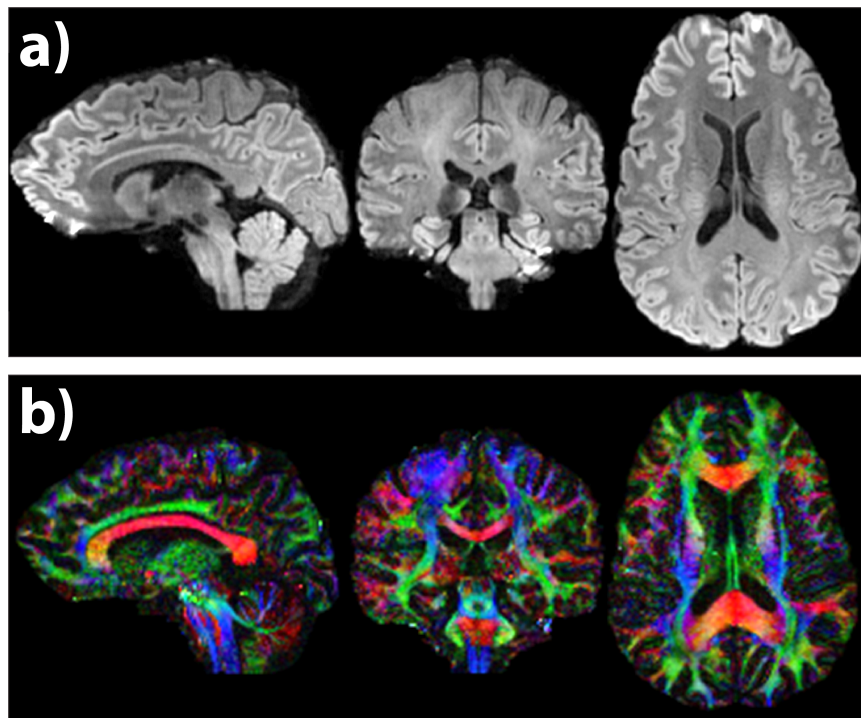


Figure 24. DW 3D-MS EPI with a,b) no motion, c,d) rotation around *L-R*, and e-h) rotation around *S-I*.

Figure 25. DW 3D-MS EPI data with $1.3 \times 1.3 \times 1.3$ mm³ resolution. a) isoDWI and b) color encoded FA map.



4.3 DW 3D-MS EPI – PAPER II

Figure 26 shows the results from the SNR simulations where a DW 3D-MS EPI is compared against a conventional 2D DW ssEPI used as gold standard, with identical scan parameters and coverage. For a-d) overlap effects were discarded and the values

correspond to the center of the slab. As seen is the DW 3D-MS EPI sequence most beneficial at large z-FOVs and with thick slabs (cf. Fig 26a-c). There is however a minimal TR that can be used before slab banding artifacts arise. This is illustrated in Fig. 26d where the TR as a function of slab thickness and z-FOV is depicted. The solid lines represent $2 \times T_1$ of GM and WM respectively. With a TR lower than $2 \times T_1$ of GM and WM banding artifacts will emerge.

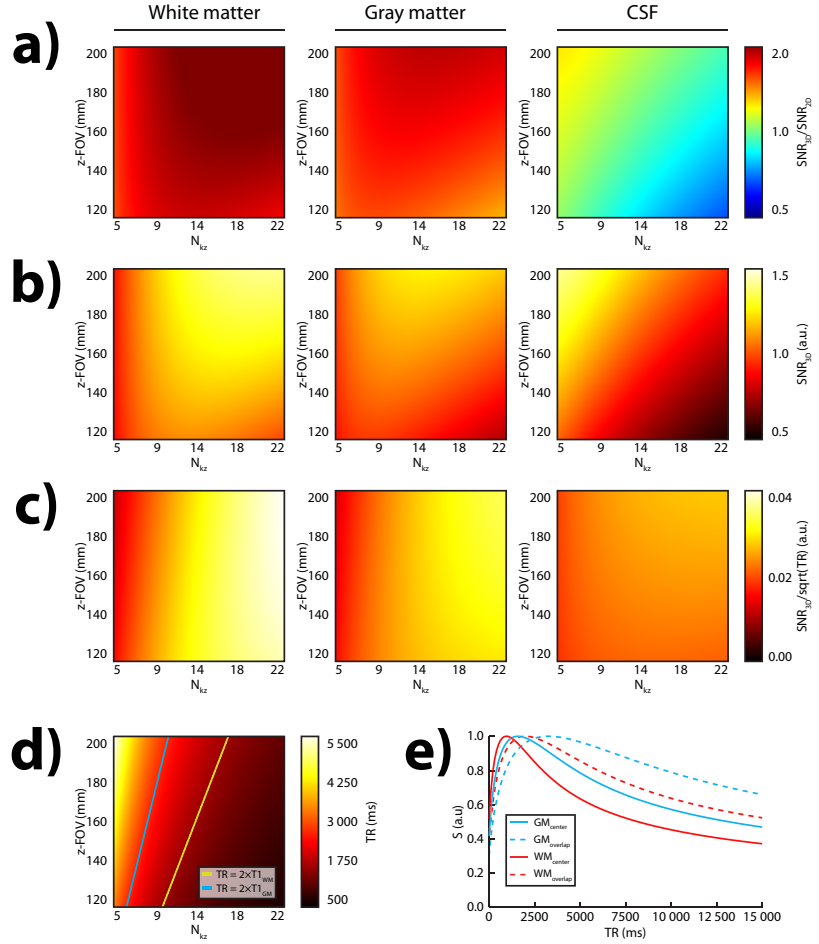


Figure 26. Simulations: a) SNR_{3D} versus SNR_{2D}, b) SNR_{3D}, c) SNR_{3D} efficiency, and d) corresponding TR. e) SNR efficiency for the slab center (solid lines), and overlapping zones (dashed lines) for gray and white matter.

In Fig. 26e signal (a.u.) versus TR is plotted as function of GM and WM for the slab center (solid lines) and the overlap zones (dashed lines). Optimal TR for GM (blue lines) is ~1700 ms, and ~1000 ms for WM at the center of the slabs. For the overlap zones these values increase slightly and becomes ~3400 ms for GM and ~2100 for WM.

The performance of the two slab banding reduction methods proposed is shown in Figure 27. In Fig. 27a was a TR of 4600 ms used while in Fig. 27b a TR of 2000 ms, in both cases was no banding reduction methods applied. In Fig. 27c, TR/T₁-

adjusted slab weighting was applied, while Fourier band-pass filtering was used in Fig. 27d. Fig. 27e shows the performance of the combined use of both methods.

4.4 FATNAV

The importance of image contrast in the GRAPPA calibration data is shown in Figure 28. For $R = 4$ GRAPPA weights derived from water and fat work reasonably well in unfolding data, with some low frequent signal changes for fat derived weights on water data, Fig. 28g. For high acceleration factors the choice becomes more critical, as seen by inspecting Fig. 28c,e,h,j. Water derived GRAPPA weights yield unacceptable results, Fig. 28e, and the need for content matched calibration becomes apparent.

In order to acquire data that is as geometrically correct as possible the

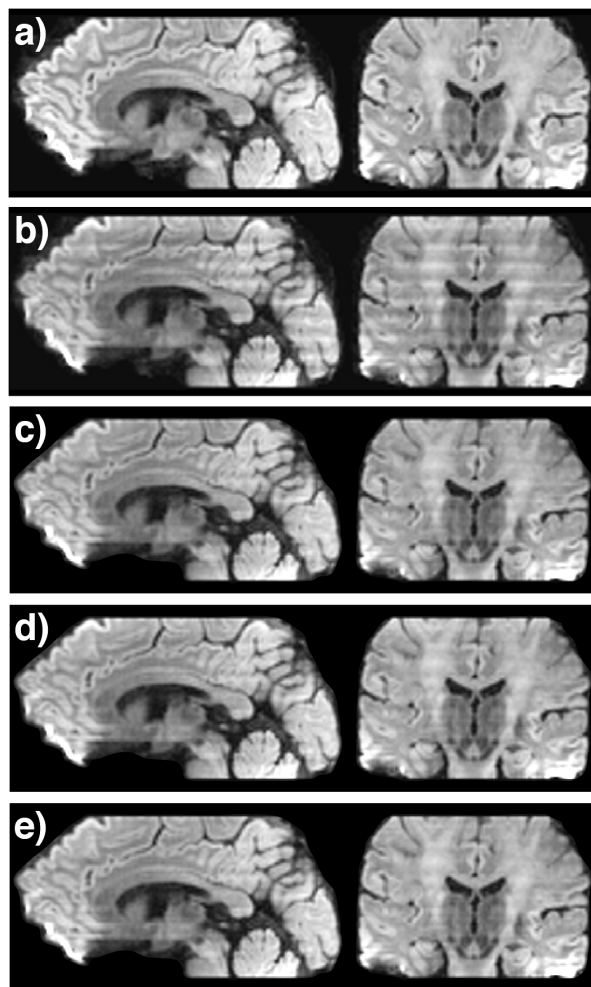


Figure 27. Banding artifact reduction: a) $TR = 4600$ ms (no correction), $TR = 2000$ ms with b) no correction, c) TR/T_1 -adjusted slab weighting, d) Fourier band-pass filtering, and e) combined use of both c) and d).

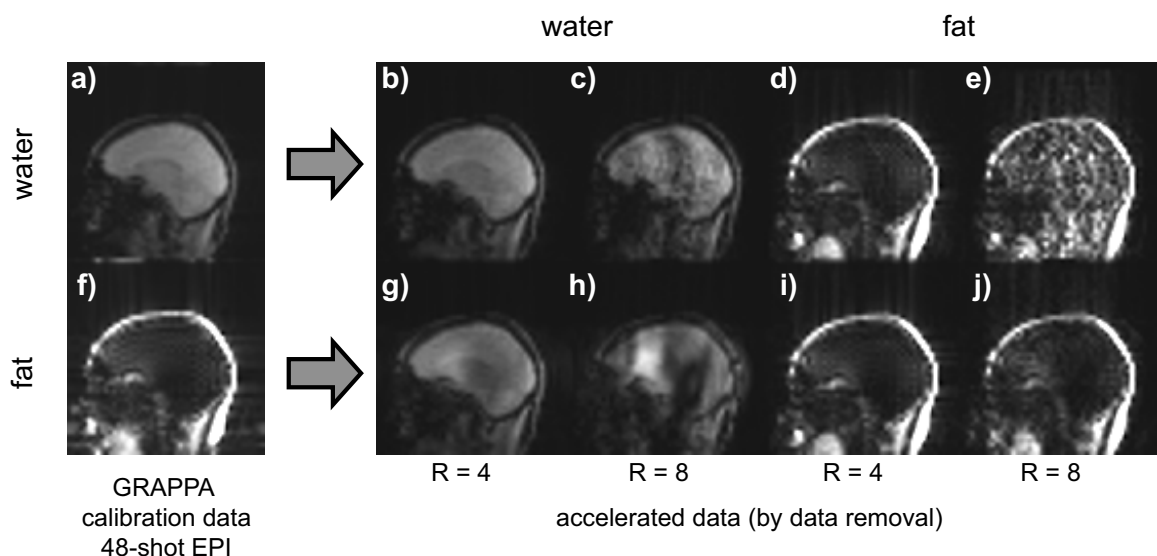


Figure 28. GRAPPA calibration data with water a) and fat f). Data reconstructed with GRAPPA weights estimated from water are shown in b-c) and from fat in g-j).

use of high acceleration factors is desired. Figure 29 shows FatNav data with acceleration levels ranging from $R = 1$ to $R = 8$. On the top row data with $etl = 1$ was used for GRAPPA weight calibration and on the bottom row distortion matched calibration data was used. For low acceleration factors ($R < 4$) the choice of a distortion-matched calibration is of less importance, while clear image degradation can be seen for higher acceleration factors (Fig. 29g,m).

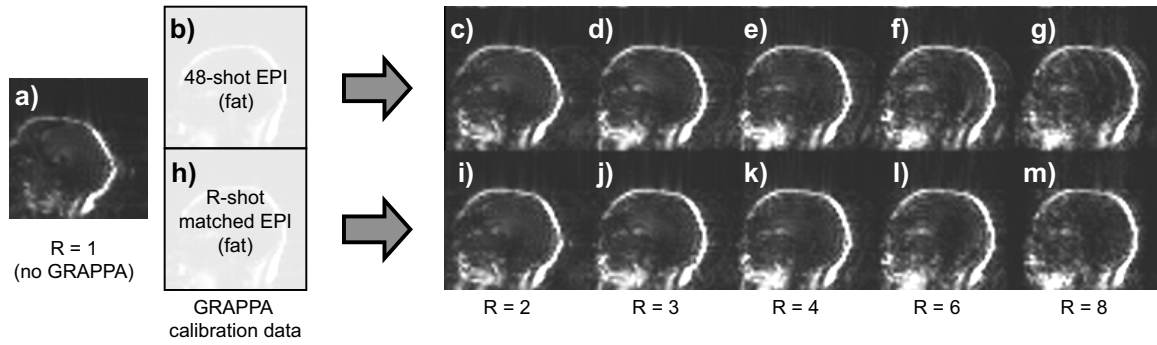
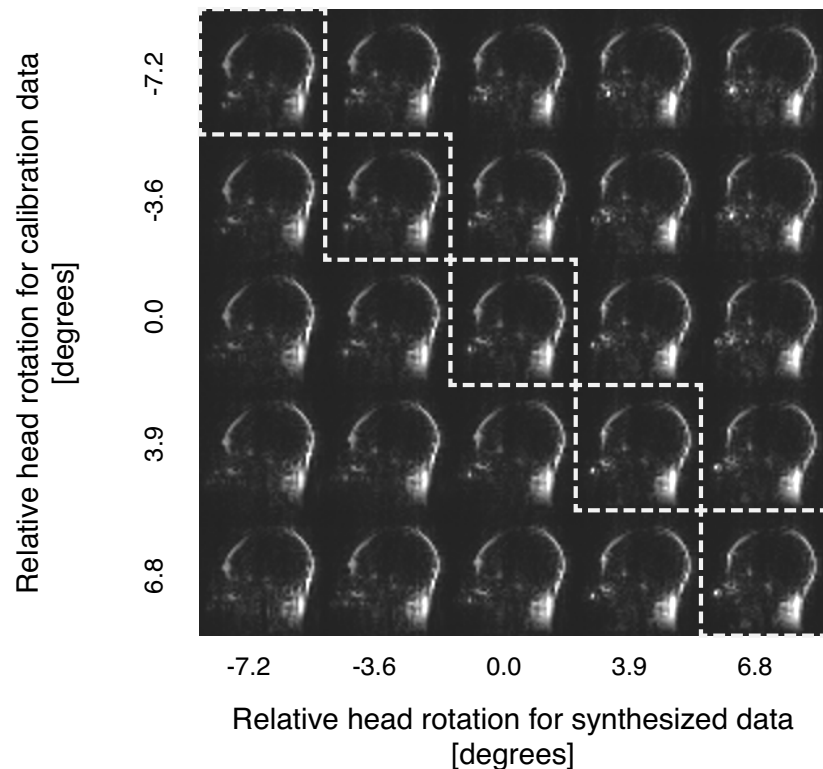


Figure 29. Fully sampled data versus distortion matched calibration data for FatNav.

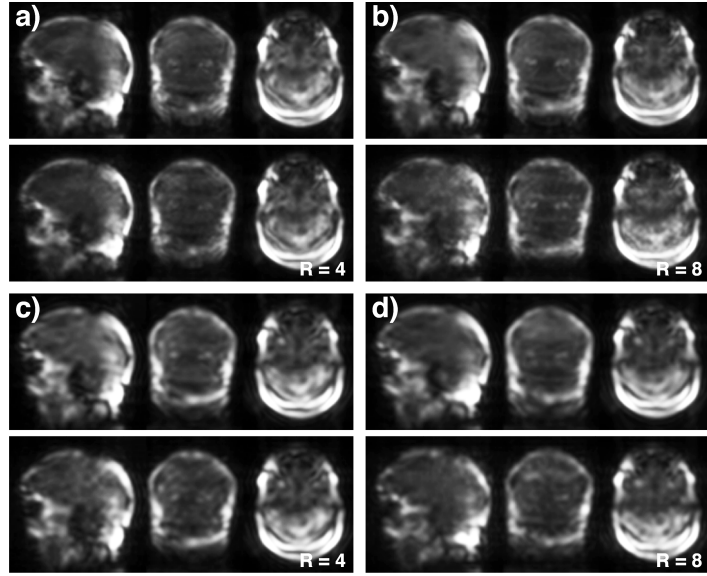
With content and distortion-matched calibration data, the effect of head pose was investigated and presented in Figure 30. The white dashed lines denote no change in head pose between calibration and data synthesis. The further from the diagonal the relative difference between calibration data and head pose increases. Although a drop in image quality can be seen with the mismatch the overall decrease is not significantly impairing the shape or definition of the fat contour.

Figure 30. Validity of GRAPPA weights as a function of head pose. The white dashed lines denote self-calibrated data sets with an increasing mismatch the further away from main diagonal.



4.5 COLLAPSED FATNAV

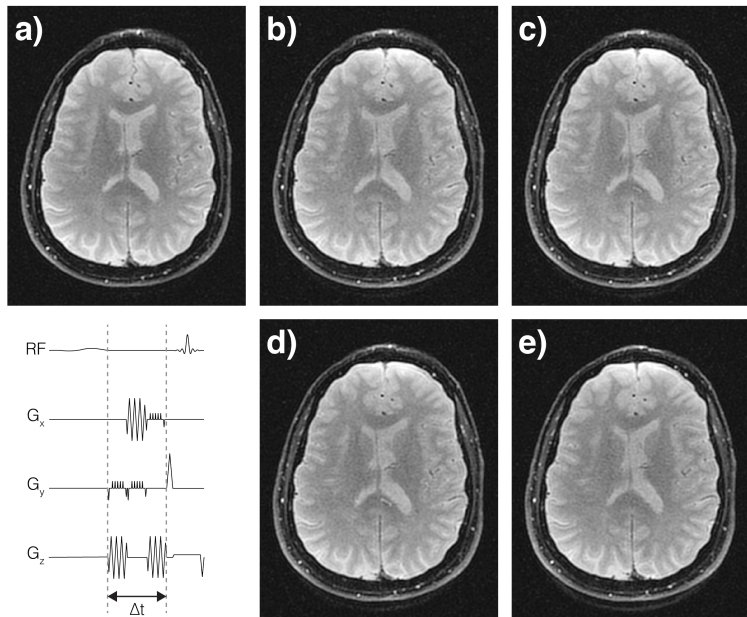
Figure 31 shows two cFatNav data sets at two different resolutions for two different parallel imaging acceleration levels. The upper panel of Fig. 31a-d shows data reconstructed from full data sets, while the bottom row is from a reduced data set. Typical parallel imaging reduction artifacts are absent.



The slightly increased noise level in the $R = 8$ data is primarily due to that only six k-space lines were acquired for the 48×48 case (Fig. 31b) and four lines for the 32×32 case (Fig. 31d).

Figure 31. cFatNav with 48×48 matrix and a) $R = 4$, b) $R = 8$. 32×32 matrix with c) $R = 4$, and d) $R = 8$ (top: full data, bottom: reduced data).

Figure 32. Effects of introducing a delay between the ChemSat RF pre-pulse and the excitation. a) SpSp water only excitation, b) 0 ms delay, c) 6.4 ms delay (default protocol), d) 15 ms delay, and e) 25 ms delay.



By adding the cFatNav readout block a delay is introduced between the ChemSat pulse and the host sequence excitation pulse. The effect of this delay is shown in Figure 32. With a delay corresponding to the suggested default protocol, Table 7, no visible degradation of fat saturation could be found via visual inspection of Fig. 32c. For the longest delay (25 ms) a faint streak from off resonance signal can be seen at the posterior part of the skull. This delay is however more than three times longer than what is required for a cFatNav readout (at the largest matrix size).

Figure 33 shows stability measurements for the cFatNav module over time. In Fig. 33a cFatNav acquired at three times the suggested acquisition rate for 8 minutes is shown. The jitter seen in the data is caused by registration errors between the current and reference frame due to signal intensity differences. The host sequence's RF pulses act on the magnetization for both water and fat creating dark bands in the cFatNav data, which also change from slice to slice. Fig. 33b shows long-term eddy-currents effects on the navigator precision stemming from the single refocused diffusion-encoding gradients ($b = 1000 \text{ s/mm}^2$).

DW 3D-MS EPI prospectively corrected with a cFatNav readout block is shown in Figure 34. In Figs. 34a,b the subject was instructed to lie as still as possible, while instructed to nod the head for Figs. 34c,d. For all datasets cFatNav data were acquired in parallel, however real-time feedback motion updates were only applied for Fig. 34b,d. From Fig. 34b it is clear that the jitter detected in Fig. 33 does not introduce any visible image artifacts. By comparing the data in Figs. 33c,d it is apparent that the cFatNav motion correction improves data consistency. There is some residual blurring still present, but the image quality is overall on par with the motion free data, Figs. 33a,b.

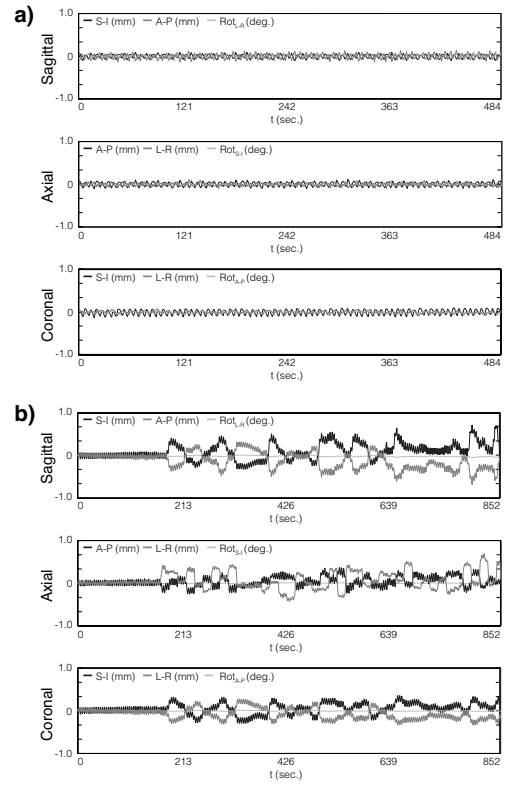


Figure 33. cFatNav stability measurements with a) three times the temporal resolution, b) diffusion encoding gradients

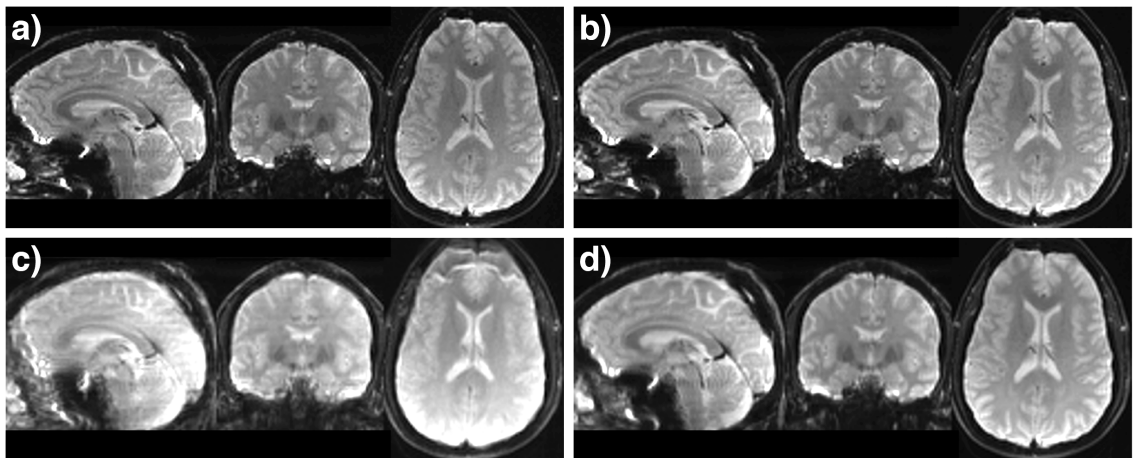


Figure 34. DW 3D-MS EPI combined with cFatNav for a,b) no motion, and c,d) nodding motion. Prospective updates were applied for b,d)

DISCUSSION

4.6 DIFFUSION-WEIGHTED IMAGING

4.6.1 Low distortion imaging and vGRASE

With a combination of diffusion weighting and vertical GRASE it was possible to acquire EPI data with reduced geometric distortions for a given image matrix size, where the width of each blind determines the level of distortions and the height and number of blinds together determine the final image resolution. The partial-Fourier approach that reduced the number of blinds from five to three was necessary to achieve a reasonable signal for the last blind in the readout train. Higher image resolutions than the 192x192 attempted would require more blinds, and the image quality would be limited by increasing T2-decay (and T2-blurring) rather than increased distortions like in ss-EPI.

Aside from the challenge with T2-blurring, due to the step-wise T2 signal decay across blinds, the major component that had to be addressed in DW-vGRASE was the stimulated echoes due to the non-CPMG condition. With a variation in duration between the refocusing RF-pulses, the stimulated echoes that arise from the non-perfect 180 flip angles in the slice are no longer coherent with the regular spin-echoes, generating signal voids in the reconstructed data, both for the T2-weighted and the diffusion weighted images. Our first approach was to make the slices sharper, and thereby obtain a flip angle distribution tighter around 180 degrees and weaken the stimulated echo pathways. The second approach was to vary the crusher areas from one refocusing pulse to the next, effectively dephasing all non-spin-echo pathways. This latter approach was found much more effective in dealing with the problem. With the crusher alterations in place, little gain was achieved with better RF pulses. In the interest of shortening the effective TE standard RF pulses could therefore be used, with maintained image quality. The relative difference in crusher area must however be large enough to produce both FID spoiling from each refocusing pulse and enough incoherence in the stimulated echoes (so they do not contribute to the signal). At the same time the crusher gradients cannot be so large that they add additional diffusion-weighting along the readout train or significantly increases the sequence time. The problem with stimulated echoes was found more prominent at 3T than at 1.5T.

With three blinds covering a partial-Fourier k-space, the order the blinds are played out makes a difference in the image. If the central blind is acquired first in the readout train, a short effective TE is achieved but the noise in the outer parts of k-space is elevated. With the central blind instead acquired last, the outer parts of

k-space are better preserved, and this was the preferred choice after visual inspection of DW-vGRASE images acquired in both ways. To reduce the high-pass filtration that result, an intensity normalization of the blinds was suggested and evaluated. As this was performed in the k-space domain, it cannot account for differences in T2 between tissues, and will never be able to completely compensate for the T2-decay.

DW-vGRASE is a single-shot technique that is not subject to the random diffusion phase issue in the same way as multi-shot sequences. Nevertheless, DW-vGRASE cannot ignore the diffusion phase as it is conjugated between RF-refocusing pulses while the signal phase is negated. To overcome this a tailored phase correction method was introduced to counteract the inconsistency between the blind readouts involving the central blinds of the T2-weighted and the diffusion-weighted data.

The vGRASE readout comes with a trade-off between TE, resolution and geometric distortions. Larger matrices than the proposed 192×192 matrix is possible but will result in increased distortions and T2-blurring. For a fixed distortion level, more blinds are needed at higher resolution, but this will further increase T2-blurring artifacts due to the longer train and give a longer effective TE. One could also reduce the matrix size, and use smaller blinds, giving both less T2-blurring, lower distortions and lower TE. To bear in mind is that as the vertical blinds are narrowed in the frequency encoding direction, data is to a larger extent read out on the gradient ramps, which also decrease in size and makes the k-space traversal slower and less efficient.

Seen to the relative time spent reading out data, the DW-vGRASE sequence could be argued being relatively scan efficient, and it is clear that a noticeable reduction in image distortions is achieved by this segmented readout approach. The increased TE (due to the multiple readouts) does however give the regular 2D DW-ssEPI an SNR advantage in comparison. With shorter readout times for the 2D DW-ssEPI, the minimum TR for a given number of slices is also shorter, giving the latter further advantages.

4.6.2 Multi-Slab Imaging

A DW 3D-MS EPI acquisition is basically a spin echo EPI sequence with two RF-refocused readouts and a diffusion preparation, where only the first readout is Fourier encoded in the slab direction. The slabs are acquired in a interleaved fashion (unlike e.g. time-of-flight (TOF) multi-slab imaging that is acquired one slab after each other to achieve the desired in-flow effect), with an updated phase encoding step in k_z between each TR. Compared to DW-vGRASE, DW 3D-MS EPI

has like ss-EPI a higher distortion level for a given in-plane matrix size. The DW 3D-MS EPI sequence has however significantly higher SNR efficiency than both ss-EPI and DW-vGRASE, making it much more interesting to develop further.

For any 2D imaging, the slice resolution is determined by the composite slice profile of the excitation and refocusing RF-pulses. A perfect box-shaped profile is therefore only a theoretical concept. Specific to EPI, a robust and strong fat-suppression is preferred in favor of better slice profile fidelity, which has led to the wide use of SpSp RF excitation pulses. While not specific to DW MRI, a bad slice definition the tissue in the imaged voxels will be weighted by the slice profile in the slice direction, creating a comb like weighting filter of the tissue in the slice direction over the entire volume. Tissue microstructure at the center of the slice will contribute more to the signal than tissue at the edges. One can imagine that this is not ideal for advanced diffusion imaging or fiber tracking, although it has been outside the scope of this work to try to show this effect in experiments. At any rate, for multi-slab DWI the slice profile is perfectly rectangular as it is Fourier encoded, leading to unarguably more well-defined voxels. Moreover, the thicker excitation volume of multi-slab DWI implies that RF pulses with higher bandwidths may be used without reaching the gradient amplitude limitations. This shortens the RF pulses in time and leads to a shortened pulse sequence.

The major obstacle in reconstructing multi-slab data is to seamlessly combine the slabs into one full volume without slab banding artifacts. We discovered early in the implementation process that the slab profile is of great importance and that the default RF pulses needed to be replaced. The default SpSp RF excitation pulse is excellent in its role to only excite water, but the resulting slab definition is quite poor. As a result, it has to be made significantly wider to match the FWHM criteria for the combined slab thickness. This effect becomes a cross-talk issue for 2D acquisitions but is otherwise not seen in the data. For multi-slab scans, the non-rectangular slab profile is exposed and results in severe banding artifacts and an uneven tissue saturation.

We therefore chose to use a separate non-spatially selective fat-sat (ChemSat) pulse followed by an SLR optimized sharp RF excitation of our choice, and so also for the refocusing pulse. The consequence of more well-defined RF pulses is longer RF pulse durations and therefore also sequence duration, but with excessive over-scaling of the slices is on the other hand no longer needed to meet the prescribed slice thickness, with less cross-talk as a result.

Another issue in the strive for sharper slices or slabs is to get the right flip angle in the central part of the FOV. We have found it often necessary to alter the RF

transmit gain somewhat to get a better overall flip angle across the object. We believe this has to do with that the auto-gain setting in the prescan primarily optimizes the flip angle for tissues close to the receiver coil elements as the signal there is much stronger.

As the slab thickness and profile scales linearly with the slab selection gradient, increasing the slab thickness forces more overlap in units of phase encodes, although the percentage overlap remains the same. To optimize the scan coverage, it is therefore important to choose the separation of the RF-pulses such that the overlap is minimized. Disregarding patient motion, the ideal overlap would be if two adjacent slabs could be combined with one shared Fourier encoded slice. For a flat SNR across the imaged volume the signal contribution each both slab into this overlapping position should be $1/\sqrt{2}$. Even with this ideal configuration, at least one more Fourier encoded slice must be added on either side of each slab to avoid wrap-around artifacts, leading to a minimum overlap of three, in units of Fourier encoded slices. For a more robust slab combination and for motion correction purposes, the DW 3D-MS EPI data presented in this thesis have however been acquired with an overlap of four slices.

The key component in the DW 3D-MS EPI reconstruction is however the phase correction. Without a properly working phase correction the slice direction Fourier transform would not be possible, as each kz encode would have its own Fourier phase and a unique diffusion phase. The method presented relies on that the diffusion phase is slowly varying, with a spatial resolution one the order of centimeters that is approximately constant across the z-direction of the slab. Phase changes with higher spatial frequency content would therefore be left uncorrected, as it can only detect in-plane variations. Beyond a slab thickness of ~30-35 mm, the 3D diffusion phase in the slab cannot be sufficiently removed using only a 2D navigator, which is why narrower slab thicknesses were used throughout this thesis work.

4.6.3 2D versus 3D

The DW 3D-MS EPI sequence was consistently shown to be more SNR efficient than 2D DW-ssEPI in both SNR efficiency simulations and scan-time normalized phantom and volunteer scans. This, despite that the shorter sequence duration of DW-ssEPI allows for more excited slices per unit of time than DW 3D-MS-EPI. RF slice profiles aside, the 3D approach is most competitive for large z-FOVs and many kz encodes. This is largely due to that excessively long TRs can be avoided with DW 3D-MS EPI for a large z-FOVs, since the number of slabs needed are less than the corresponding number of slices necessary for 2D DW-ssEPI. For long TRs,

beyond the regime of T1-relaxation of the brain parenchyma, the scan time increases without any additional signal gain.

Consequently, full brain DWI scans with a limited number of thick slabs tends to be the ideal combination for 3D-MS EPI. One may calculate an optimal TR w.r.t. SNR efficiency, where the benefit of shorter scan times at shorter TRs is counteracted by the reduced Mz recovery (or increased T1-w) for the tissues of interest. For GM/WM, the optimal TR is around 2 s by just taken these effects into account.

However, with different T1 weighting of the tissue at the center and at the slab-overlapping regions (exposed to twice as many excitations), slab-banding artifacts occur for TRs near the SNR optimal value. In this thesis work, we have had a low tolerance to slab banding artifacts as we find this both introduces a spatially periodic SNR across the volume and leads to banded isoDWI data. In addition, quantitative effects arise in the presence of head motion. For clinical use of the DW 3D-MS EPI sequence, we would suggest that TRs below 3000 ms should be avoided, noting that slab boundary artifacts will be reduced even further at yet higher TRs.

To enable a reduction of the TR towards the theoretical SNR optimal value with minimal slab banding artifacts, we have proposed two filtering methods. One that operates on the slabs before slab combination and the other that attempts to remove signal fluctuations in the final 3D volume using a band-pass filter. Both methods were successful in reducing the slab banding for a short TR of 2000 ms, with a slight advantage for the Fourier band-pass filtering approach. Combining the two did not result in any direct benefit. For both methods to work optimally, all imaged tissue would need to have approximately the same T1 value. For DWI data, where long-T1 tissues like CSF are suppressed, this is not a too bad of an approximation. In the absence of motion, both filters work as point operators and do not interfere with the calculation of parametric maps during post processing. Nevertheless, it is important to consider both methods primarily as an aid for visualization, and not as a pure correction method for the T1 saturation. The visualization aspect becomes important when e.g. the isoDWI or T2-w ($b=0$) data is being reformatted into other scan planes, where a periodic banding would be distracting for the radiologist.

4.6.4 Challenges

For DW 3D-MS EPI to become a serious contender to 2D DW-ssEPI, the main issue is the minimum scan time for a given set of diffusion directions. For research

applications, where volunteers most often are motivated and cooperative, a prolonged scan time is less of a hindrance. The ability to reach high, SNR rich, isotropic resolution can reasonably be justified with the extent of the scan time increase.

For clinical situations, where time is more critical and patient cooperation cannot be taken for granted, the DW 3D-MS EPI protocol has to be more strictly adapted. The current suggested protocol (1) is using two or three T2-weighted volumes (for parallel imaging self-calibration) and six to eight diffusion encoding directions, yielding a ~3:30 minute scan time at $2.0 \times 2.0 \times 2.0 \text{ mm}^3$ resolution with full brain coverage. Although fewer diffusion directions are possible compared to a 2D DW-ssEPI in the same scan time, the ability to do reformats and treating the diffusion-weighted data as any other 3D acquisition is valuable in many clinical situations. There has been a gradually increasing demand for 3D sequences over the last years and hopefully this DW 3D-MS EPI sequence can be a suitable workhorse for clinical diffusion-weighted imaging.

4.7 MOTION CORRECTION

4.7.1 Fat navigators

While other recently proposed image domain motion navigators, like vNav and PROMO, use the water magnetization of the brain, the FatNav method is selective on the fat signal in the head, which largely means the subcutaneous fat and fat around the eyes. With FatNav, the idea is that the interleaved motion navigator does as little harm to, or use of, the diagnostically relevant magnetization in the brain. Except for the fat in the neck region, the fat signal in the FOV moves rigidly with the brain, making it possible to directly apply motion estimates derived from fat signal data to the brain data acquired with the host pulse sequence.

For a quick data readout for the FatNav module, an accelerated EPI-readout was chosen. Even if the FatNav EPI data is of low resolution, geometric distortions will be present to some extent, especially at 3T. As these distortions change character as the head is rotated, the apparent shape of the head in the FatNav data may change and lead to bias in the motion estimates. Parallel imaging techniques such as GRAPPA reduces the amount of distortions by the acceleration factor R . In this work, parallel imaging acceleration factors ranging from $R = 1-8$ were attempted on an 8-channel receive only head coil. For a SENSE reconstruction using an 8-channel coil, the reconstruction problem becomes strictly underdetermined if $R > 8$, but notable reconstruction errors (g-factor noise) usually occurs already around $R = 4$. For GRAPPA, the matrix for the GRAPPA weight estimation can be invertible even

if R is larger than the number of coil elements as the number of ACS lines (i.e. the amount of calibration data) determines the ‘tall-ness’ of this matrix. Still, R factors again around 4 or higher usually gives unacceptable data for regular imaging due to g-factor limitations, since there is not enough discrepancy between the coils to solve the system in a stable manner without structured noise amplifications.

For FatNav, the situation is different. With the imaged fat signal located mostly in the skull near the coil elements, the FatNav data become well suited for parallel imaging. At $R = 8$, both distortions and readout-time can be significantly reduced without significant reconstruction errors, which improves both scan efficiency and image registration. A core enabler for these high acceleration factors is a carefully performed GRAPPA calibration and calibration scan. A lot of effort was therefore put into determining how this should be performed. It was found that a calibration scan that has the same contrast and the same distortion level as the intended navigator is the optimal choice. It might seem slightly counter-intuitive but is in good compliance with previous studies (29). This also holds when motion is introduced.

Our experiments showed that high acceleration factors ($R = 8$) produces motion estimates with less bias compared to $R = 2$ FatNav scans. We can also with a fair amount of confidence attribute the errors for the $R = 2$ scans to the distortions as the bias is largely negated when the distortion direction is changed. This systematic bias seemed to be less influential on the rotational parameters, but further work is needed to quantify the accuracy in detail. For these sagittal FatNavs the frequency encoding direction was played out in the superior-inferior direction. In this way tissue outside the FOV, primarily the neck and shoulders could be prevented from folding back into the image.

For other fast imaging techniques, e.g. spiral (used in PROMO), off-resonances in the object results in image blurring. One could argue that this would be a better readout than EPI as there is no net shift of the anatomy. This is an alternative readout for FatNav, but to make it short enough and with minimal blurring, also the spiral readout would ideally need to be as highly accelerated. For spiral, non-Cartesian parallel imaging reconstruction is necessary. While we not yet have any experience with this type of reconstruction, it will be more computational intensive compared to Cartesian EPI, which may or may not increase the feedback time for prospective motion correction using FatNav. Depending on future accuracy measurements for our EPI based FatNav in a prospective feedback setting, a spiral readout may be considered trying as well.

Common for image-based navigators like PROMO, vNav, and FatNav is that for movements in the sagittal plane, the upper part of the neck does not move rigidly with the brain. This leads to wrong motion correction parameters if these regions are not masked out. In PROMO this has been addressed by using an adaptive mask (ROI) that follows and only includes the brain for the registration. For FatNav, we have not yet worked out a fully automated masking algorithm that excludes the neck and jaw. For now, we have simply applied a mask to the lower (inferior) 30% of the FOV to exclude the neck region. Attempts were also done with a more conservative mask that removed more of the inferior part of the FOV, but this did not improve the quality of the registration. With an automated mask not dependent on the placement of the head in the FOV, the image registration could be further improved and is a prerequisite for any clinical use.

For the initial experiments with the FatNav, only one sagittal image plane were acquired, hence only nodding motion within that plane could be detected. For a complete motion correction procedure this is not sufficient and the FatNav module should capture full 3D rigid body movements. This was the main aim of the follow up work with the collapsed FatNav method.

4.7.2 Collapsed fat navigators

With collapsed FatNav (cFatNav) the single EPI readout of the original sagittal 2D FatNav module was replaced with three orthogonal 2D EPI projection readouts to capture motion in 3D. By placing the three EPI readouts directly after the non-slice selective ChemSat RF pulse, only the duration of the readouts was added to the total sequence time for host pulse sequences such as EPI based DWI that already need the ChemSat RF module for its fat saturation. As the cFatNav readout was implemented in the vendor's generic ChemSat source code module that is compatible with multiple sequences, it is straightforward to broaden the use of cFatNav for other (non-diffusion) pulse sequences in future. Similar to the original FatNav technique, very high parallel imaging acceleration factors has been show possible for cFatNav ($R = 8$), and as a result the total readout duration for three projection planes can be limited to only a few milliseconds.

For DW 3D-MS EPI, with an acquisition time per volume of ~20-30 seconds, the efficacy of volume-to-volume retrospective motion correction is questionable as it is only be able to correct for very slow movements. In-plane motion correction has been shown possible in this thesis, using the diffusion-phase navigators, but cannot correct for any out-of-plane movements. Combining DW 3D-MS EPI with cFatNav is hence helpful. With a sequence time of ~170 ms, the addition of a cFatNav readouts would result in only a ~3-4% scan time increase. For 2D DW

ssEPI (with a read-out of ~ 120 ms) motion updates would occur at 6 Hz and the increased sequence time would be about 5-6%, which should be justified in a clinical context.

Despite the perceived lack of sparsity in the reconstructed images acceleration factors similar to that of our original 2D FatNav was shown possible. This is likely due to that the subcutaneous fat is well separated in space and located close to the individual receiver coils, and that little fat is located in the central parts of the brain where the coil geometry factor is high. In its current implementation, the cFatNav GRAPPA weights and gradient delay compensation are calculated once at the beginning of the scan. If large head movements are detected, new data set and calibration could be obtained if necessary, at the cost of ~ 1 second of missed updates. For image intensity stability reasons it was found that using the same ky dephasing gradient amplitude for all acquired navigators was preferable, as opposed to continuously changing the dephasing gradient, the latter which would allow for the estimation of new calibration data every Rth excitation.

There was initially a concern that there would be drifts in the navigator data due to the increased system load, e.g. B_0 drifts causing a translation offsets. When testing this, using a three-fold acquisition rate, no drift was observed over an eight-minute acquisition. With diffusion-encoding gradients applied, a smaller TR-periodic drift of the motion estimates could be observed due to long term eddy currents from the previous TR. How to address these fluctuations will be a subject for future work, optimizing the entire motion correction procedure and data feedback.

By inserting the cFatNav readout, a delay is introduced between the ChemSat RF pulse and the initial excitation RF pulse of the host sequence. It was at first unclear whether this gap would result in a reduced fat saturation. However, our tests show that the delay needs to be roughly four times that of the duration of the cFatNav readouts used for DW 3D-MS EPI to have any bad influence on the fat saturation performance.

With cFatNav played out for each slice, the previously excited slice by the host pulse sequence could be observed as dark bands across the cFatNav projection images. I.e. while cFatNav has no impact on the host sequence, the latter affects the data of the cFatNav since its excitation is not spectrally selective on water. Because of this, a slight jitter could be seen in the acquired motion estimates that correlate with this banding from the host sequence excitations. To dampen this jitter, temporal averaging may be performed (at the expense of temporal resolution), or importance weighting (excluding the dark bands) can be applied when performing the realignment. We will explore both these options next.

When combining cFatNav with DW 3D-MS EPI in-vivo, no apparent image degradation was found in the absence of motion with the prospective motion correction turned on. For the controlled nodding motion experiments, a clear improvement in image quality could be seen with the cFatNav prospective correction applied. This, despite the quite crude realignment procedure that has been used this far. To correctly address the full 3D motion, a more advanced model for extracting motion estimates will have to be used, e.g. projection-to-volume algorithms for registration.

It should be noted that cFatNav is a navigator that is not uniquely designed to work with DW 3D-MS EPI. It was implemented to be easily combined with other pulse sequences such as T₂-w FSE sequences. Depending on whether fat saturation of the FSE image data is desired, the ChemSat RF pulse flip angle could be set to either a few degrees (for minimal fat-sat effect) or 90 degrees.

By combining the cFatNav module with the DW 3D-MS EPI sequence, we have taken a first step to a prospective motion corrected high-resolution diffusion-weighted 3D imaging sequence that can be used on uncooperative patients and children.

5 ACKNOWLEDGEMENTS

Stefan Skare, for inviting a bearded man to California in 2010 and supporting him since then.

Bo Nordell, who first introduced me to MRI, showed me how much fun it is, and gave me my first employment.

My co-supervisors, Olof Flodmark and Anders Lilja, for support, backup, and help. Special thanks to Olof for making this whole thing possible by allowing us to work freely and unrestricted. Anders for always taking time to discuss and improve new methods and ideas.

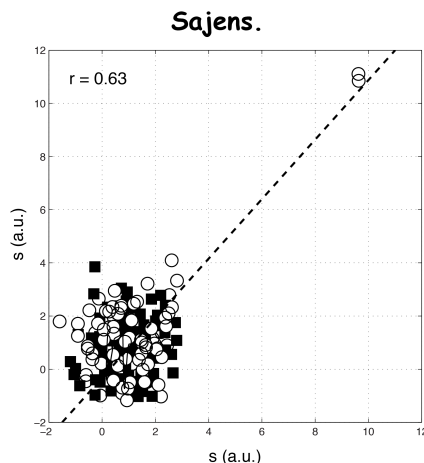
Magnus Mårtensson (ol' chap), Ola Norbeck, and Enrico Avventi for the every day fun and being the greatest co-workers! Past co-workers Anders Nordell, Finn Lennartsson, and Axel Hartwig (ITBOSL) for the same thing.

All personnel at Neuroradiology for being supportive, open-minded when trying new stuff out, understanding when “new stuff” does not work, and being a good competitor in the quest for scan time. Some extra thanks to those being close to my projects - Yords, Christina (*“Jag lovar att jag skall stänga av autotransfer i fortsättningen”*), Marie, Patrik, Lars P, Lars B, Birgitta, Mitra, Peter, Per (*“Mors!”*), Lucas, Elisabeth, and Maria.

My parents, Addie and Jan-Åke, for being there for me, pushing me, and always helping out. Same thing goes for Bettis, Åke, and Ellinor.

Friends, for being friends - Krister, Tobias, Kenneth, Boris, Bojan, Calle W, Karl P, Elias, Jenny, Julia, and Nicklas. I'm sure I forgot someone...

Josefin, thanks for putting up with me. Love you!



6 REFERENCES

1. Boltzmann L. Wissenschaftliche Abhandlungen. Leipzig: Barth; 1909.
2. Guyton AC. Textbook of Medical Physiology. Philadelphia: W.B. Saunders; 1991.
3. Bottomley PA. Turning up the heat on MRI. Journal of the American College of Radiology : JACR 2008;5(7):853-855.
4. Mansfield P. Multi-planar image formation using NMR spin echoes. J Physics C: Solid State Phys 1977;10:4.
5. Carr HY, Purcell EM. Effects of Diffusion on Free Precession in Nuclear Magnetic Resonance Experiments. Phys Rev 1954;94(1):630-638.
6. Stejskal O, Tanner JE. Spin diffusion measurements: Spin echoes in the presence of a time-dependent field gradients. J Chem Phys 1965;42(1):288-292.
7. Kwong KK, Belliveau JW, Chesler DA, Goldberg IE, Weisskoff RM, Poncelet BP, Kennedy DN, Hoppel BE, Cohen MS, Turner R, et al. Dynamic magnetic resonance imaging of human brain activity during primary sensory stimulation. Proc Natl Acad Sci U S A 1992;89(12):5675-5679.
8. Menon RS, Ogawa S, Kim SG, Ellermann JM, Merkle H, Tank DW, Ugurbil K. Functional brain mapping using magnetic resonance imaging. Signal changes accompanying visual stimulation. Invest Radiol 1992;27 Suppl 2:S47-53.
9. Posse S. Direct imaging of magnetic field gradients by group spin-echo selection. Magn Reson Med 1992;25(1):12-29.
10. Meiboom S, Purcell E. Modified spin-echo method for measuring nuclear relaxation times. Rev Sci Instrum 1958;29:688-691.
11. Skare S, Clayton DB, Newbould R, Moseley ME, Bammer R. A fast and robust minimum entropy based non-interactive Nyquist ghost correction algorithm. 2006; Seattle, WA, USA. p 2349.
12. Clare S. Iterative Nyquist Ghost Correction for Single and Multi-shot EPI using an Entropy Measure. 2003; Toronto, Canada. p 1041.
13. Meyer CH, Pauly JM, Macovski A, Nishimura DG. Simultaneous spatial and spectral selective excitation. Magn Reson Med 1990;15(2):287-304.
14. Block W, Pauly J, Kerr A, Nishimura D. Consistent fat suppression with compensated spectral-spatial pulses. Magn Reson Med 1997;38(2):198-206.

15. Schick F. Simultaneous highly selective MR water and fat imaging using a simple new type of spectral-spatial excitation. *Magn Reson Med* 1998;40(2):194-202.
16. Zur Y. Design of improved spectral-spatial pulses for routine clinical use. *Magn Reson Med* 2000;43(3):410-420.
17. Noll DC, Nishimura DG, Macovski A. Homodyne detection in magnetic resonance imaging. *IEEE Trans Med Imaging* 1991;10(2):154-163.
18. Haacke EM, Liang Z.P., Boada F. Image reconstruction using projections onto convex sets, model constraints and linear prediction theory for the removal of phase, motion, and Gibbs artifacts in magnetic resonance imaging and ultrasound imaging. *Opt Eng* 1984;29:11.
19. McKinnon GC. Ultrafast interleaved gradient-echo-planar imaging on a standard scanner. *Magn Reson Med* 1993;30(5):609-616.
20. Griswold MA, Jakob PM, Heidemann RM, Nittka M, Jellus V, Wang J, Kiefer B, Haase A. Generalized autocalibrating partially parallel acquisitions (GRAPPA). *Magn Reson Med* 2002;47(6):1202-1210.
21. Pruessmann KP, Weiger M, Scheidegger MB, Boesiger P. SENSE: sensitivity encoding for fast MRI. *Magn Reson Med* 1999;42(5):952-962.
22. Porter D, Mueller E. Multi-shot diffusion-weighted EPI with readout mosaic segmentation and 2D navigator correction. 2004; Kyoto, Japan. p 442.
23. Skare S, Newbould RD, Clayton DB, Bammer R. Propeller EPI in the other direction. *Magn Reson Med* 2006;55(6):1298-1307.
24. Pipe JG. Motion correction with PROPELLER MRI: application to head motion and free-breathing cardiac imaging. *Magn Reson Med* 1999;42(5):963-969.
25. Skare S, Andersson JLR, Bammer R. Calibration free distortion correction for propeller EPI. 2008; Toronto. p 417.
26. Brown R. A brief account of microscopical observations mad on the particles contained in the pollen of plants. *Philos Mag* 1828;4:12.
27. Einstein A. Über die von der molekularkinetischen Theorie der Wärme geforderte Bewegung von in ruhende Flüssigkeiten suspendierten Teilchen. *Ann Phys* 1905;8:11.
28. Le Bihan D. [Diffusion, perfusion and functional magnetic resonance imaging]. *Journal des maladies vasculaires* 1995;20(3):203-214.
29. Basser PJ, Mattiello J, LeBihan D. Estimation of the effective self-diffusion tensor from the NMR spin echo. *Journal of magnetic resonance Series B* 1994;103(3):247-254.

30. Basser PJ, Mattiello J, LeBihan D. MR diffusion tensor spectroscopy and imaging. *Biophysical journal* 1994;66(1):259-267.
31. Andersson JLR, Skare S. A model-based method for retrospective correction of geometric distortions in diffusion-weighted EPI. *Neuroimage* 2002;16(1):177-199.
32. Reese TG, Heid O, Weisskoff RM, Wedeen VJ. Reduction of eddy-current-induced distortion in diffusion MRI using a twice-refocused spin echo. *Magn Reson Med* 2003;49(1):177-182.
33. Dietrich O, Heiland S, Benner T, Sartor K. Reducing motion artefacts in diffusion-weighted MRI of the brain: efficacy of navigator echo correction and pulse triggering. *Neuroradiology* 2000;42(2):85-91.
34. Skare S, Andersson JL. On the effects of gating in diffusion imaging of the brain using single shot EPI. *Magn Reson Imaging* 2001;19(8):1125-1128.
35. Bammer R, Keeling SL, Augustin M, Pruessmann KP, Wolf R, Stollberger R, Hartung HP, Fazekas F. Improved diffusion-weighted single-shot echo-planar imaging (EPI) in stroke using sensitivity encoding (SENSE). *Magn Reson Med* 2001;46(3):548-554.
36. Atkinson D, Porter DA, Hill DL, Calamante F, Connelly A. Sampling and reconstruction effects due to motion in diffusion-weighted interleaved echo planar imaging. *Magn Reson Med* 2000;44(1):101-109.
37. Atkinson D, Counsell S, Hajnal JV, Batchelor PG, Hill DL, Larkman DJ. Nonlinear phase correction of navigated multi-coil diffusion images. *Magn Reson Med* 2006;56(5):1135-1139.
38. Liu C, Bammer R, Kim DH, Moseley ME. Self-navigated interleaved spiral (SNAILS): application to high-resolution diffusion tensor imaging. *Magn Reson Med* 2004;52(6):1388-1396.
39. Liu C, Moseley ME, Bammer R. Simultaneous phase correction and SENSE reconstruction for navigated multi-shot DWI with non-cartesian k-space sampling. *Magn Reson Med* 2005;54(6):1412-1422.
40. Bammer R, Aksoy M, Liu C. Augmented generalized SENSE reconstruction to correct for rigid body motion. *Magn Reson Med* 2007;57(1):90-102.
41. Pipe JG, Farthing VG, Forbes KP. Multishot diffusion-weighted FSE using PROPELLER MRI. *Magn Reson Med* 2002;47(1):42-52.
42. Engström M, Bammer R, Skare S. Diffusion weighted vertical gradient and spin echo. *Magn Reson Med* 2012;68(6):1755-1763.
43. Engström M, Skare S. Diffusion-Weighted 3D Multislab Echo Planar Imaging for High Signal-to-Noise Ratio Efficiency and Isotropic Image Resolution. *Magn Reson Med* 2013;70:1507-1514.

44. Ordidge RJ, Helpert JA, Qing ZX, Knight RA, Nagesh V. Correction of motional artifacts in diffusion-weighted MR images using navigator echoes. *Magn Reson Imaging* 1994;12(3):455-460.
45. Anderson AW, Gore JC. Analysis and correction of motion artifacts in diffusion weighted imaging. *Magn Reson Med* 1994;32(3):379-387.
46. Pipe JG. Whole Blade Method for Robust PROPELLER DWI. 2007; Berlin, Germany. p 1486.
47. Andersson JLR, Skare S, Ashburner J. How to correct susceptibility distortions in spin-echo echo-planar images: application to diffusion tensor imaging. *Neuroimage* 2003;20(2):870-888.
48. Smith SM, Jenkinson M, Woolrich MW, Beckmann CF, Behrens TE, Johansen-Berg H, Bannister PR, De Luca M, Drobnjak I, Flitney DE, Niazy RK, Saunders J, Vickers J, Zhang Y, De Stefano N, Brady JM, Matthews PM. Advances in functional and structural MR image analysis and implementation as FSL. *Neuroimage* 2004;23 Suppl 1:S208-219.
49. Forbes KP, Pipe JG, Karis JP, Heiserman JE. Improved image quality and detection of acute cerebral infarction with PROPELLER diffusion-weighted MR imaging. *Radiology* 2002;225(2):551-555.
50. Pipe JG, Zwart N. Turboprop: improved PROPELLER imaging. *Magn Reson Med* 2006;55(2):380-385.
51. Li Z, Pipe JG, Lee CY, Debbins JP, Karis JP, Huo D. X-PROP: A Fast and Robust Diffusion-Weighted PROPELLER Technique. 2011; Montreal, Canada. p 179.
52. Skare S, Andersson JL. Correction of MR image distortions induced by metallic objects using a 3D cubic B-spline basis set: application to stereotactic surgical planning. *Magn Reson Med* 2005;54(1):169-181.
53. O'Halloran RL, Aksoy M, Van AT, Bammer R. 3D isotropic high-resolution diffusion-weighted MRI of the whole brain with a motion-corrected steady-state free precession sequence. *Magn Reson Med* 2013;70(2):466-478.
54. O'Halloran R, Aksoy M, Aboussouan E, Peterson E, Van A, Bammer R. Real-time correction of rigid body motion-induced phase errors for diffusion-weighted steady-state free precession imaging. *Magn Reson Med* 2014.
55. Parker DL, Yuan C, Blatter DD. MR angiography by multiple thin slab 3D acquisition. *Magn Reson Med* 1991;17(2):434-451.
56. Oshio K, Jolesz FA, Melki PS, Mulkern RV. T2-weighted thin-section imaging with the multislab three-dimensional RARE technique. *J Magn Reson Imaging* 1991;1(6):695-700.

57. Frost R, Miller KL, Tijssen RH, Porter DA, Jezzard P. 3D Multi-slab diffusion-weighted readout-segmented EPI with real-time cardiac-reordered k-space acquisition. *Magn Reson Med* 2013.
58. Engström M, Nordell A, Mårtensson M, Nordell B, Bammer R, Skare S. Isotropic resolution in Diffusion Weighted Imaging using 3D multi-slab, multi-echo Echo Planar Imaging. 2010; Stockholm, Sweden. p 1619.
59. Van AT, Karampinos DC, Sutton BP. High Resolution 3D Multi-slab Multi-shot Spin Echo Diffusion-Weighted Imaging. 2010; Stockholm, Sweden. p 1618.
60. Engström M, Martensson M, Avventi E, Skare S. On the signal-to-noise ratio efficiency and slab-banding artifacts in three-dimensional multislab diffusion-weighted echo-planar imaging. *Magn Reson Med* 2014.
61. Le Roux P; French patent 86101791986.
62. Shinnar M, Bolinger L, Leigh JS. The synthesis of soft pulses with a specified frequency response. *Magn Reson Med* 1989;12(1):88-92.
63. Shinnar M, Bolinger L, Leigh JS. The use of finite impulse response filters in pulse design. *Magn Reson Med* 1989;12(1):81-87.
64. Shinnar M, Eleff S, Subramanian H, Leigh JS. The synthesis of pulse sequences yielding arbitrary magnetization vectors. *Magn Reson Med* 1989;12(1):74-80.
65. Shinnar M, Leigh JS. The application of spinors to pulse synthesis and analysis. *Magn Reson Med* 1989;12(1):93-98.
66. Viola P, Wells W. Alignment by maximization of mutual information. 1995; Cambridge, USA.
67. Nelder J, Mead R. A simplex method for function minimization. *Computer Journal* 1965(7):5.
68. Engström M, Skare S. In-plane motion correction for Diffusion-Weighted 3D Multi-Slab EPI. Proceedings of the 21st Annual Meeting of ISMRM. Salt Lake City, USA2013. p 2579.
69. White N, Roddey C, Shankaranarayanan A, Han E, Rettmann D, Santos J, Kuperman J, Dale A. PROMO: Real-time prospective motion correction in MRI using image-based tracking. *Magn Reson Med* 2010;63(1):91-105.
70. Maclaren J, Armstrong BS, Barrows RT, Danishad KA, Ernst T, Foster CL, Gumus K, Herbst M, Kadashevich IY, Kusik TP, Li Q, Lovell-Smith C, Prieto T, Schulze P, Speck O, Stucht D, Zaitsev M. Measurement and correction of microscopic head motion during magnetic resonance imaging of the brain. *PloS one* 2012;7(11):e48088.

71. Zaitsev M, Dold C, Sakas G, Hennig J, Speck O. Magnetic resonance imaging of freely moving objects: prospective real-time motion correction using an external optical motion tracking system. *Neuroimage* 2006;31(3):1038-1050.
72. Schulz J, Siegert T, Bazin PL, Maclaren J, Herbst M, Zaitsev M, Turner R. Prospective slice-by-slice motion correction reduces false positive activations in fMRI with task-correlated motion. *Neuroimage* 2014;84:124-132.
73. Ooi MB, Krueger S, Thomas WJ, Swaminathan SV, Brown TR. Prospective real-time correction for arbitrary head motion using active markers. *Magn Reson Med* 2009;62(4):943-954.
74. Kober T, Marques JP, Gruetter R, Krueger G. Head motion detection using FID navigators. *Magn Reson Med* 2011;66(1):135-143.
75. Thesen S, Heid O, Mueller E, Schad LR. Prospective acquisition correction for head motion with image-based tracking for real-time fMRI. *Magn Reson Med* 2000;44(3):457-465.
76. Hess AT, Tisdall MD, Andronesi OC, Meintjes EM, van der Kouwe AJ. Real-time motion and B0 corrected single voxel spectroscopy using volumetric navigators. *Magn Reson Med* 2011;66(2):314-323.
77. Alhamud A, Tisdall MD, Hess AT, Hasan KM, Meintjes EM, van der Kouwe AJ. Volumetric navigators for real-time motion correction in diffusion tensor imaging. *Magn Reson Med* 2012;68(4):1097-1108.
78. Setsompop K, Gagoski BA, Polimeni JR, Witzel T, Wedeen VJ, Wald LL. Blipped-controlled aliasing in parallel imaging for simultaneous multislice echo planar imaging with reduced g-factor penalty. *Magn Reson Med* 2012;67(5):1210-1224.
79. Bhat H, Cauley SF, Tisdall MD, Witzel T, Setsompop K, van der Kouwe A, Heberlein K. Prospective motion correction based on ultra-fast whole head navigators acquired with Multi-Band EPI. 2014; Tromsø, Norway.
80. Hartwig A, Mårtensson M, Skare S. 2D Fat Navigators (FatNav) for real-time correction of nodding motion of the patient's head. 2013; Salt Lake City, UT, USA. p 308.
81. Gallichan D, Marques JP, Gruetter R. FatNavs: Exploiting the Natural Sparsity of Head Fat Images for High-Resolution Motion-Navigation at Very High Acceleration Factors. 2013; Salt Lake City, USA. p 309.
82. Skare S, Hartwig A, Martensson M, Avventi E, Engstrom M. Properties of a 2D fat navigator for prospective image domain correction of nodding motion in brain MRI. *Magn Reson Med* 2014.

83. Avventi E, Engström M, Mårtensson M, Norbeck O, Skare S. Towards a real-time prospective 3D fat navigator: investigating the limits of parallel imaging. 2014; Tromsø, Norway.
84. Gallichan D, Marques AP, Gruetter R. Overproof GRAPPA: Exploiting the natural sparsity of fat images for 64-times accelerated motion navigators. 2014; Milan, Italy. p 4345.
85. Engström M, Mårtensson M, Norbeck O, Avventi E, Skare S. Collapsed FatNav - A 3D Motion Navigator Using the Chemical Saturation RF-pulse. 2014; Milan, Italy. p 1609.
86. Holdsworth S, Aksoy M, Newbould R, Yeom K, Van AT, Ooi MB, Barnes I, Bammer R, Skare S. Diffusion tensor imaging (DTI) with retrospective motion correction for large scale pediatric imaging. *Journal of Magnetic Resonance Imaging* 2012;36(4):10.
87. Andre JB, Mahmud M-B, Hoff NM, Smith CP, Cohen W. Patient Motion: Small Annoyance or Call To Action? 2014; Milan, Italy. p 1607.
88. Feinberg DA, Oshio K. GRASE (gradient- and spin-echo) MR imaging: a new fast clinical imaging technique. *Radiology* 1991;181(2):597-602.
89. Oshio K. vGRASE: separating phase and T(2) modulations in 2D. *Magn Reson Med* 2000;44(3):383-386.
90. Pauly J, Le Roux P, Nishimura D, Macovski A. Parameter relations for the Shinnar-Le Roux selective excitation pulse design algorithm [NMR imaging]. *IEEE transactions on medical imaging* 1991;10(1):53-65.
91. Skare S, Holdsworth SJ, Bammer R. Image domain Propeller FSE (iProp-FSE). 2010; Stockholm, Sweden. p 80.
92. Poncelet BP, Wedeen VJ, Weisskoff RM, Cohen MS. Brain parenchyma motion: measurement with cine echo-planar MR imaging. *Radiology* 1992;185(3):645-651.
93. Skare S, Holdsworth SJ, Newbould RD, Bammer R. On the battle between Rician noise and phase-interferences in DWI. 2009; Honolulu, Hawaii, USA. p 4617.
94. Edelstein WA, Glover GH, Hardy CJ, Redington RW. The intrinsic signal-to-noise ratio in NMR imaging. *Magn Reson Med* 1986;3(4):604-618.
95. Perman WH, Hilal SK, Simon HE, Maudsley AA. Contrast manipulation in NMR imaging. *Magnetic resonance imaging* 1984;2(1):23-32.
96. Van AT, Aksoy M, Holdsworth SJ, Kopeinigg D, Vos SB, Bammer R. Slab profile encoding (PEN) for minimizing slab boundary artifact in three-dimensional diffusion-weighted multislabs acquisition. *Magn Reson Med* 2014.

97. Bernstein MA, King KF, Zhou XJ. Handbook of MRI Pulse Sequences. Burlington (MA): Elsevier Academic Pres; 2004.
98. Wansapura JP, Holland SK, Dunn RS, Ball WS. NMR relaxation times in the human brain at 3.0 tesla. J Magn Reson Imaging 1999;9(4):7.